Polarization fluctuations in
vertical-cavity surface-emitting lasers

M.B. Willemsen

PhD. Thesis, Leiden University
Leiden, The Netherlands
September 2001

Promotiecommissie:

Promotor: Prof. dr. J. P. Woerdman
Copromotor: Dr. M. P. van Exter
Referent: Prof. dr. D. Lenstra (Vrije Universiteit, Amsterdam)
Leden: Prof. dr. K. J. Boller (Universiteit Twente)
                   Prof. dr. G. W. 't Hooft
                   Dr. F. Karouta (Technische Universiteit Eindhoven)
                   Prof. dr. G. Nienhuis
                   Prof. dr. ir. W. van Saarloos
                   Prof. dr. P. H. Kes

Contents

Chapter 1

Introduction

Communication and information technologies have become exceedingly important during the last decade. Laser diodes in combination with optical fiber networks are the backbone of modern communication systems like the Internet. The 2000 Nobel prize in physics was awarded for basic research on information and communication technology. Z. I. Alferov and H. Kroemer were honoured "for developing semiconductor hetero-structures used in high-speed- and opto-electronics", and J. S. Kilby was honoured "for his part in the invention of the integrated circuit". Semiconductor heterostructures form the basis of both micro-electronic components, like transistors and chips, and opto-electronic devices, like laser diodes. These structures consist of thin layers of different semiconductor materials grown sandwich-like on top of each other on a large wafer.

In the case of a laser diode, the light can propagate either parallel or perpendicular to the layered structure. Propagation of light parallel to the layers of the structure, as occurs in conventional laser diodes used in cd-players and bar-code readers, has a disadvantage. It requires cleavage of the overall wafer into small "bricks"to define a solitary device and to couple the light out from the edges of the layered stack. In a vertical-cavity surface-emitting laser, or VCSEL (pronounce as "vixel"), discussed in this thesis, the light propagates perpendicular to the semiconductor layers. Perpendicular propagation of light in the structure profits from the planar symmetry of the layers on the wafer. This construction allows in particular for integration of many solitary devices into two-dimensional arrays on a single wafer, which can be used for parallel optical data-communication. Integration of lasers into two-dimensional arrays is the opto-electronic equivalent of integration of micro-electronic components into chips. As a result of drastically improved performances, VCSELs have become increasingly popular during the last ten years.

This thesis presents a study of the polarization fluctuations in the light emitted by VCSELs. Understanding of polarization fluctuations is important since it seriously limits many VCSEL applications. This chapter starts with a comparison between conventional diode-lasers and VCSELs, it continues with a discussion of fabrication techniques, and concludes with an overview of this thesis.

1.1 VCSELs

Laser action in semiconductors was first reported in 1962 [1]. Figure 1.1 shows a conventional semiconductor laser, which consists of an active layer sandwiched between two cladding layers. The current, to create population inversion in the valence and conduction bands, is injected via the metal-stripe contact on top of the laser. The laser light propagates in the plane of the active layer and is emitted from the cleaved facets of the device. Therefore these conventional semiconductor lasers are called edge-emitters.
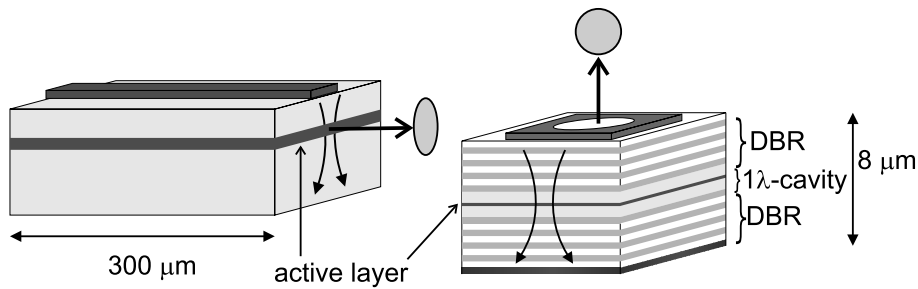
Figure 1.1: Sketches of a conventional semiconductor laser or edge-emitter (left-hand side) and of a vertical-cavity surface-emitting lasers or VCSEL (right-hand side). Please note the different size of the devices (not drawn to scale). For convenience, only a few mirror pairs of the VCSEL DBR mirrors are shown, which typically consists of 20-30 mirror pairs. In an edge-emitter, the light propagates in the plane of the active layer, whereas in a VCSEL the light propagates perpendicular to the active layer.

In contrast, a surface-emitting laser has its beam perpendicular to the active layer. The first surface-emitting laser was realized in 1979 by Iga [2]. It comprised a thick bulk GaAs active layer sandwiched between two metallic mirrors. A huge improvement was reported in 1989 when a thin quantum-well active layer was used in combination with multi-layer mirrors [3]. Figure 1.1 shows such a vertical-cavity surface-emitting laser, or VCSEL, with a cavity length matched to a single optical wavelength of light. The light inside the VCSEL propagates perpendicular to the quantum-well active layer. Since the optical gain from the (typically 10 nanometer) thin quantum-well active layer is limited, high reflectivity mirrors are needed. Multi-layer mirrors or Distributed Bragg Reflectors (DBRs), consisting of quarter-wave layers with alternating low and high-refractive index materials, have such high reflectivities (R > 99 %). The current is injected from the metal contact on top of the p-doped top-DBR into the n-doped bottom-DBR. For vertical confinement of the light typically DBRs with 20-30 mirror pairs are

used (for convenience only a few pairs are shown in Fig. 1.1). To achieve transverse confinement of the optical field and injection current, several methods have been developed, which are discussed in detail in Sec. 1.2.

The different topology of a VCSEL has important advantages when comparing with edge-emitters. The smaller volume leads to lower threshold currents [4] and high-speed modulation [5]. The geometry leads to a potentially high spectral purity, as the λ-cavity restricts oscillation to a single longitudinal mode. Another advantage of VCSELs is their planar two-dimensional architecture that allows for testing and processing on the wafer and requires no cleavage. Moreover, due to the planar symmetry solitary VCSELs can be integrated into two-dimensional arrays, so that a single wafer can contain more than hundred thousand lasers. VCSELs in 2D-arrays can be organized, depending on the wafer processing, as individually addressable devices or as densely-packed elements (see chapter 9). Two-dimensional arrays of individually addressable VCSELs can be used for parallel optical data communication, where the cylindrical symmetric and low-divergent VCSEL beams can be coupled into fibers easily.

VCSELs have improved quickly during the last decade. Nevertheless, there are several problems restricting the number of applications. The most important problems are the limited amount of output power, polarization instable emission (the subject of this thesis) and the difficulties to fabricate VCSELs operating at telecommunication wavelengths (1.3 μm-1.5 μm). Recent developments show that VCSELs operating at telecommunication wavelengths are still promising [6]. Metropolitan or local-area networks are expected to become the most important application of VCSELs [5]. In these networks, the low cost of VCSELs emitting at 850 nm is attractive.

1.2 Design and fabrication of VCSELs

Micro-cavity lasers, like VCSELs, are interesting because light is confined in a small volume of only a few cubic wavelengths. Confinement of the optical field in the vertical direction is obtained with high-reflectivity Bragg mirrors, whereas optical field confinement in the in-plane directions is achieved via current confinement. Current confinement is also needed for high energy conversion from electrical to optical power. In state-of-the-art VCSELs, the wall-plug efficiency is about 55 % [7]. In the first decade of VCSEL research important breakthroughs in design related the confinement have been made.

To achieve transverse confinement in VCSELs several fabrication techniques have been developed. Figure 1.2 shows the most common VCSEL designs. Originally, proton-implantation and etched-post confinement were used. In proton-

implanted VCSELs, the surroundings of the device are made insulating by a bombardment and implantation of hydrogen atoms, resulting in current confinement. In etched-post VCSELs, the current flow is restricted by etching away most of the VCSEL. A breakthrough in VCSEL designs was realized around 1994 [8], based on confinement by wet oxidation of AlAs [9]. In these oxide-confined VCSELs an extra thin AlAs-layer, typically 25 nm thick, is grown in the top DBR-mirror. As a next step the surrounding material is etched away, and the structure is oxidized from the etched sides to the center. Since the oxidation process is highly selective (the oxidation rate for AlAs is about five times larger than for $Al_{0.98}Ga_{0.02}As$), confinement is obtained only via the thin AlAs layer [10]. Oxidation of AlAs creates an insulating Al_2O_3 aperture, which confines the current. In addition the lower index of refraction of Al_2O_3, typically 1.5, results in confinement of the optical field. Oxide-confinement reduces optical scatter losses, and resulted in an impressive threshold current reduction of an order of magnitude, down to 0.5 mA. The performances of oxide-confined VCSELs are far better than that of proton-implanted and etched-post devices; for oxide-confined VCSELs the lowest threshold current [4], the highest output power [11] and the highest efficiency [7] have been reported. In this thesis, the polarization fluctuations of all three types of structures, as shown in Fig. 1.2, are addressed

proton-implanted   **etched-post**   **oxide-confined**

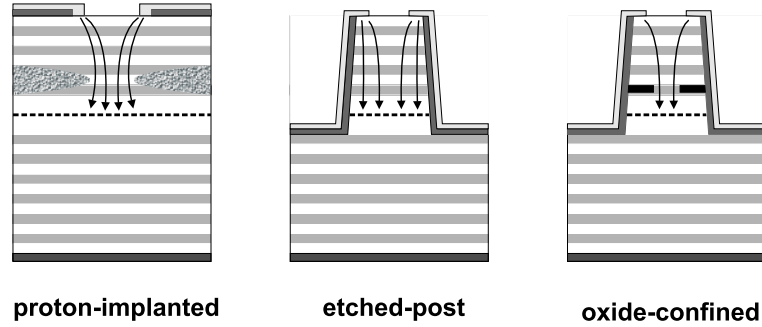**Figure 1.2**: Cross-section sketches of a proton-implanted VCSEL, an etched-post VCSEL, and an oxide-confined VCSEL. The arrows indicate the current flow in the devices.

1.3   Thesis overview

The central theme of this thesis is polarization fluctuation behaviour of VCSELs. This is interesting for several reasons. VCSELs have a high degree of rotational symmetry, leading to weak pinning of the polarization. On the other hand, the

source of polarization fluctuations is quantum noise. This quantum noise, resulting from (polarized) spontaneous emission, is known to be exceptionally strong for small lasers in general, and VCSELs in particular [12]. Although an ideal rotationally symmetric VCSEL would have no polarization preference, the polarization of practical VCSELs is generally observed to be linear with a strong orientation preference for the (orthogonal) crystalline [110] or [1$\bar{1}$0] axes. Polarization switches, where the polarization suddenly switches to the orthogonal polarization as a function of injection current, are often reported [13]. Understanding of polarization fluctuations is important from an application point of view. Uncontrolled polarization switches are an industrial nightmare, whereas polarization fluctuations will be converted into extra intensity noise by the unavoidable polarization dependence of the detection scheme in almost any conceivable application. In general, polarization projection always leads to a degradation of the signal-to-noise ratio. Proper knowledge of the time scale of polarization fluctuations, the statistics of polarization switching, and polarization intensity noise spectra is thus required.

Since the emission in practical VCSELs occurs in a linear polarization, the cylindrical symmetry is apparently broken. Mechanism of symmetry breaking are *(i)* cavity anisotropies [14] and/or *(ii)* anisotropies in the quantum-well gain medium. In the latter case, the Zeeman sub-levels of the conduction and valence bands are coupled to the optical field polarization via dipole transition selection rules [15].

This thesis presents a combined experimental and theoretical study of polarization fluctuations in VCSELs, where the emphasis is on understanding of practical devices. The experiments were performed on VCSELs from several suppliers with all the three different types of transverse confinement, as shown in Fig. 1.2. Proton-implanted VCSELs were obtained commercially [16]. Avalon Photonics (formerly CSEM) provided etched-post and oxide-confined VCSELs, whereas the Opto-Electronics group of the University of Ulm provided oxide-confined VCSELs.

The theoretical framework, with both symmetry-breaking mechanisms, is introduced in chapter 2. The complete theoretical model allows only numerical solutions, and therefore hinders an insightful comparison with the experiment. To facilitate this comparison we have reduced the full model to a stripped model in the two polarization degrees of freedom, namely the polarization direction angle ϕ and ellipticity angle χ. In turn, this two-dimensional model in ϕ and χ is reduced to a one-dimensional Kramers model for polarization noise. Subsequently analytical expressions for polarization fluctuations are derived. In chapter 2 these simplified models are validated experimentally, and it is demonstrated that the po-

larization fluctuations in ϕ and χ can be different due to symmetry breaking from the quantum-well gain medium.

These simplified models, as derived in chapter 2, are used as a starting point for studies of the polarization correlation and polarization switching in chapter 3-5. Chapter 3 describes a combined theoretical and experimental study of the correlation of polarization fluctuations and intensity noise. From an analysis of measured correlation functions, we conclude that the intensity and polarization fluctuations are decoupled. Chapter 4 addresses stochastic polarization switching, where the polarization continuously hops between two orthogonally linearly polarized components. By applying a controlled amount of strain, the hop-rates can be varied by 8 orders of magnitude; from 0.1 s^{-1} to 10^7 s^{-1}. This result agrees with an one-dimensional Kramers model for diffusion in a double well potential. The polarization switch or jump occurs on a faster nanosecond time scale. Chapter 5 addresses the nature of polarization switching in VCSELs. From time-resolved measurements of the Stokes polarization parameters during a polarization switch, we reconstruct the switch trajectory on the Poincaré sphere.

In chapter 6, the polarization excursions in VCSELs with either symmetry breaking due to an imperfect cylindrical symmetric cavity or symmetry breaking due to the quantum-well gain medium are discussed theoretically. It is demonstrated that for both limits the polarization excursions reduce to loxodromes.

Chapter 7 presents a combined analysis of the spectral and polarization impurity of a VCSEL. Both impurities, ultimately limited by the quantum noise, are demonstrated to exhibit anomalies around the lasing threshold.

In chapter 8, oxide-confined VCSELs with very small oxidation apertures are studied. The benefit of oxide-confinement, in comparison to etched-post confinement, is that this fabrication technique allows for transverse miniaturization without introducing large optical scattering losses. The emission was observed to occur in strongly chirped pulses; we show that this is a consequence of the strong confinement of small oxidation apertures.

Finally, the polarization properties of two-dimensional *arrays* of densely-packed VCSELs are addressed in chapter 9. VCSELs organized in densely-packed arrays will communicate with each other due to evanescent optical fields, leaking to neighbouring cavities. As a result of overlapping optical fields phase-coupling occurs, and all VCSELs will organize themselves in an overall energetically favourable mode, a so-called supermode. Neighbouring VCSELs in a square lattice will start to lase out-of-phase [17], which is similar to anti-ferromagnetic ordering of spins. Although such phase-coupled arrays have been realized in the early days of VCSEL research [18,19], continuous-wave operation was observed only recently [20]. By using a spectrally-resolved spatial-imaging technique, we

have demonstrated that the polarization of a single supermode emitted by a continuously operating phase-coupled array can be highly nonuniform.

Since all chapters have been written to be published as individual papers, it is possible to read each chapter separately. The consequence of this presentation is some overlap between chapters.

Chapter 2

Polarization fluctuations in vertical-cavity semiconductor lasers [1]

We report, theoretically and experimentally, how polarization fluctuations in vertical-cavity semiconductor lasers are affected by optical anisotropies. We develop a two-dimensional spin-eliminated (class A type) description of laser polarization and show how the various model parameters can be extracted from the experimental data. In practice, the linear anisotropies are often much stronger than the nonlinear anisotropies, so that the polarization modes defined by the linear anisotropies form a useful basis. For this case we derive a new one-dimensional model for polarization noise, with simple expressions for the relative strength of the polarization fluctuations. For the other, more extreme, case where the nonlinear anisotropies are as strong (or even stronger) than the linear anisotropies, the spin-eliminated description remains valid. However, in this case the concept of polarization modes is shown to lose its meaning, as a strong four-wave mixing peak appears in the optical spectrum and polarization fluctuations become highly nonuniform.

2.1 Introduction

Polarization fluctuations are present in all lasers, but are exceptionally strong in semiconductor vertical-cavity surface-emitting lasers (VCSELs). The reason for this is twofold. On the one hand, the spontaneous emission noise, which drives the polarization fluctuations, is relatively strong due to the limited size of the device. This is true for any semiconductor laser and leads, among others, to a relatively large quantum-limited laser linewidth [21]. On the other hand, the deterministic forces, being the optical anisotropies in the device, are relatively small due to the nominal cylindrical symmetry of a VCSEL. The combination of strong stochastic noise and weak restoring forces creates relatively large polarization fluctuations. A proper understanding of these fluctuations is clearly important from a practical

---

point of view; in any application of VCSELs polarization noise will be converted into intensity noise by the (unavoidable) polarization dependence of a practical detection system. Alternatively, and this is the emphasis of the present chapter, a study of these fluctuations constitutes a very useful tool to unravel the various anisotropies and other laser parameters of practical VCSELs. A preliminary study has appeared in ref. [22].

Up to recently, it was difficult to compare theory and experiments on VCSEL polarization. The "standard"theoretical model for the polarization of a quantum-well VCSEL is the "spin-flip model"or "split-inversion model", which describes the effect of the quantum-well gain medium on the polarization of the emitted light [15]. In this model the conduction and heavy-hole valence band are treated as four discrete levels, with $J_z = \pm\frac{1}{2}$ and $J_z = \pm\frac{3}{2}$, respectively, and the inversion is split into two transitions ($J_z = \frac{1}{2} \leftrightarrow \frac{3}{2}$ and $J_z = -\frac{1}{2} \leftrightarrow -\frac{3}{2}$), each interacting with circularly-polarized light of a specific handedness. An important parameter in this model is Γ, which describes the spin-flip relaxation between the two spin inversions (normalized to the inversion decay rate). So far experimental verification of this model has been difficult, as the spin-flip theory in its full generality allows only numerical treatment [15,23].

However, an experimental study of the optical spectrum revealed that the polarization properties of practical devices could almost completely attributed to linear anisotropies, *i.e.*, anisotropies due to symmetry-breaking of the almost cylindrical symmetric VCSEL cavity [24]. In practice, the effect of the gain medium or nonlinear anisotropies were thus found to be relatively small, corresponding to a large value of Γ. Based on this insight, simplified theoretical descriptions have been developed [25,26], in which the spin-inversion was eliminated adiabatically, and the rate equations were linearized around steady-state. The simplicity of the linearized spin-eliminated model allows for many analytic expressions; the model yields, among others, expressions for a nonlinear redshift and for excess damping of the nonlasing mode as compared to the lasing mode [25,27,26]. More recent predictions [26] concern the appearance of a third (four-wave mixing) peak in the optical spectrum and asymmetries in the polarization-resolved intensity noise.

Theoretically, this chapter constitutes an extension of the work on the spin-eliminated model reported in [25] and [26]. We will put special emphasis on the role of noise. The key issue is not so much *whether* the lasing polarization is stable, but rather *how* stable it is, what the stability eigenvalues are, and how much the polarization still fluctuates around its equilibrium value. We hereby derive many useful expressions for VCSEL polarization noise, that allow for easy comparison with experiment. As a further extension, we will go beyond the linearized theory, concentrating on the practical case that linear birefringence is the

dominant anisotropy, and develop a new one-dimensional model for polarization fluctuations in VCSELs.

Experimentally, we report a multitude of data on VCSEL polarization noise. By analyzing the measured polarization fluctuations, which can be exceptionally strong in VCSELs, we extract a series of VCSEL parameters, with emphasis on the various optical anisotropies. By comparison of the experiments performed on different VCSEL-designs, *i.e.*, proton-implanted VCSELs, etched-post VCSELs and oxide-confined VCSELs, we demonstrate the generality of our results.

We focus on three experimental tools to study the polarization fluctuations. The first tool is a measurement of the polarization-resolved optical spectrum, where polarization fluctuations show up in the form of additional spectral peaks with a polarization different from that of the lasing peak. The second tool is a measurement of the polarization-resolved intensity noise, a polarization-type of homodyne detection, suggested in ref. [26] and first demonstrated in [22], in which the intensity noise, after polarization projection of the VCSEL output, is frequency analyzed. We will show how this new technique provides information on the polarization fluctuations. As a third tool we employ a time-domain study of the polarization-resolved intensity.

In Section 2.2, we will review the spin-flip model [15]. In Section 2.3 we will introduce the adiabatic model for the polarization dynamics of VCSELs. In doing so we will generalize the earlier theory to the case of nonaligned birefringence and dichroism. After discussing the various parameters in the problem, we will show how their magnitude can be determined from experimental data. To facilitate the comparison between theory and experiment, Sections 2.4 and 2.5 present several useful expressions for the polarization-resolved optical spectrum, and the polarization-resolved intensity noise, respectively. In Section 2.6 we isolate the case where the linear birefringence dominates over all other anisotropies; this is the case encountered for almost any practical VCSEL. We will show how in this case the adiabatic description in terms of two polarization variables can be reduced even further, to a simple one-dimensional description, with an appealing expression for the relative strength of the polarization modes. In Sections 2.7-2.11 we will present and analyze our experimental data on proton-implanted VCSELs, organized via the three basic techniques that we use. In Section 2.7 we discuss the experimental setup, in Section 2.8 the polarization-resolved optical spectra, in Section 2.9 the polarization-resolved intensity noise, and in Section 2.10 the polarization switches that occur in some VCSELs. In Section 2.11 we will discuss results for VCSELs with a different design: etched-post VCSELs and oxide-confined VCSELs. Section 2.12 summarizes the results and gives an overall conclusion.

2.2   Spin-flip theory

In this section, we will review the spin-flip model that describes the polarization dynamics of quantum-well VCSELs [15], and that is the starting point of our theoretical analysis. In the spin-flip model, the band structure as well as the vectorial nature of the optical field are incorporated. Figure 2.1a shows the band structure of a semiconductor quantum well, with its conduction and valence bands. The electrons at the center of the conduction band have a total angular momentum $J = 1/2$. There are three valence bands: the split-off band, the light-hole band, and the heavy-hole band. Since the split-off band, with total angular momentum $J = 1/2$, has a lower energy it is not taken into account [15]. For bulk material the heavy-hole and light-hole valence band, with total angular momentum $J = 3/2$, are degenerated at the center of the bandgap. Due to the confinement of the quantum well in the z-direction, the degeneracy of the heavy-hole band and light-hole band is lifted, with the heavy-hole band having the highest energy. As a complete
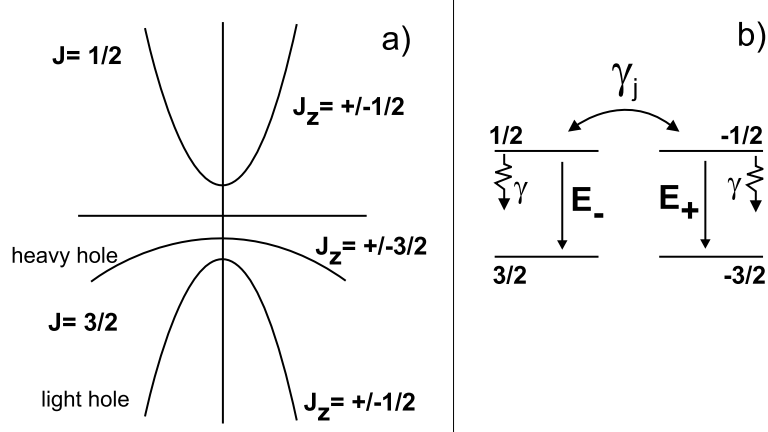
Figure 2.1: Typical band structure of a GaAs quantum well (a). Approximation of the conduction band and heavy-hole valence band by four discrete spin-levels (b). The inversion is split into two transitions $J_z = \frac{1}{2} \leftrightarrow \frac{3}{2}$ and $J_z = -\frac{1}{2} \leftrightarrow -\frac{3}{2}$, each interacting with a circularly polarized component of the optical field E_- and E_+, respectively. The inversion of the transitions are coupled via the spin-flip rate γ_j.

inclusion of the band structure is far too complicated, the light hole band with its lower energy is neglected, *i.e.*, assumed to be completely filled [15]. Moreover, in the spin-flip theory the band structure of the heavy-hole and conduction band are approximated by four discrete spin levels at the center of the band gap [15]. Due to conservation of angular momentum, the allowed dipole transitions are $\Delta J_z = \pm 1$,

corresponding to two transitions $J_z = \frac{1}{2} \leftrightarrow \frac{3}{2}$ and $J_z = -\frac{1}{2} \leftrightarrow -\frac{3}{2}$. Figure 2.1b shows how these four discrete spin levels interact pair-wise with the circularly polarized components of the optical field E_+ and E_-. The spin-flip model uses two spin reservoirs, each with an inversion N_+ and N_-, which are coupled due to spin-relaxation, modeled by the spin-flip rate γ_j [15]. The spin inversions N_+ and N_- can be rewritten as an average inversion $N = (N_+ + N_-)/2$ and a spin-difference inversion $n = (N_+ - N_-)/2$, and are normalized with respect to a threshold inversion, for which the gain exactly compensates the average optical cavity loss. This interaction scheme results in the following set of deterministic rate-equations for the optical field $\vec{E}$, the average inversion N, and the spin-difference inversion n [15,23]

$$\frac{dE_+}{dt} = -\frac{1}{2}(\gamma_{\parallel} + i\omega_{\mathrm{lin}})E_+ + \kappa(1 - i\alpha)[(N-1) + n]E_+ , \qquad (2.1a)$$

$$\frac{dE_-}{dt} = -\frac{1}{2}(\gamma_{\parallel} + i\omega_{\mathrm{lin}})E_+ + \kappa(1 - i\alpha)[(N-1) - n]E_- , \qquad (2.1b)$$

$$\frac{dN}{dt} = -\gamma[(N - 1 - \mu) + (|E_+|^2 + |E_-|^2)N + (|E_+|^2 - |E_-|^2)n] , (2.1c)$$

$$\frac{dn}{dt} = -\gamma_s n - \gamma[(|E_+|^2 + |E_-|^2)n + (|E_+|^2 - |E_-|^2)N] . \qquad (2.1d)$$

The split-flip model contains three decay rates: the decay rate κ for the optical field, the decay rate γ for the average inversion N, and the decay rate γ_s for the difference inversion n, where $\gamma_s = 2\gamma_j + \gamma$. The parameter $\mu + 1$ is the injection current normalized to the threshold current, and α is the linewidth enhancement factor [21]. In a practical laser the rotational polarization symmetry is generally broken by linear anisotropies, $i.e.$, anisotropies that are independent of laser power. In the absence of a magnetic field there can be only two of these: a birefringence ω_{lin} and a dichroism $\gamma_{\parallel} = \gamma_{\mathrm{lin}} \cos 2\beta$ [28,29]. As these anisotropies have a directionality, we also need the angle β between the axes of linear dichroism and linear birefringence. Note that the linear birefringence and linear dichroism both have a sign, being positive when the lasing mode has the highest frequency and highest linear gain, respectively.

Unfortunately, the spin-flip model is rather complicated, as the dynamics of two population inversions has to be accounted for, so that analytic approaches are very difficult. Numerical studies have concentrated on the issue of polarization stability, depicted in so-called stability diagrams, and more specifically on polarization switching and bistability [23,25,28]. Although polarization switching has been observed in several experiments, a quantitative comparison with theory proved to be difficult, due to the numerical methodology and due to the fact that only limited information could be extracted from the experiments reported

so far [13,30]. Also, alternative explanations for polarization switches seemed equally likely [13].

Other experimental studies involved the optical spectra of light emitted by VCSELs [24]. In general, these spectra consist of two (Lorentzian-shaped) components, a strong "lasing mode"and a weak "nonlasing mode"with orthogonal polarization, the two components being related to the two VCSEL polarizations. The differences in centre frequency and spectral width between these two components could be almost completely attributed to linear anisotropies; only small deviations between experiment and a linear "coupled-mode"model hinted at more complicated population dynamics [24]. A reconciliation between experiment and theory came with a simplified theoretical description, which was concurrently developed by several authors [25,27,26], in which the spin inversion was adiabatically eliminated from the laser rate equations.

2.3 Adiabatic description of polarization fluctuations; 2D-description of polarization fluctuations

In this section, we discuss the adiabatic elimination of the spin-difference inversion [25,27,26]. The validity condition for the adiabatic elimination has been thoroughly discussed in [25]: the polarization of the optical field should vary slowly as compared to the medium response to polarization changes. This means that *(i)* the optical anisotropies should not be too large, as these set the time scale of polarization changes, and *(ii)* the normalized spin-decay rate $\Gamma = \gamma_s/\gamma$ should be large enough, as this sets the time scale of the medium response. Adiabatic elimination of the spin-difference inversion n in Eqs. (2.1a-c) yields the following set of rate-equations for the optical field $\vec{E}$ and the average inversion N

$$
\begin{aligned}
\frac{dE_x}{dt} &= \frac{1}{2}(i\omega_{\text{lin}} + \gamma_\parallel)E_x + \kappa(1 - i\alpha)(N-1)E_x \\
&\quad - \frac{\kappa}{\Gamma}(1 - i\alpha)[|E_y|^2 E_x + E_y^2 E_x^*] \,,
\end{aligned} \tag{2.2a}
$$

$$
\begin{aligned}
\frac{dE_y}{dt} &= -\frac{1}{2}(i\omega_{\text{lin}} + \gamma_\parallel)E_y + \kappa(1 - i\alpha)(N-1)E_y \\
&\quad - \frac{\kappa}{\Gamma}(1 - i\alpha)[|E_x|^2 E_y + E_x^2 E_y^*] \,,
\end{aligned} \tag{2.2b}
$$

$$
\begin{aligned}
\frac{dN}{dt} &= -\gamma(N - 1 - \mu) - \gamma(|E_x|^2 + |E_y|^2)N \\
&\quad + \frac{\gamma}{\Gamma}[2|E_x|^2|E_y|^2 - E_x^2(E_y^*)^2 - (E_x^*)^2 E_y^2] \,,
\end{aligned} \tag{2.2c}
$$

   The third-order terms in the optical field at the rhs of Eqs. (2.2a-b) are the remnants of the eliminated spin-difference inversion, which act as a nonlinear anisotropies. The effect of these nonlinear anisotropies is that the saturation power for linearly-polarized light is (slightly) larger than for circularly-polarized light, and that four-wave mixing peaks can be generated.

   The optical field in Eqs. (2.2a-b) is written in terms of the complex field components E_x and E_y. However, from an experimental point of view it is convenient to describe the optical field vector with four real-valued variables, instead. The first variable is a common phase factor (the phase of the laser field φ_l), which exhibits a diffusive evolution that has no consequences for the other dynamics. The other variables are: the optical intensity $I = |\vec{E}|^2$, and two angles ϕ and χ that characterize the optical polarization [31], where ϕ ($0 \leq \phi \leq \pi$) is the direction of the polarization ellipse and χ ($-\pi/4 \leq \chi \leq \pi/4$) is the ellipticity angle. The polarization state can be represented on the Poincaré sphere using ($2\phi, 2\chi$) as spherical coordinates (see Fig. 2.2). On the Poincaré sphere, the polarization in the equatorial plane is linear, the poles correspond to circularly-polarized light, whereas the polarization on the hemispheres is elliptical. Along the Cartesian axes of this sphere the Stokes parameters ($s_1 = \cos(2\chi)\cos(2\phi)$, $s_2 = \cos(2\chi)\sin(2\phi)$, $s_3 = \sin(2\chi)$) are plotted.

   For practical VCSELs the output polarization is practically always close to linear, in a direction that we can define to be the x-axis. Linearization around this point yields:

$$\vec{E} \approx (\vec{e}_x - (\phi + i\chi)\vec{e}_y)\,|\vec{E}|e^{-i\varphi_l}\,. \tag{2.3}$$

The rate-equations after spin-elimination [Eqs. (2.2a-c)] can now be linearized with Eq. (2.3). In earlier work the linear birefringence and linear dichroism were often assumed to be aligned, resulting in VCSEL eigenmodes that are linearly-polarized along the common axes of birefringence and dichroism. We now generalize this approach, allowing the axes of linear birefringence and linear dichroism to make an arbitrary angle β. In Appendix A the full expressions for this general case, from [28,29,32], are rewritten into the following linearized polarization rate equations:

$$\frac{d}{dt}\begin{pmatrix} \phi - \phi_{ss} \\ \chi - \chi_{ss} \end{pmatrix} = \begin{pmatrix} -\gamma_\parallel & -\omega_{lin} - 2\alpha\gamma_{non} \\ \omega_{lin} & -\gamma_\parallel - 2\gamma_{non} \end{pmatrix} \begin{pmatrix} \phi - \phi_{ss} \\ \chi - \chi_{ss} \end{pmatrix} + \begin{pmatrix} f_\phi \\ f_\chi \end{pmatrix}, \tag{2.4}$$

where ϕ_{ss} and χ_{ss} are steady-state angles, and f_ϕ and f_χ are Langevin noise sources. The eliminated spin-difference inversion, that gives rise to polarization-dependent saturation, is now represented by two nonlinear anisotropies ω_{non} and

γ_{non}. The magnitude of the nonlinear anisotropies is $\gamma_{\mathrm{non}} = \kappa I/\Gamma$ for the nonlinear dichroism (absorptive saturation) and $\omega_{\mathrm{non}} = \alpha\gamma_{\mathrm{non}}$ for the nonlinear birefringence (dispersive saturation). These nonlinear anisotropies are proportional to the intra-cavity intensity I, which has been normalized with respect to the saturation intensity and which for an ideal four-level laser is thus equal to the normalized pump parameter μ [25].

For completeness we note that the polarization dynamics (ϕ, χ) is only coupled to the intensity I via γ_{non}. This coupling disappears when the intensity is reasonably constant, *i.e.*, when fluctuations are limited or at frequencies very different from those of the polarization dynamics, so that one can substitute the average intensity. This leads to a first-order separation of the polarization and intensity/inversion dynamics, so that the polarization dynamics of a VCSEL is that of a class A laser, although the intensity dynamics is still that of a class B laser (with relaxation oscillations) [33,34]. A summary of the parameters that we use is given in table 2.1.

The misalignment of the linear birefringence ω_{lin} and linear dichroism γ_{lin} is found to result in two changes: *(i)* the steady-state polarization ceases to be linear and obtains an average ellipticity χ_{ss} [where we consider only $\chi_{\mathrm{ss}} \ll 1$, see Eq. (A.2a)], and *(ii)* the polarization dynamics is now determined by the projected linear dichroism $\gamma_{\parallel} = \gamma_{\mathrm{lin}} \cos 2\beta$.

Furthermore we note that, in some aspects, the validity range of Eq. (2.4) surpasses that of the underlying split-inversion model. Namely, through adiabatic elimination we have reduced our description to a general third-order Lamb theory for the laser polarization, which is valid for any class A with rotational symmetry [25]. In this sense Eq. (2.4) is quite general; it is only the interpretation of the nonlinear anisotropies γ_{non} and ω_{non}, as $\gamma_{\mathrm{non}} = \kappa I/\Gamma$ and $\omega_{\mathrm{non}} = \alpha\gamma_{\mathrm{non}}$, that is specific for the spin-flip model.

The eigenvalues of the above equation [Eq. (2.4)] are $\lambda = -\gamma_0 \pm i\omega_0$, with:

$$\gamma_0 = \gamma_{\parallel} + \gamma_{\mathrm{non}} , \tag{2.5a}$$

$$\omega_0 = \sqrt{\omega_{\mathrm{lin}}^2 + 2\omega_{\mathrm{lin}}\alpha\gamma_{\mathrm{non}} - \gamma_{\mathrm{non}}^2}$$

$$= \sqrt{(\omega_{\mathrm{lin}} + \alpha\gamma_{\mathrm{non}})^2 - (\alpha^2 + 1)\gamma_{\mathrm{non}}^2} , \tag{2.5b}$$

where ω_0 and γ_0 contain the combined action of linear and nonlinear effects and will thus be called the *effective* birefringence and *effective* dichroism, respectively, and where the nonlinear terms corresponds to a "spectral redshift" and "excess broadening" of the nonlasing peak as compared to the lasing peak [25,27,26]. The

Table 2.1: Important parameters and variables, together with their symbol and units.

Parameter or variable	Symbol	Units
- linear birefringence	ω_{lin}	ns^{-1}
- linear dichroism	γ_{lin}	ns^{-1}
- projected linear dichroism	$\gamma_{\parallel} = \gamma_{\text{lin}} \cos 2\beta$	ns^{-1}
- angle between linear birefringence and linear dichroism	β	rad
- nonlinear birefringence	$\omega_{\text{non}} = \alpha \gamma_{\text{non}}$	ns^{-1}
- nonlinear dichroism	γ_{non}	ns^{-1}
- linewidth enhancement factor	α	-
- effective birefringence	$\omega_0 = 2\pi\nu_0$	ns^{-1}
- effective dichroism	$\gamma_0 = \gamma_{\parallel} + \gamma_{\text{non}}$	ns^{-1}
- cavity loss rate (of intra-cavity optical field)	κ	ns^{-1}
- loss rate of average inversion	γ	ns^{-1}
- loss rate of difference inversion	γ_{s}	ns^{-1}
- normalized spin decay rate	$\Gamma = \gamma_s / \gamma$	-
- noise strength	$D = n_{\text{sp}} \kappa / S$	ns^{-1}
- spontaneous emission factor	n_{sp}	-
- number of photons in fundamental cavity mode	S	-
- intra-cavity intensity (normalized to saturation)	I	-
- optical phase	φ_l	rad
- polarization orientation angle	ϕ	rad
- polarization ellipticity angle	χ	rad
- rotationally averaged polarization angle	φ	rad

corresponding eigenvectors are:

$$\begin{pmatrix} \omega_{\text{lin}} + 2\alpha\gamma_{\text{non}} \\ \mp i\omega_0 + \gamma_{\text{non}} \end{pmatrix} \approx \omega_0 \begin{pmatrix} 1 \\ \mp i \end{pmatrix} + \begin{pmatrix} \alpha\gamma_{\text{non}} \\ \gamma_{\text{non}} \end{pmatrix}, \qquad (2.6)$$

where the approximate expression is valid for $\omega_0 \gg \sqrt{\alpha^2 + 1}\,\gamma_{\text{non}}$.

The main reason for writing down the above eigenvectors [Eq. (2.6)] is that these already show the intrinsic polarization dynamics, *i.e.*, the response to a perturbation without noise. In the absence of nonlinear anisotropies, *i.e.*, for $\gamma_{\text{non}} = 0$,

the dynamics is extremely simple: on the Poincaré sphere the polarization (ϕ, χ) will evolve along a spiral-like curve towards steady state. In terms of optical amplitudes this means that there is a (steady-state) lasing mode and an (orthogonally-polarized) nonlasing mode that gradually decays to zero. The rotation on the Poincaré sphere is counterclockwise for the case $\omega_0 > 0$, where the dominant x-polarized mode has the highest frequency.

In the presence of nonlinear anisotropies the situation becomes more interesting. Equation (2.6) shows that the amplitudes in the ϕ and χ directions will then be different, so that the evolution is now along an *elliptical* spiral-like trajectory. As a consequence, fluctuations in the laser's polarization direction ϕ are expected to have a different magnitude than fluctuations in the ellipticity χ. As another consequence a third peak is expected to appear in the optical spectrum. This is because the mentioned trajectory can be decomposed in a clockwise and counter-clockwise circular trajectory, which correspond to spectral peaks on the high and low-frequency side of the lasing peak, respectively [22,26]. The approximate amplitude of these components can be easily found from Eq. (2.6).

Equation (2.4) shows how polarization fluctuations result from a balance between the stochastic driving force of polarization noise and the damping and spectral deformation caused by the various anisotropies. The polarization noise is a manifestation of the quantum noise that results from the discrete character of photons and carriers. For practical VCSELs $\kappa/\gamma \gg 1$, so that photon noise dominates, as the average number of inverted carrier states is much larger than the average photon number. As photon noise originates from random spontaneous emission of photons with arbitrary phase and arbitrary polarization (since $N_+ \approx N_-$), the complex noise vector $\vec{f}(t)$ comprises four independent real-valued numbers, that can be divided into phase noise, intensity noise, and two forms of polarization noise. Phase and amplitude noise are best known as they also occur in the single-mode (scalar) problem. The two polarization components are similar uncorrelated real-valued Langevin noise sources of identical strength, which satisfy:

$$< f_\chi(t_1) f_\chi(t_2) > \quad = \quad < f_\phi(t_1) f_\phi(t_2) > = D\,\delta(t_1 - t_2)\,, \tag{2.7a}$$

$$< |f_\chi(\omega)|^2 > \quad = \quad < |f_\phi(\omega)|^2 > = D = n_{\mathrm{sp}}\,\kappa/S\,, \tag{2.7b}$$

where the noise strength, or diffusion rate D, is inversely proportional to the photon number S and proportional to the product of cavity loss rate κ and spontaneous emission factor n_{sp} ($n_{\mathrm{sp}} \geq 1$ results from incomplete inversion as determined by the finite temperature, which smoothens the sharpness of the Fermi-Dirac distribution) [33].

One way to solve the polarization rate equations (2.4) is via Green functions that are based on the eigenvectors of Eq. (2.6); this was done in [26]. An easier way is to apply a Fourier transformation and solve the equations in the frequency domain, to obtain:

$$\phi(\omega) = \frac{(i\omega - \gamma_\parallel - 2\gamma_{\mathrm{non}})f_\phi(\omega) + (\omega_{\mathrm{lin}} + 2\alpha\gamma_{\mathrm{non}})f_\chi(\omega)}{(\omega - \omega_0 - i\gamma_0)(\omega + \omega_0 - i\gamma_0)} , \qquad (2.8a)$$

$$\chi(\omega) = \frac{-\omega_{\mathrm{lin}}f_\phi(\omega) + (i\omega - \gamma_\parallel)f_\chi(\omega)}{(\omega - \omega_0 - i\gamma_0)(\omega + \omega_0 - i\gamma_0)} . \qquad (2.8b)$$

By combining these equations with the expressions for the polarization noise [Eqs. (2.7a-b)] it is relatively straightforward to calculate the experimentally accessible polarization-resolved optical spectra and intensity noise. This will be done in Sec. 2.4 and Sec. 2.5, respectively.

2.4 Polarization-resolved optical spectra

In this section we will calculate the optical spectrum $|E(\omega)|^2$ of the VCSEL light, as measured after polarization projection. In the linearized description, *i.e.*, for $\phi, \chi \ll 1$, the projection onto the dominant polarization depends only on the dynamics of the optical phase and intensity (see below). On the other hand, if we block this light and project onto the orthogonal polarization, we obtain different information, namely on the polarization dynamics. The optical spectrum thus observed is the Fourier transformation of $E_y(t) \approx -\{\phi(t) + i\chi(t)\}E(t)\exp(-i\varphi_l(t))$, where $E(t) \equiv |\vec{E}(t)| \approx |E_x(t)|$. For convenience, we will first assume the optical field and optical phase to be constant at $E(t)\exp(-i\varphi_l(t)) = E_0$; later we will remove this restriction. In this practical case, the *y*-polarized spectrum is dominated by the polarization dynamics, so that:

$$< |E_y(\omega)|^2 > \approx E_0^2 < |\phi(\omega) + i\chi(\omega)|^2 >$$
$$= DE_0^2 \frac{(\omega - \omega_{\mathrm{lin}})^2 + (\omega - \omega_{\mathrm{lin}} - 2\alpha\gamma_{\mathrm{non}})^2 + \gamma_\parallel^2 + (\gamma_\parallel + 2\gamma_{\mathrm{non}})^2}{(\omega^2 - \omega_0^2 - \gamma_0^2)^2 + 4\gamma_0^2\omega^2} . \quad (2.9)$$

This optical spectrum generally consist of two peaks: a strong peak at $\omega \approx -\omega_0$, which corresponds to the "nonlasing mode" in the coupled-mode description [24], and a (much weaker) peak at $\omega \approx \omega_0$, which is produced in a polarization-type of four-wave mixing (FWM) between the *y*-polarized peak at $\omega \approx -\omega_0$ and the dominant *x*-polarized peak at $\omega = 0$ [22]. The *y*-polarized spectrum can be approximated as the sum of two Lorentzian curves with the same width when $\omega_0 \gg \gamma_0$. The position and width (HWHM = Half Width at Half Maximum) of the two peaks

yield the effective birefringence ω_0 and the effective dichroism γ_0, respectively. The intensity of the FWM peak, relative to that of the nonlasing peak, can then be used to estimate the combined (dispersive and absorptive) nonlinear anisotropy $(\alpha^2 + 1)\gamma_{\text{non}}^2$ via:

$$\frac{< |E_y(\omega_0)|^2 >}{< |E_y(-\omega_0)|^2 >} \approx \frac{(\alpha^2 + 1)\gamma_{\text{non}}^2}{4\omega_0^2} + \frac{\gamma_0^2}{4\omega_0^2} , \qquad (2.10)$$

where the second term results from the Lorentzian wing of the nonlasing peak at the position of the FWM peak. Note that a decomposition of the eigenvectors [Eq. (2.6)] in their cw and ccw components gives the same approximate result.

It is relatively easy to go beyond the approximation of "constant $E(t)$ and $\varphi_l(t)$", by noting that the polarization-resolved optical field is the *product* of the field $E(t) \exp(-i\varphi_l(t))$ and a function of (ϕ, χ). As a result, in the general case the polarization-resolved spectrum equals the *convolution* of the ideal spectrum [Eq. (2.9)] with the spectrum $|E(\omega)^2| \approx |E_x(\omega)|^2$, as measured for projection onto the dominant polarization. The shape of the latter is similar to that of "edge-emitting" lasers: it has a finite (Schawlow-Townes) laser linewidth γ_{lase}, due to diffusion of the optical phase, and (generally very weak) sidebands due to relaxation oscillations [34]. After convolution one thus finds that phase diffusion broadens all spectral peaks by an equal amount γ_{lase}, being the (HWHM) spectral width of $|E_x(\omega)|^2$, but that it does not affect the relative strength of the FWM peak as compared to the nonlasing peak, since these have the same (intrinsic) width (for $\omega_0 \gg \gamma_0$).

2.5 Polarization-resolved intensity noise

Next we will discuss the polarization-resolved intensity noise. A measurement of this projected noise is extremely simple: the laser light is passed through a rotateable $\lambda/4$ waveplate and subsequently through a rotateable polarizer, to project $\vec{E}(t)$ onto a selectable polarization state, after which the projected intensity noise is measured. Projection onto the dominant x or orthogonal y polarization yields information about the "polarization-mode partition noise" [35]. The intensity noise in the orthogonal y projection is generally rather small, being second order in ϕ and χ [see Eq. (2.3)]. A much stronger signal, *i.e.*, first order in ϕ and/or χ, is found for projection onto a "mixed" polarization like $x + y$ or $x + iy$. Such a projection constitutes a polarization homodyne detection, because it allows one to observe beats between the x-polarized lasing peak and the y-polarized nonlasing and FWM peaks [26]. Through these intensity beats, which go unnoticed without

projection, one gets a quantitative measure for the polarization fluctuations in the laser.
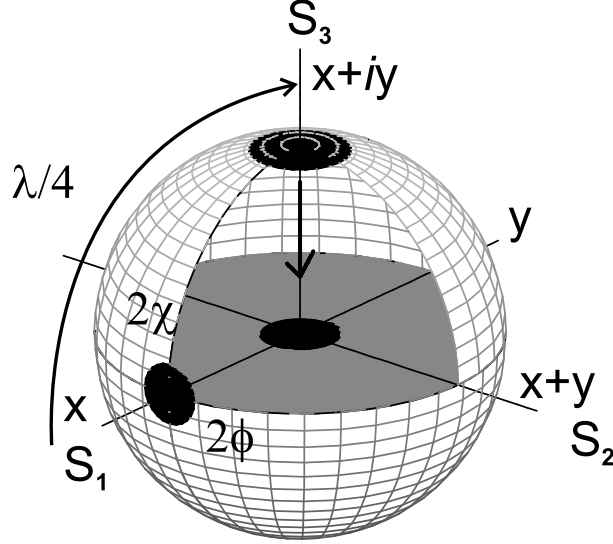

Figure 2.2: Principle of noise projection on the Poincaré sphere. The polarization fluctuations around the, almost linearly polarized, steady-state are presented as a noise cloud around a position close to the equator. Propagation through a $\lambda/4$-plate and polarizer results in a 90° rotation towards the north pole and a projection downwards onto a line, the orientation of which depends on polarizer angle. By projecting onto axis s_1 or s_2 we can measure the noise in the Poincaré angles χ or ϕ, respectively.

An appealing picture of the principle behind polarization projection arises on the Poincaré sphere, where each polarization state is depicted as a single point, *i.e.*, the normalized Stokes vector $(s_1, s_2, s_3) \equiv (\cos 2\chi \cos 2\phi, \cos 2\chi \sin 2\phi, \sin 2\chi)$. On the Poincaré sphere, the polarization evolution is represented by a timetrace and polarization fluctuations by a "noise cloud". Figure 2.2 sketches how, for dominantly *x*-polarized light, this noise cloud is located in the neighbourhood of the equator at $\phi, \chi \ll 1$. When the light is passed through a $\lambda/4$ plate, with its axes at 45° with respect to the dominant laser polarization, this noise cloud is rotated by 90° on the sphere, to end up around the north pole (right-handed circular polarization). The projected intensity behind a consecutive polarizer can now be found graphically by projection of the polarization state onto an axis passing through equator and centre of the Poincaré sphere, with an orientation that depends on the polarizer angle. When the polarizer axis is aligned with that of

the lasing mode one projects onto axis s_1 in Fig. 2.2 and measures $I_{\text{project}}(t) = (I/2)(1 + \sin 2\chi) \approx (I(t)/2)(1 + 2\chi(t))$. When the polarizer axis is aligned under $45°$ one projects onto axis s_2 and measures $I_{\text{project}}(t) \approx (I(t)/2)(1 + 2\phi(t))$. Other orientations give linear combinations of these results.

After this discussion, a calculation of the polarization-resolved intensity noise is straightforward. When the overall intensity is stable enough, the projected noise will be determined by the polarization dynamics only, so that the relative intensity noise, for projection onto the ϕ or χ direction respectively, is given by:

$$
\frac{<|\Delta I_{\text{project}}(\omega)|^2>}{<I_{\text{project}}>^2} = 4 <|\phi(\omega)|^2>
$$

$$
= 4D \left(\frac{\omega^2 + (\omega_{\text{lin}} + 2\alpha\gamma_{\text{non}})^2 + (\gamma_{\parallel} + 2\gamma_{\text{non}})^2}{(\omega^2 - \omega_0^2 - \gamma_0^2)^2 + 4\gamma_0^2\omega^2} \right) , \qquad (2.11a)
$$

$$
\frac{<|\Delta I_{\text{project}}(\omega)|^2>}{<I_{\text{project}}>^2} = 4 <|\chi(\omega)|^2>
$$

$$
= 4D \left(\frac{\omega^2 + \omega_{\text{lin}}^2 + \gamma_{\parallel}^2}{(\omega^2 - \omega_0^2 - \gamma_0^2)^2 + 4\gamma_0^2\omega^2} \right) . \qquad (2.11b)
$$

For the case of relatively large birefringence ($\omega_0 \gg \gamma_0, \gamma_{\text{non}}, \alpha\gamma_{\text{non}}$), these projected noise spectra are quite similar, both peaking around ω_0 and having a spectral width of γ_0 (HWHM). From fits to these spectra one can directly obtain the effective birefringence ω_0 and effective dichroism γ_0, without the experimental complication of a finite laser linewidth γ_{lase} that occurs when analyzing the optical spectra.

Interestingly enough, the above spectra have the same functional form as the relative intensity noise (RIN) spectrum. When the intensity fluctuations are relatively small, so that the intensity rate equation can be linearized, this RIN spectrum is given by:

$$
\frac{<|I(\omega)|^2>}{I_0^2} = 4D \frac{\omega^2 + 4\gamma_{\text{ro}}^2}{(\omega^2 - \omega_{\text{ro}}^2)^2 + 4\gamma_{\text{ro}}^2\omega^2} , \qquad (2.12)
$$

where ω_{ro} and γ_{ro} are the relaxation oscillation frequency and damping rate, respectively [33]. As the diffusion rate D is the same in Eqs. (2.11a-b) and (2.12), the relative strengths of the polarization fluctuations as compared to the intensity fluctuations is approximately equal to the ratio of the relaxation decay rate γ_{ro} over the polarization decay rate γ_0, where low damping corresponds to a sharp resonance and large fluctuations.

Once more it is relatively easy to generalize the expressions for the projected polarization noise to beyond the approximation of stable intensity. In the common

case of relatively small intensity and polarization fluctuations ($D \ll \gamma_0, \gamma_{\text{ro}}$), the time-dependent part of the projected intensity is approximately $\frac{1}{2}\Delta I(t) + I_0\chi(t)$ or $\frac{1}{2}\Delta I(t) + I_0\phi(t)$, where $\Delta I(t)$ is the deviation from the average intensity I_0. As the intensity and polarization fluctuations are practically uncorrelated, apart from minor interactions via the dichroism γ_{lin} and γ_{non}, the general projected noise spectrum is equal to the sum of the ideal polarization noise spectrum [Eqs. (2.11a-b)] and the (scaled) intensity noise spectrum, as measured without polarization projection [Eq. (2.12)].

The difference between the ϕ and χ projections, *i.e.*, between Eq. (2.11a) and (2.11b), is a measure for the ellipticity of the noise cloud on the Poincaré sphere:

$$\frac{<|\phi(\omega)|^2>}{<|\chi(\omega)|^2>} = \frac{\omega^2 + (\omega_{\text{lin}} + 2\alpha\gamma_{\text{non}})^2 + (\gamma_{\parallel} + 2\gamma_{\text{non}})^2}{\omega^2 + \omega_{\text{lin}}^2 + \gamma_{\parallel}^2} \, , \qquad (2.13)$$

and can be used to estimate the nonlinear anisotropies γ_{non} and $\alpha\gamma_{\text{non}}$. For relatively large linear birefringence ($\omega_{\text{lin}} \gg \gamma_{\parallel}, \gamma_{\text{non}}, \alpha\gamma_{\text{non}}$) the ratio displayed in Eq. (2.13) approaches unity and the exact result can be approximated as:

$$\frac{<|\phi(\omega)|^2>^{\frac{1}{2}}}{<|\chi(\omega)|^2>^{\frac{1}{2}}} \approx 1 + \frac{2\alpha\gamma_{\text{non}}}{\omega_0}\left(\frac{\omega_0^2}{\omega_0^2 + \omega^2}\right) \, , \qquad (2.14)$$

where we have introduced square roots to facilitate a comparison with the experimental signal on the RF-analyzer [22]. Equation (2.14) shows that the nonuniformity of the polarization fluctuations depends on frequency, being relatively large for $\omega \leq \omega_0$ and disappearing for $\omega \gg \omega_0$. This aspect was apparently overlooked in the time domain analysis in [26], because that analysis neglected the nonorthogonality of the eigenvectors [Eq. (2.6)].

When linear birefringence is not the dominant anisotropy the analysis becomes more complicated. In principle one should use the exact result Eq. (2.13) instead of the approximate expression Eq. (2.14). A problem is that the exact result Eq. (2.13), which can be written as $(\omega^2 + C_\phi)/(\omega^2 + C_\chi)$, is complicated, because the C-coefficients contain many unknowns. A rewrite as

$$\alpha\gamma_{\text{non}} = \frac{\omega_0}{2}\frac{C_\phi - C_\chi}{C_\phi + C_\chi}\left(\frac{1 + [2(\alpha^2 + 1)\gamma_{\text{non}}^2 + \gamma_0^2]/\omega_0^2}{\sqrt{1 + (\alpha^2 + 1)\gamma_{\text{non}}^2/\omega_0^2} + \gamma_0/(\alpha\omega_0)}\right) \qquad (2.15)$$

provides some help, as in practical cases (see section 2.9) the complicated factor within parentheses is generally very close to unity. In the experimental analysis we will first neglect this correction factor, and substitute the fitted C_ϕ and C_χ into

Eq. (2.15) to derive the nonlinear anisotropy $\alpha\gamma_{\mathrm{non}}$. As a next step we resubstitute the obtained result (and assume that $\alpha \gg 1$) for a somewhat better second estimate.

The fluctuations in ϕ and χ are not independent, but correlated [26]. As a result, the projected polarization noise will have extrema for directions different from the ϕ and χ-axes. To find the rotation angle Ψ_{rot}, of the elliptical noise cloud in the ϕ, χ plane, we rewrite Eqs. (2.8a-b) to obtain

$$< |\phi(\omega) \cos\Psi \ + \ \chi(\omega) \sin\Psi|^2 >$$
$$\propto \left[\omega^2 + C_0 + C_1 \cos 2(\Psi - \Psi_{\mathrm{rot}}) \right] , \qquad (2.16a)$$

$$\tan(2\Psi_{\mathrm{rot}}) \ = \ \frac{\omega_{\mathrm{lin}} - \alpha\gamma_{\|}}{\alpha\omega_{\mathrm{lin}} + \gamma_{\|} + (\alpha^2 + 1)\gamma_{\mathrm{non}}} \ \approx \ \frac{1}{\alpha} , \qquad (2.16b)$$

where C_0 and C_1 are constants, and where the approximation in Eq. (2.16b) is valid only in the limit of dominant linear birefringence ($\omega_{\mathrm{lin}} \gg \alpha\gamma_{\|}, \gamma_{\mathrm{non}}, \alpha\gamma_{\mathrm{non}}$). Note that the predicted rotation angle Ψ_{rot} is independent of frequency; a change of detection frequency will only affect the ellipticity of the polarization noise cloud on the Poincaré sphere, but not the angle Ψ_{rot} at which the noise reaches its maximum.

2.6 Polarization fluctuations for dominant linear birefringence; from 2D to 1D

The above analysis was based on a linearized description of the spin-eliminated model, *i.e.*, the relative strength of the various anisotropies could be anything, as long as the laser polarization remained approximately linear ($\phi, \chi \ll 1$). In practical VCSELs, the linear birefringence generally dominates over all other anisotropies, *i.e.*, $\omega_{\mathrm{lin}} \gg \gamma_{\mathrm{lin}}, \gamma_{\mathrm{non}}, \alpha\gamma_{\mathrm{non}}$, being still small enough to satisfy the adiabatic approximation, for which $\omega_{\mathrm{lin}} \ll \gamma_s/\alpha$ is needed [25] (typical numbers are: $\gamma_{\mathrm{lin}} < 3$ ns^{-1}, $\gamma_{\mathrm{non}} \approx 1$ ns^{-1}, $\alpha \approx 3$, $\omega_{\mathrm{lin}} \approx 60$ ns^{-1}, and $\gamma_s \approx 300$ ns^{-1} [25,24,36]). For this common case of dominant linear birefringence the spin-eliminated model can be further simplified, by a second adiabatic elimination, as demonstrated in this section.

We start by noting that, for the case of dominant linear birefringence, the polarization-resolved optical and intensity noise spectra become relatively simple, as the strength of the FWM peak and the nonuniformity of the polarization fluctuations are strongly reduced, being inversely proportional to ω_0^2 and ω_0, respectively [see Eqs. (2.10) and (2.14)]. One explanation for this behavior is that the relatively fast rotation on the Poincaré sphere, associated with the large linear birefringence, makes all trajectories look like "tightly-wound corkscrews"and

thereby smoothes out the difference between ϕ and χ dynamics. An equivalent explanation is that the large frequency difference, in the optical spectrum, between the nonlasing and lasing peak reduces the coupling between the two, making the orthogonal polarization mode look more and more like a standard nonlasing mode.

As a starting point for our full (non-linearized) description of the polarization dynamics we could use Eqs. (A.1a-b) in appendix A. Instead, it is more convenient to rewrite the spin-eliminated model in terms of the normalized Stokes vector, as [26]:

$$
\begin{aligned}
\frac{ds_1}{dt} &= \gamma_{\mathrm{lin}}\cos 2\beta(1-s_1^2) - \gamma_{\mathrm{lin}}\sin 2\beta s_1 s_2 \\
&\quad + 2\gamma_{\mathrm{non}}s_1 s_3^2 + 2\alpha\gamma_{\mathrm{non}}s_2 s_3 \,,
\end{aligned}
\tag{2.17a}
$$

$$
\begin{aligned}
\frac{ds_2}{dt} &= -\omega_{\mathrm{lin}}s_3 + \gamma_{\mathrm{lin}}\sin 2\beta(1-s_2^2) - \gamma_{\mathrm{lin}}\cos 2\beta s_1 s_2 \\
&\quad + 2\gamma_{\mathrm{non}}s_2 s_3^2 - 2\alpha\gamma_{\mathrm{non}}s_1 s_3 \,,
\end{aligned}
\tag{2.17b}
$$

$$
\begin{aligned}
\frac{ds_3}{dt} &= \omega_{\mathrm{lin}}s_2 - \gamma_{\mathrm{lin}}\cos 2\beta s_1 s_3 - \gamma_{\mathrm{lin}}\sin 2\beta s_2 s_3 \\
&\quad - 2\gamma_{\mathrm{non}}s_3(1-s_3^2) \,.
\end{aligned}
\tag{2.17c}
$$

For the case of dominant linear birefringence the prevailing evolution over the Poincaré sphere is a fast rotation around the s_1-axis, where s_2 and s_3 perform a rapid out-of-phase oscillation with approximate frequency ω_{lin}, driven by the first terms in Eqs. (2.17a-c). On top of this rapid oscillation of the s_2 and s_3 coordinates, there is a much slower evolution of the s_1 coordinate, that can be separated out via a new adiabatic elimination. On the Poincaré sphere, the slow variable measures the position of an almost circular orbit at almost constant $s_1 = \cos(2\varphi)$, where $\varphi = \phi$ only at $\chi = 0$. By averaging Eq. (2.17a) over the fast rotation just mentioned, we can set $<s_1 s_2> \approx 0$, $<s_2 s_3> \approx 0$ and $<s_1 s_3^2> \approx (1/2)s_1(1-s_1^2)$, to obtain

$$
\frac{ds_1}{dt} \approx \left(\gamma_{\parallel} + \gamma_{\mathrm{non}}s_1\right)\left(1 - s_1^2\right) \,.
\tag{2.18}
$$

As the combination $(1-s_1)/2$ is equal to the relative intensity of the y-polarized light, the above equation describes the deterministic evolution that underlies the polarization-mode partition noise.

To obtain the full polarization dynamics we will now add noise to the above equation (2.18). For the angle φ it is immediately clear how much noise should be added: as polarization noise is isotropic on the Poincaré sphere, the amount of noise f_φ, perpendicular to the fast orbital evolution, is equal to that in the other projections f_χ and f_ϕ [see Eq. (2.7a-b)]. The amount of noise in s_1 is then found

by a simple transformation. The addition of noise can also produce extra drift terms in the equations [37]. For instance, the polarization noise in s_2 and s_3 will produce a steady decrease of $s_1^2 = 1 - s_2^2 - s_3^2$. Keeping this into account we obtain the following stochastic equations:

$$\frac{ds_1}{dt} = \left(\gamma_\parallel + \gamma_{\text{non}} s_1\right)\left(1 - s_1^2\right) - 4D s_1 + \left(2\sqrt{1 - s_1^2}\right) f_\varphi , \qquad (2.19a)$$

$$\frac{d\varphi}{dt} = -\frac{\gamma_\parallel}{2} \sin(2\varphi) - \frac{\gamma_{\text{non}}}{4} \sin(4\varphi) + \frac{D}{\tan(2\varphi)} + f_\varphi . \qquad (2.19b)$$

These equations show how the dominant linear birefringence, or fast rotation on the Poincaré sphere, effectively redirects the nonlinear anisotropy, so that the original (nonlinear) competition between the two circularly-polarized states is converted into a competition between the linearly polarized states aligned along the axes of birefringence. Equation (2.19b) thus has the same form as Eq. (9) in [38], which was recently derived for the dynamics of the ellipticity angle χ of an isotropic class A laser with strong competition between its circularly-polarized fields.

By transforming the above equations (2.19a,b) into the corresponding Fokker-Planck equations we regain the standard Kramers problem of "diffusion in a potential well" [39], on which the dynamics of a class A laser is usually mapped [40,41]. The steady-state probability distributions and potentials of our system are:

$$P(s_1) \quad \propto \quad \exp\left[-\frac{V_{s_1}(s_1)}{D}\right] \propto \exp\left[\frac{\gamma_\parallel}{2D} s_1 - \frac{\gamma_{\text{non}}}{4D}(1 - s_1^2)\right] , \qquad (2.20a)$$

$$P(\varphi) \quad \propto \quad \exp\left[-\frac{V_\varphi(\varphi)}{D}\right]$$

$$\propto \quad \sin(2\varphi) \exp\left[\frac{\gamma_\parallel}{2D} \cos(2\varphi) + \frac{\gamma_{\text{non}}}{8D} \cos(4\varphi)\right] . \qquad (2.20b)$$

The above result can be used to calculate the power ratio of the nonlasing and lasing mode $P_{\text{nonlasing}}/P_{\text{lasing}}$, or, equivalently, the mean-square deviation from the steady-state polarization, or, equivalently, the size of the noise cloud on the Poincaré sphere [see Eq.(2.3)]. For dominant x-polarized emission one finds:

$$\frac{P_{\text{nonlasing}}}{P_{\text{lasing}}} = \frac{1}{2}(1 - <s_1>) = <\varphi^2> = \frac{D}{\gamma_\parallel + \gamma_{\text{non}}} = \frac{D}{\gamma_0} . \qquad (2.21)$$

For dominant y-polarization the expression is the same, apart from a minus sign in front of $\gamma_\parallel$. Note that integration of the projected polarization noise spectrum, Eqs. (2.11a-b), over (positive and negative) frequency, gives the same result, for

the case of dominant linear birefringence considered here. Equation (2.21) shows, in a very convenient way, how polarization fluctuations result from a balance between a stochastic force on the one hand and the restoring forces of the (absorptive) anisotropies on the other hand. More specifically, it shows how the relative power in the nonlasing polarization, or the size of the noise cloud on the Poincaré sphere, can be used to estimate the noise strength D, when the dichroism γ_0 is known.

2.7   Experimental setup

For the experiments described in Sections 2.8-2.10 we have used a batch of some 50 proton-implanted VCSELs, organized as 1D arrays. The lasers operate around 850 nm and comprise three 8 nm thick GaAs quantum wells in a 1λ-cavity, sandwiched between an upper and lower Bragg mirror of 19 and 29.5 layer pairs, respectively [16]. The threshold currents of all these VCSELs is around 5 mA, with higher-order modes appearing around 10 mA at an output power of about 2 mW. At low current the laser polarization was practically always close to vertical, *i.e.*, perpendicular to the array axis. The steady-state ellipticity χ_{ss} was typically $1°$ or less, with a few exceptions of $\chi_{ss} \approx 5 - 10°$ for lasers with small negative birefringence ω_0. The size of the batch allowed us to pick the most interesting VCSELs for further study, namely those with relatively small effective birefringence and those that exhibit a polarization switch. In the presentation of the figures we will concentrate on two specific VCSELs, which we have labeled VCSEL 1 and VCSEL 2. Unfortunately, the (current-dependent) VCSEL performance showed small variations from day to day, so that the exact numbers for birefringence and dichroism, as obtained for the same VCSEL from the various figures, do not always match.

The experimental setup is sketched in Fig. 2.3. To limit the external noise to the minimum, the VCSEL is enclosed in a temperature-stabilized box (stability ≈ 0.1 mK) and driven by a stable current source (stability ≈ 0.75 μA from DC to 1 MHz). The collimated laser light is first passed through a (rotateable) $\lambda/4$ plate, and subsequently through a combination of a (rotateable) $\lambda/2$ plate and optical isolator, which together effectively act as a rotateable polarizer. By setting the angles of the $\lambda/4$ and $\lambda/2$ plates we select the polarization state on which the laser light is projected. After projection the light can be analyzed in three different ways. A planar Fabry-Pérot interferometer, with adjustable free spectral range, allows for detailed measurements of the optical spectrum. A 6-GHz low-noise photo receiver (NewFocus 1534 and 1514), in combination with a 25 GHz RF-analyzer (Hewlett Packard HP0563E), allows for measurements of the (polarization-resolved) inten-
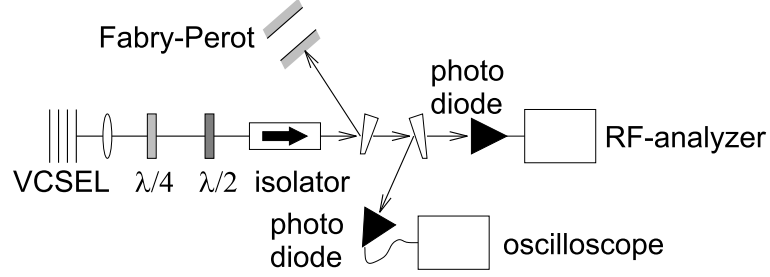
Figure 2.3: Experimental setup. After the polarization projection we measure: (i) optical spectra with a Fabry-Pérot interferometer, (ii) projected noise spectra with a 6-GHz photo diode and RF-analyzer, and (iii) time traces with a fast photo diode and oscilloscope.

sity noise. As a third method we can also observe this noise in the time domain, using a fast photo diode (DC-200 MHz) in combination with a 350 MHz oscilloscope (LeCroy 9450). In the next Sections we will discuss the results of these three methods in consecutive order.

2.8 Polarization-resolved optical spectra

Figure 2.4 shows optical spectra, for VCSEL 1 operating at $i = 9.0$ mA. In Fig. 2.4a the wave plates were set for projection onto the dominant (horizontal) polarization, whereas this polarization was largely blocked in Fig. 2.4b (we intentially kept a very small fraction of the lasing peak to serve as a marker). These figures show that the optical spectrum consists of three (equidistant) peaks, which (from left to right) are denoted the four-wave-mixing (FWM) peak (y_2), the lasing peak (x), and the nonlasing peak (y_1). Roughly speaking, the lasing peak is associated with the steady-state polarization of the laser, the nonlasing peak is a result of amplified spontaneous emission in the orthogonal polarization, and the four-wave mixing peak results from nonlinear mixing between these two. Comparison of the vertical scale of Figs. 2.4a and 2.4b shows that the lasing peak dominates over the nonlasing peak by roughly 3 orders of magnitude; it takes quite some suppression to resolve the latter. The FWM peak is much weaker still and often difficult to observe. In fact its presence was first reported in ref. [22].

The optical spectra of Figs. 2.4a,b contain information about many laser parameters. First of all the frequency difference between the lasing and nonlasing peak gives the effective birefringence ω_0, whereas the difference in their HWHM spectral width gives the effective dichroism γ_0. For VCSEL 1 studied in Fig. 2.4,
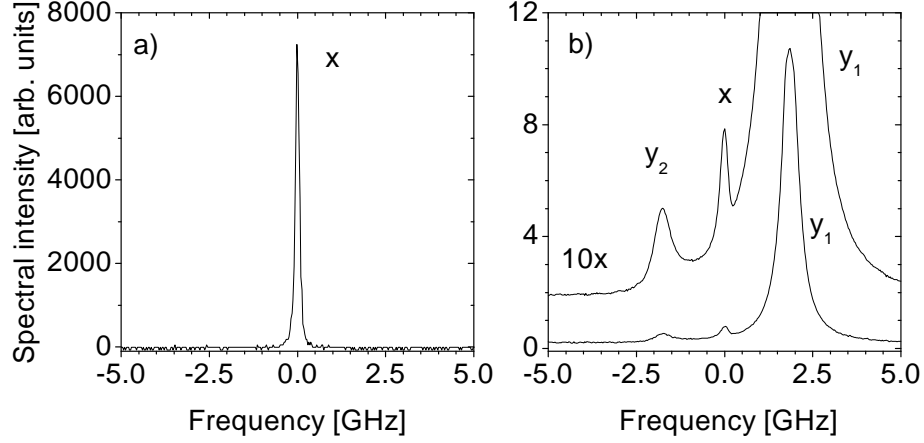
Figure 2.4: Polarization-resolved optical spectra of VCSEL 1 at $i = 9.0$ mA, as measured with a Fabry-Pérot. The x-polarized lasing peak, which dominates Fig. 2.4a, is almost completely suppressed in the y-polarized spectrum of Fig. 2.4b (same arbitrary units). The latter shows the nonlasing peak at higher frequency and a weak FWM peak, as mirror image, at lower frequency.

the effective birefringence is relatively small at $\nu_0 \equiv \omega_0/(2\pi) = -1.82(2)$ GHz (minus sign because the low-frequency mode lases); this is why it has been selected. Its effective dichroism has a more typical value, namely $\gamma_0/(2\pi) = 0.22(2)$ GHz. For most other VCSELs ν_0 ranged between -3 and +15 GHz (with two exceptions, at +25 and +40 GHz); the dichroism $\gamma_0/(2\pi)$ was always below 1 GHz. In Fig. 2.4 the measured spectral width of the lasing mode is instrument-limited to 0.06 GHz (HWHM) by the resolution of the Fabry-Pérot interferometer.

Equation (2.10) shows how the relative strength of the four-wave-mixing (FWM) peak, as compared to the nonlasing peak, can be used to quantify the non-linear anisotropies in the laser. From Fig. 2.4b we find this relative strength to be 2.5(2)%. With $\nu_0 = -1.82(2)$ GHz this gives a combined nonlinear anisotropy of $\sqrt{\alpha^2 + 1}\,\gamma_{\text{non}} = 3.6(2)$ ns^{-1}. Unfortunately, the optical spectrum does not allow a further separation into nonlinear birefringence and nonlinear dichroism; it mainly provides information on the nonlinear birefringence, as generally $\alpha \gg 1$ [42], so that $\sqrt{\alpha^2 + 1} \approx \alpha$.

Theoretically we expect the relative strength of the FWM peak (as compared to the nonlasing peak) to be inversely proportional to the square of the effective birefringence ω_0 [see Eq. (2.10)]. This is indeed observed: for two other VCSELs we measured a relative strength of 0.63(7)% at $\nu_0 = 3.45$ GHz, and 0.15(3)% at $\nu_0 = 6.7$ GHz. For our "average"VCSEL, with $\nu_0 \approx 10$ GHz, the strength of the

FWM peak was below 0.1 % of that of the nonlasing peak and thereby below the noise level.

As a last piece of information we calculate the amount of polarization fluctuations, by dividing the sum of the spectrally-integrated strengths of y-polarized nonlasing and FWM peak by the (integrated) x-polarized lasing peak. From Fig. 2.4 we determine this ratio to be 0.65(5)%. On the Poincaré sphere, this corresponds to a noise cloud with a size $< (2\varphi)^2 >^{\frac{1}{2}} \approx 9°$ [see Eq. (2.21)], which, on the world globe, is equivalent to an area bigger than Alaska, but smaller than Australia. At the end of section 2.9 we will discuss how the above value can be used to determine the magnitude of the polarization noise, and thereby the cavity loss rate κ.
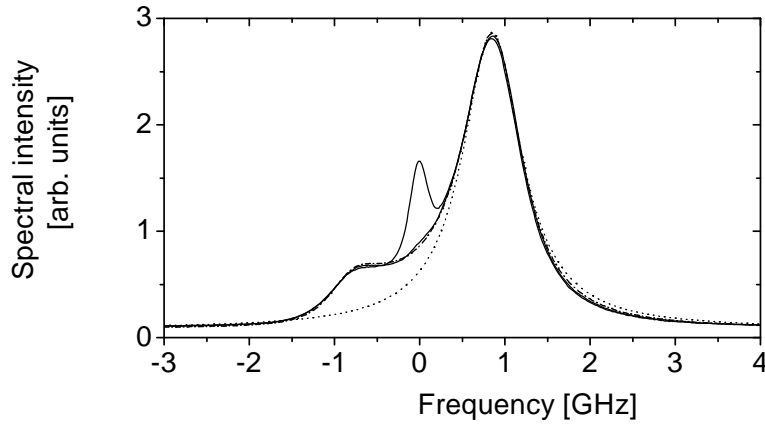

Figure 2.5: The optical spectrum of VCSEL 2 at $i = 10.0$ mA shows how, for VCSELs with very small birefringence ($\nu_0 = -0.85$ GHz in the present case) the FWM peak can be as much as 20% of the nonlasing peak. The dashed and dotted lines are fits to Eq. (2.9) and to a single Lorentzian, respectively.

For VCSEL 2, studied in Fig. 2.5, the birefringence is extremely small (and negative) at $\nu_0 = -0.85$ GHz in VCSEL. As a consequence, the strength of the FWM peak now amounts to about 20% of that of the nonlasing peak. For this extreme situation the nonlinear and linear anisotropies are comparable in strength and the nonlinear effect can no longer be treated as a weak perturbation. However, even for this extreme situation, the linearized theory developed in section 2.4 remains valid; the relative strength of the nonlasing and FWM peak, as compared to the lasing peak, is still only $\approx 1\%$, so that $\phi, \chi \ll 1$. This is demonstrated by the dash-dotted curve in Fig. 2.5, which is a fit of [Eq. (2.9)] to the optical spectrum, where the fitted width includes the finite width of the lasing peak. The dotted

curve shows the Lorentzian fit to the nonlasing peak only.

2.9   Polarization-resolved intensity noise spectra

In this section we will describe measurements of the polarization-resolved intensity noise, for which the principle was already discussed in section 2.5 (see Fig. 2.2). The practical implementation is based on a spectral analysis of the intensity noise of laser light that has passed through a rotateable $\lambda/4$ plate and a combination of a rotateable $\lambda/2$ and isolator, which together act as a rotateable polarizer (see Fig. 2.3). Figure 2.6 shows spectra of the projected intensity noise $< |I_{\mathrm{project}}(\omega)|^2 >^{\frac{1}{2}}$ for VCSEL 2 operating at $i = 9.0$ mA, with a relatively small birefringence of $\nu_0 = -0.85$ GHz. From top to bottom, the curves in Fig. 2.6 show noise spectra for projection onto the χ-direction, onto the ϕ-direction, onto the lasing polarization (label P), onto the nonlasing polarization, and the noise in the absence of light (system limit). As the noise in the first two projections is much larger than that for projection onto the lasing polarization, our first conclusion is that polarization noise dominates over pure intensity noise. Our analysis will be concentrated on the noise spectra observed for the χ and ϕ projections.
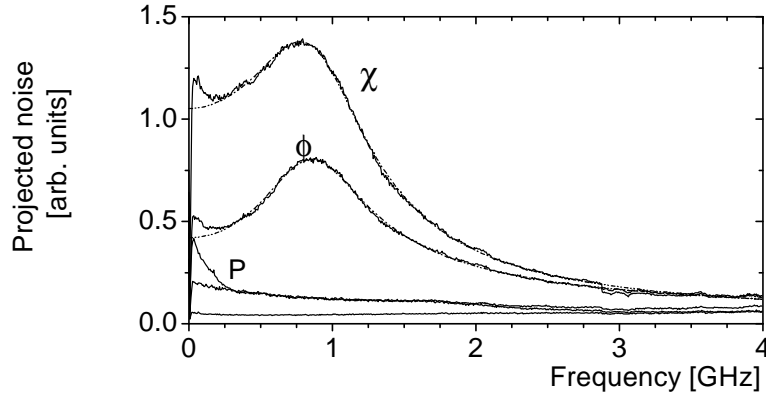

Figure 2.6: Projected intensity noise of VCSEL 2 at $i = 9.0$ mA. From top to bottom the curves show noise spectra for projection onto the χ-direction, onto the ϕ-direction, onto the lasing polarization (label P), onto the nonlasing polarization, and the noise in the absence of light (system limit).

The dashed curves in Fig. 2.6 are fits of Eqs. (2.11a-b) to the upper two experimental curves over the range 0.3-2.5 GHz. The fitting range has been limited to avoid both the low-frequency noise tail, as well as the high-frequency noise floor. The high quality of the fits allows us to extract: the effective birefringence

37

ω_0, the effective dichroism γ_0, a constant C [used to simplify the numerator of Eq. (2.11a) to $\omega^2 + C$, see also the discussion just above Eq. (2.15)], and a proportionality constant, which contains the detected intensity I, the diffusion rate D, and the system response. Our fitting results are: $|\nu_0| = |\omega_0/(2\pi)| = 0.85(2)$ GHz, $\gamma_0/(2\pi) = 0.38(2)$ GHz, $C_\phi/(4\pi^2) = 0.49$ GHz^2, and $C_\chi/(4\pi^2) = 3.6$ GHz^2. The first two parameters, ν_0 and γ_0, can also be obtained from optical spectra. A big advantage of the present measurement is its extreme resolution: a spectral analysis of intensity noise is only limited by the resolution of the RF-analyzer, which can easily be below 1 kHz, whereas optical measurements are limited by the Fabry-Pérot resolution of typically 10-100 MHz.

Figure 2.6 shows that the projected intensity noise in the χ-direction is much bigger than that in the ϕ-direction ($C_\chi > C_\phi$), or, in other words, that the polarization fluctuations are highly nonuniform and that the noise cloud on the Poincaré sphere is elliptical instead of circular. This difference is intimately related to the presence of the FWM peak in the optical spectrum, and can likewise be used to estimate the strength of the nonlinear anisotropies. To do so we determine the ratio $< |\phi(\omega)|^2 >^{\frac{1}{2}} / < |\chi(\omega)|^2 >^{\frac{1}{2}}$ and compare the result with Eqs. (2.13), (2.14) and (2.15). At the resonance frequency of 0.85 GHz we find $< |\phi(\omega)|^2 >^{\frac{1}{2}} / < |\chi(\omega)|^2 >^{\frac{1}{2}} = 0.59$. Substitution of this ratio in Eq. (2.14) yields $\alpha\gamma_{\text{non}} \approx 2.2$ ns^{-1}. As the very small birefringence makes the use of this approximate expression disputable, it is better to substitute the fitted C_ϕ and C_χ in Eq. (2.15), using the procedure discussed in section 2.5. This yields estimates of $\alpha\gamma_{\text{non}} \approx 2.0$ ns^{-1} on the first try and $\alpha\gamma_{\text{non}} \approx 2.5$ ns^{-1} upon iteration.

The noise spectra observed for the projections onto the lasing and nonlasing polarization contain information on the intensity and polarization partition noise. A detailed analysis of these spectra will be published elsewhere [43]. The relative strength of the various noise spectra show how the χ and ϕ projection are first-order in the polarization fluctuations and how the projections onto the lasing and nonlasing polarization are only second-order.

Figure 2.7 shows spectra of the projected intensity noise of VCSEL 1. This VCSEL exhibits a polarization switch; it operates on the high-frequency (vertically polarized) mode at $i = 8.5$ mA (Fig. 2.7a) and on the low-frequency (horizontally polarized) mode at $i = 9.0$ mA (Fig. 2.7b). In both figures the solid and dashed curves denote the intensity noise for projection onto the χ and ϕ-direction respectively, whereas the dash-dotted curve shows the system noise floor. The fits to these noise spectra (not shown) were again excellent and gave: $|\nu_0| = 2.96(2)$ GHz, $\gamma_0/(2\pi) = 0.23(2)$ GHz and $\alpha\gamma_{\text{non}} = 2.8(3)$ ns^{-1} at $i = 8.5$ mA, and $|\nu_0| = 1.75(2)$ GHz, $\gamma_0/(2\pi) = 0.23(2)$ GHz and $\alpha\gamma_{\text{non}} = 3.2(3)$ ns^{-1} at $i = 9.0$ mA. In Fig. 2.7 the differences between ϕ- and χ-noise are less prominent
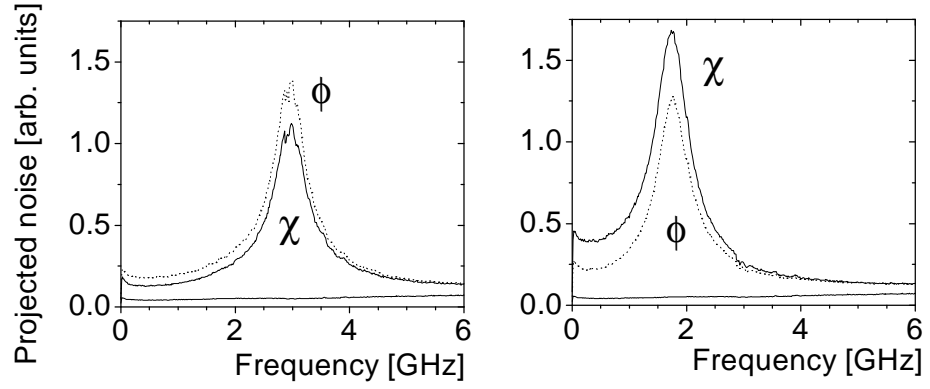
Figure 2.7: Projected intensity noise for VCSEL 1 before and after a polarization switch, at (a) $i = 8.5$ mA, and (b) $I = 9.0$ mA.

than in Fig. 2.6 as a result of the larger birefringence. The main message of this figure is that the nonuniformity of the polarization fluctuation is as expected for $\alpha \gg 1$; when the high-frequency mode lases we find $|\phi(\omega)| > |\chi(\omega)|$ (Fig. 2.7a); when the low-frequency mode lases we find $|\phi(\omega)| < |\chi(\omega)|$ (Figs. 2.6 and 2.7b).
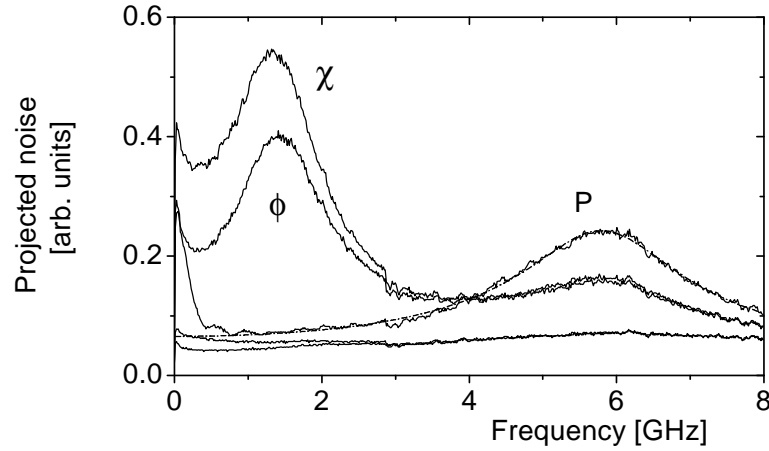

Figure 2.8: Projected intensity noise for VCSEL 2 at $i = 7.0$ mA. Note the presence of the relaxation oscillations around 6 GHz in the projection onto the lasing polarization (label P) and the corresponding structure in the polarization-resolved intensity noise (ϕ and χ). The dashed curve is a fit based on Eq. (2.12).

Figure 2.8 shows again the projected intensity noise spectra of VCSEL 2 (as in

Fig. 2.6), but now at an operating current of $i = 7.0$ mA, *i.e.*, closer to threshold ($i_{\text{thr}} = 5.0$ mA), and for a wider frequency range. The spectrum for projection onto the lasing polarization (solid curve, label P) is dominated by pure intensity noise; the broad structure around 6 GHz results from intensity fluctuations associated with the relaxation oscillations. The dash-dotted line shows a fit of Eq. (2.12) to this noise spectrum, yielding a relaxation oscillation frequency of 5.8 GHz and a damping (HWHM) of 1.1 GHz. The ϕ and χ-curves show the noise spectra for projection onto the corresponding polarization states. From fits in the range 0.4-2.8 GHz we find $|\nu_0| = 1.39$ GHz, $\gamma_0/(2\pi) = 0.55$ GHz, and $\alpha\gamma_{\text{non}} = 2.2$ ns^{-1}. This figure clearly shows how intensity noise and polarization noise simply add up in the projection spectrum; the relaxation oscillation is of course less prominent in the ϕ and χ-curves because the average intensity for polarization projection is about half the intensity for projection onto the lasing polarization.
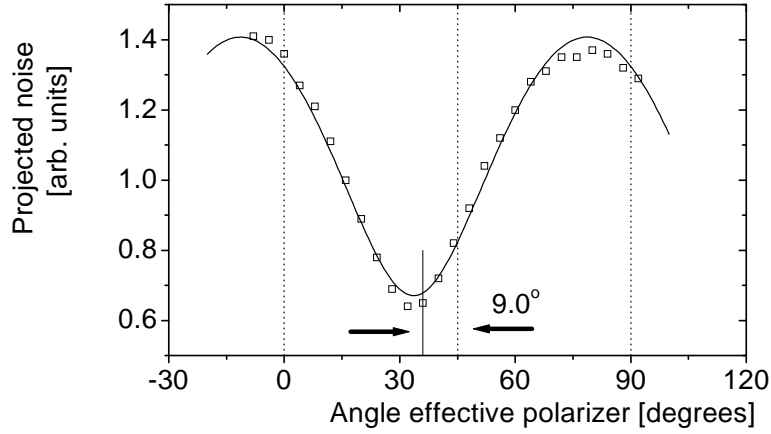

Figure 2.9: Measurements of the projected intensity noise for VCSEL 2 at $i = 9.0$ mA as function of the orientation angle of the projecting polarization. The angles 0° and 45° correspond to projection onto the χ and ϕ direction, respectively. Note the angular shift of about -9°.

Next we have measured the correlation between the polarization noise in ϕ and χ, which, according to section 2.5 and [26], should be noticeable as a rotation of the elliptical noise cloud on the Poincaré sphere. For best results we took VCSEL 2, with its relatively small birefringence and large nonuniformity, and operated it at 9.0 mA. Figure 2.9 shows a measurement series of the projected intensity noise as function of the angle of the projecting polarizer, where 0° and 45° corresponds to projection onto the χ- and ϕ direction respectively (see dashed vertical lines). The solid curve is a fit, using the square root of Eq. (2.16a). Figure 2.9 shows that

the cases of maximum and minimum projection noise do not correspond to pure χ- and ϕ projection, but occur at a slightly smaller angle. Specifically, the noise ellipse is rotated over an angle of $\Psi_{\mathrm{rot}} = 18(6)^\circ$ with respect to the χ, ϕ coordinate system. This agrees very roughly with the rotation angle as expected from Eq. (2.16a-b), which is about 9° for the case of dominant birefringence ($\alpha = 3$), but as much as 36° for the case at hand ($\omega_{\mathrm{lin}}/(2\pi) = -0.85$ GHz, $\gamma_{\mathrm{non}} \approx 1.0$ ns^{-1}, $\alpha \approx 3$, $\gamma_\parallel \approx 1.4$ ns^{-1}), where the latter estimate is clearly hindered by the uncertainties in the various parameters.

2.10   Polarization switches

For some VCSELs the polarization direction changes suddenly by about 90° when the laser current is varied. A study of the laser dynamics around such a polarization switch is ideally suited to determine the various laser parameters. This is demonstrated in Figs. 2.10a and 2.10b, which show the effective birefringence $|\nu_0|$ and dichroism $|\gamma_0|/(2\pi)$ of VCSEL 1, as obtained from the polarization-resolved intensity noise spectra, as a function of current. This VCSEL exhibits a polarization switch between 8.9 and 9.1 mA. To be more specific: at low current the (vertically polarized) high-frequency mode lases, at high current the (horizontally polarized) low-frequency mode lases, whereas either situation can occur within the switching region, depending on history (hysteresis). Fig. 2.10a shows how the frequency splitting between the lasing and nonlasing mode changes from $|\nu_0|$=3.16 GHz to 1.93 GHz, when the VCSEL switches polarization. This change is a result of nonlinear birefringence and can be used as a measure thereof [22]. By expanding Eq. (2.5a) into a linearized expression for the "spectral redshift of the nonlasing mode" we deduce from the switch that $\alpha\gamma_{\mathrm{non}} \approx \pi(3.16 - 1.93)$ ns$^{-1} =$ 3.9 ns^{-1}. Using the full Eq. (2.5a) we get a somewhat better estimate, $\alpha\gamma_{\mathrm{non}} \approx$ 3.7 ns^{-1}. We note that VCSEL 1 was also used to obtain the optical spectrum of Fig. 2.4 (at $i = 9.0$ mA and $\nu_0 < 0$, *i.e.*, after the switch), and the polarization-resolved intensity noise of Fig. 2.7 (before and after the switch).

Figure 2.10b shows how the effective dichroism changes with current and how the vertically-polarized mode becomes less and less dominant. This is a general trend in all our VCSELs: before the switch the dominant polarization is always close to vertical, *i.e.*, perpendicular to the array axis; after the switch the dominant polarization becomes horizontal. Furthermore, VCSELs that have a small dichroism at low current exhibit a polarization switch at increasing current, whereas those with larger dichroism do not switch within the realm of fundamental mode operation. We therefore attribute the occurrence of these switches to a current dependence of the measured effective dichroism $\gamma_0(i)$, and more specifically to
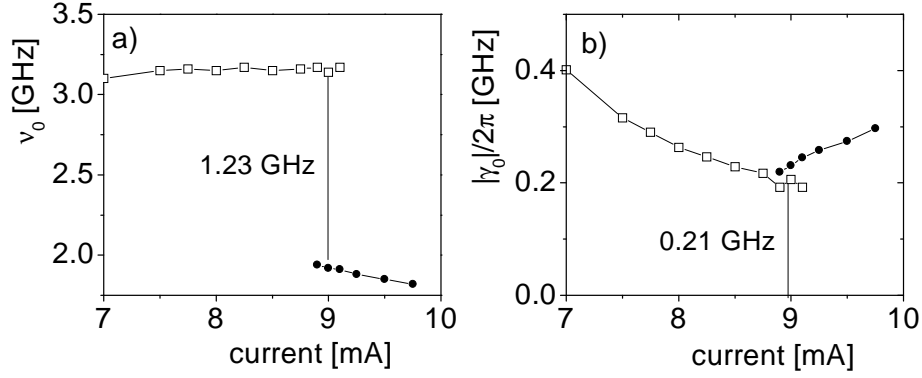
Figure 2.10: The effective birefringence $|\nu_0|$ and dichroism $|\gamma_0|$ of VCSEL 1 as function of current. Note the observed hysteresis and the jump in $|\nu_0|$ that occurs upon a polarization switch (around $i = 9.0$ mA). From Fig. 2.10b we conclude that the polarization switch results from a current dependence dichroism, $\gamma_0(i)$.

the linear part thereof, *i.e.*, $\gamma_{\parallel}(i)$, as the nonlinear part $\gamma_{\text{non}} > 0$ will always favor the lasing polarization over the nonlasing one and increase monotonically with current. A measurement of $\gamma_0(i)$ in fact allows us to predict whether or not a polarization switch is going to occur at a certain current. In the switching region the two polarizations will have almost equal loss ($\gamma_{\parallel} \approx 0$) so that we conclude for the nonlinear dichroism $\gamma_{\text{non}} \approx \gamma_0 \approx 2\pi \times 0.21$ ns^{-1} = 1.3 ns^{-1} (see Fig. 2.10b). Division of the nonlinear birefringence (in Fig. 2.10a) by the nonlinear dichroism (in Fig. 2.10b) yields $\alpha \approx 2.9$, in agreement with literature values. Similar values where found for other VCSELs. As an example, one of these other VC-SELs switched its polarization around $i = 8.5$ mA, had a frequency splitting of 11.5 GHz and 10.5 GHz before and after the switch and an effective dichroism of $\gamma_0/(2\pi) = 0.22$ GHz within the switching region, so that $\alpha \approx 3.1$.

In practice, the VCSELs that switch their polarization can have both positive and negative effective birefringence ν_0. In both cases, the observed changes in ν_0 were consistent with the expected nonlinear redshift [see Eq. (2.5b)]: when the high-frequency mode dominates ($\nu_0 > 0$) at low current, as is generally the case in our VCSELs, $|\nu_0|$ increased gradually with current and jumped to a smaller value upon a polarization switch; when the low-frequency mode is dominant ($\nu_0 < 0$), $|\nu_0|$ decreased with current, to jump to larger values upon a switch. Furthermore, switches have been observed in VCSELs with both small and large ν_0. These observations show that the nonlinear anisotropies by themselves are not the prime reason for the occurrence of polarization switches, as the "nonlinear" explanation predicts only switches from low to higher frequency operation, and only at rela-

tively small (negative) ν_0 [23,30].

The physical mechanism behind the polarization switches, *i.e.*, the mechanism responsible for the experimentally-observed current dependence of $\gamma_\parallel(i)$, is not yet known. It is tempting to attribute this dependence to a (temperature-induced) shift in frequency detuning between the polarized cavity modes and the gain spectrum [13]. However, this explanation seems to be ruled out by our experiments. Apart from subtleties in the scalar or tensor nature of γ_{lin}, this explanation predicts that the mode closest to the gain centre lases and that the current dependence of γ_0 is proportional to the effective birefringence ν_0. In practice, we find both switches from low-to-high and high-to-low frequencies, and we find hardly any correlation between the slope $d\gamma_0/di$ (in figures like Fig. 2.10b) and ν_0. An alternative explanation has not yet been found. The observation that the dominant polarization is always vertical before and horizontal after the switch indicates that the physical mechanism behind the polarization switch is linked to either the design layout of the array or to the orientation of the crystalline wafer.

The diffusion coefficient D can be estimated from the absolute strength of the polarization fluctuations, as given by the ratio of power in the dominant polarization and the orthogonal polarization, in combination with the effective dichroism γ_0 [see Eq. (2.21) for the case of dominant linear birefringence]. This power ratio can be obtained most reliably from optical spectra like Fig. 2.4, by integration over the lasing and nonlasing peak, but one can also use the frequency-integrated projection noise, as e.g. in Fig. 2.7, or even the polarization-resolved light-current characteristic of the laser (as long as the higher-order modes remain weak). We found these estimates to be mutually consistent within a factor 1.5; at a typical current of 8.5 mA they all yielded $P_{\text{nonlasing}}/P_{\text{lasing}} \approx 0.7 - 1.0\,\%$. Combined with $\gamma_0 \approx 1.1$ ns^{-1} this then corresponds to $D \approx 8 - 11 \mu\text{s}^{-1}$ at an output power of 1.8 mW.

As a final step we deduce the cavity loss rate κ from the value of D, using Eq. (2.7b). We therefore express the intra-cavity photon number S in terms of the VCSEL output power as $P_{\text{out}} = 2h\nu\eta\kappa S$, where η is the outcoupling efficiency through the top mirror. At $i = 8.5$ mA we had $D = 8 - 11\ \mu\text{s}^{-1}$ at an output power of 1.8 mW. For an ideal four-level laser, where $n_{\text{sp}} = \eta = 1$, this would make the estimated cavity loss rate $\kappa \approx 200$ ns^{-1}. A more realistic estimate, based on $n_{\text{sp}} = 1.5$ and $\eta = 0.3$, gives $\kappa \approx 300$ ns^{-1}.

2.11   Results for other VCSELs

In this section we address the question whether our results have generic validity. Therefore, we have repeated the experiments discussed in Secs. 2.8-2.10 on

several types of VCSELs from different manufactures. In the following subsections we will present the results obtained for etched-post VCSELs and for oxide-confined VCSELs, respectively. Finally, we end with an overall comparison of all the investigated structures.

2.11.1 Etched-post VCSELs

The set of etched-post VCSELs were grown at the "Centre Suisse Electronique and Microtechnique"(formerly the Paul Scherrer Institute, currently Avalon Photonics) in Zürich, Switzerland. These devices have a post diameter of 17 μm (*i.e.*, no proton implantation) and comprise three 8 nm thick GaAs quantum wells in a 1-λ cavity. The top and bottom Bragg mirror contain 20 and 40.5 pairs of graded AlAs-Al$_{0.18}$Ga$_{0.82}$As layers, respectively. The device that was singled out for further study had a threshold current of $i_{thr} = 4.1$ mA, operated in the fundamental transverse mode up to 2 i_{thr}, and exhibited a polarization switch around 5.5 mA, at an output power of 0.30 mW.
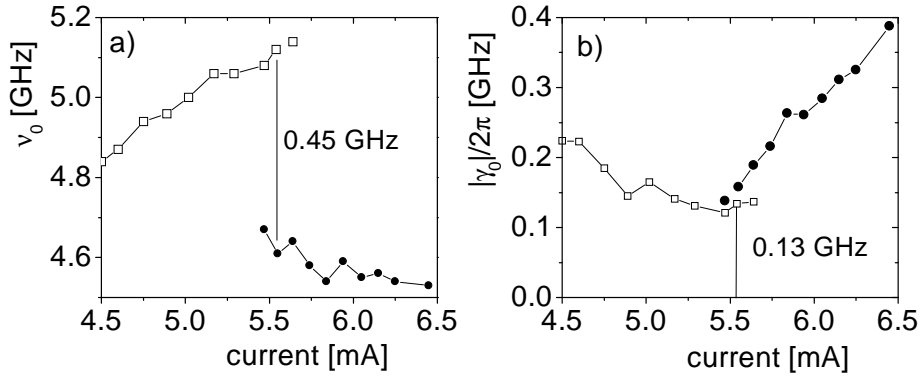

Figure 2.11: The effective birefringence $|\nu_0|$ and dichroism $|\gamma_0|$ of the etched-post VCSEL as function of current. Note the observed hysteresis and the jump in $|\nu_0|$ that occurs upon a polarization switch (around $i = 5.5$ mA). From Fig. 2.11b we conclude that the polarization switch results from a current dependent dichroism, $\gamma_0(i)$.

Figure 2.11 shows the effective birefringence $|\nu_0|$ and dichroism $|\gamma_0|/(2\pi)$ measured as function of laser current. The behavior of this etched-post VCSEL is quite similar to that of the proton-implanted VCSEL in Fig. 2.10. Once more, we observed hysteresis; when the current is increased the VCSEL polarization switches from y to x at $i = 5.65$ mA; when the current is decreased the VCSEL polarization lingers on in x and switches back at $i = 5.46$ mA. Again, the effec-

tive birefringence exhibits a jump due to the nonlinear birefringence (Fig. 2.11a) and again the switch coincides with a minimum in the measured dichroism as a function of current $\gamma_0(i)$ (see Fig. 2.11b). By relating the jump in Fig. 2.11a to the nonlinear redshift we find $\alpha\gamma_{\text{non}} \approx \pi(5.13 - 4.68)$ ns^{-1} = 1.4(1) ns^{-1}. By relating the effective dichroism inside the hysteresis loop to nonlinear effects we find $\gamma_{\text{non}} \approx 2\pi \times 0.132$ ns^{-1} = 0.83(6) ns^{-1}. Combining these two results yields $\alpha = 1.7(2)$, which is relatively low, but not unrealistic for thin quantum wells [42]. As a detail, we note that the effective dichroism inside the hysteresis loop is asymmetric, γ_0 being larger after the polarization switch than before. The reason for this asymmetry is not yet known.

As a next step we tried to observe the effect of the nonlinear anisotropies in the polarization-resolved optical and intensity noise spectra. To increase our changes of success, and to facilitate the comparison with earlier results, we set the laser current at $i = 5.55$ mA, *i.e.*, inside the hysteresis loop, after the polarization switch. At this point, both ν_0 and γ_0 are relatively small, so that both the magnitude of the nonlinear effects and the polarization fluctuations are optimized. In this situation the optical spectra showed the integrated power in the nonlasing peak to be 2.6% of that of the lasing peak. What is more important, these spectra also showed the presence of a four-wave mixing peak at an intensity of $8.0(6) \times 10^{-4}$ of that of the nonlasing peak. When we combine this ratio with $|\nu_0| = 4.68$ GHz in Eq. (2.10) we find $\sqrt{\alpha^2 + 1}\gamma_{\text{non}} = 1.7(1)$ ns^{-1}, in good agreement with the earlier estimate based on the observed nonlinear redshift.

We also measured the polarization-resolved intensity noise. The fits to these spectra were quite good, although they were somewhat hindered by the presence of a low-frequency relaxation-oscillation peak around 2.3 GHz. After the polarization switch the fluctuations in the polarization angle ϕ were measured to be smaller than in the ellipticity angle χ, as expected for a VCSEL in which the low-frequency mode dominates ($\nu_0 = -4.68$ GHz). At the resonance frequency we measure $< |\phi(\omega)|^2 >^{\frac{1}{2}} / < |\chi(\omega)|^2 >^{\frac{1}{2}} = 0.92(2)$. Substitution of this ratio in Eq. (2.14) yields $\alpha\gamma_{\text{non}} \approx 2.4(6)$ ns^{-1}. This estimate is somewhat larger than the previous ones, but still falls within the error bars, which are relatively large due to the presence of relaxation oscillations.

Finally we estimate the magnitude of the polarization noise from the observed power ratio $P_{\text{nonlasing}}/P_{\text{lasing}} = 2.6\%$. Substitution of this ratio, and the fitted value of $\gamma_0 = 0.83$ ns^{-1}, into Eq. (2.21) yields a diffusion coefficient $D = 22(3)$ μs^{-1}. Just as before, we now insert D, together with the output power of 0.3 mW, into Eq. (2.7b), to obtain an estimated cavity loss rate $\kappa \approx 120$ ns^{-1} for the ideal four-level laser and $\kappa \approx 220$ ns^{-1} for the case $n_{\text{sp}} = 1.5$ and $\eta = 0.2$.

2.11.2   Oxide-confined VCSELs

The oxide-confined VCSELs that we have investigated were grown by two different manufactures; from CSEM we studied structures grown with MOCVD and from the University of Ulm we studied structures grown with MBE.

The oxide-confined VCSELs grown at CSEM, emit at a wavelength of $\lambda \approx 960$ nm. The top and bottom Bragg mirror contain 21 and 30 pairs of alternating layers of $Al_{0.9}Ga_{0.1}As$ and GaAs. The cavity comprises three InGaAs quantum wells embedded in $Al_{0.15}Ga_{0.85}As$. The oxide-layer (AlAs) is 25 nm thick and is located in the first p-doped mirror period.

All the devices from this set exhibited a polarization switch. For the experiments we selected a typical device with an oxide diameter of 3.9 μm. The threshold current of this device was $i_{thr} = 0.3$ mA, and the device emitted into the fundamental transverse mode up to a current of 3.0 mA. The switch occurred around a laser current of $i = 0.6$ mA at an output power of 0.070 mW. Figure 2.12 shows the effective birefringence $|\nu_0|$ and dichroism as $|\gamma_0|/(2\pi)$ function of current. The effective birefringence was positive before the switch and negative afterwards.
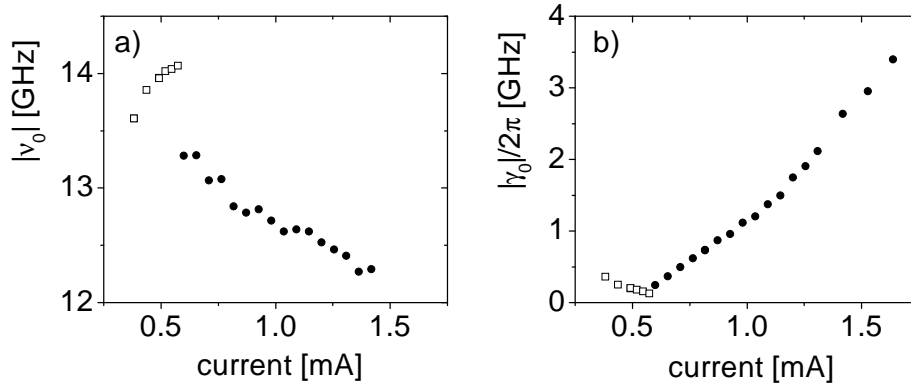

Figure 2.12: The effective birefringence $|\nu_0|$ and dichroism $|\gamma_0|$ of the oxide-confined VCSEL from CSEM as function of current. This laser exhibited a polarization switch at current of 0.6 mA. From 2.12b we conclude that the polarization switch results from a current dependent dichroism $\gamma_0(i)$.

Around the polarization switch at $i = 0.6$ mA, the anisotropies showed the same characteristics as was observed for the other structures: the effective birefringence jumps, and the measured dichroism exhibits a minimum. Attributing the jump in Fig. 2.12a to the nonlinear redshift gives a value of $\alpha\gamma_{non} \approx 2.5$ ns^{-1} for the nonlinear birefringence. Attributing the minimum dichroism at the switch in Fig. 2.12b to the nonlinear dichroism gives $\gamma_{non} \approx 1.0$ ns^{-1}. Division of the

nonlinear anisotropies yields $\alpha \approx 2.5$. However, most remarkable for these oxide-confined devices is the very large current dependence of the dichroism, as shown in Fig. 2.12b. At higher laser currents we measured values of $\gamma_0 \approx 3 - 4$ GHz for the dichroism; these values are an order of magnitude larger as measured for proton-implanted VCSELs and etched-post VCSELs.

Unfortunately, the other methods to quantify the nonlinear effects failed for this set of lasers. Due to the large effective birefringence ($|\nu_0|$=12-14 GHz), the four-wave-mixing effect becomes too weak for detection. Also the polarization-resolved intensity noise could not be measured, since the noise in ϕ and χ peaked at a birefringence beat frequency too high for detection with a photo diode.

From integration of the spectral peaks, we found that the power in the nonlasing mode was 4% of that in the lasing mode at a current of i=0.55 mA just below the switching current. Using Eq. 2.21 (see discussion at end of Sec. 2.10), this modal ratio yields a diffusion coefficient of $D = 40$ μs^{-1}. Plugging this value of D and $P_{\text{out}} = 0.070$ mW at $i = 0.6$ mA into Eq. 2.7b gives a value of $\kappa \approx 150$ ns^{-1} for the cavity loss rate, where we used a value of $\eta \approx 30\%$ for the quantum efficiency, as extracted from the output-input curve.

The oxide-confined VCSELs, grown at the University of Ulm, emit at a wavelength of $\lambda \approx$ 830 nm. None of these oxide-confined devices exhibited a polarization switch. From these devices a typical device was selected for further measurements. The threshold current of this laser was $i_{\text{thr}} = 0.43$ mA and the laser emitted into the fundamental transverse mode up to a current of 3.0 mA.

The effective birefringence $|\nu_0|$ and dichroism $|\gamma_0|/(2\pi)$ as a function of the laser current are shown in Fig. 2.13. The effective birefringence was found to be negative. The effective dichroism was found to be $\gamma_0 = 0.8 - 1.5$ GHz, again being much larger than typical values measured for proton-implanted and etched-post devices.

The absence of a polarization switch hindered a complete analysis of the nonlinear effects in this laser. Moreover the large value of the dichroism results in a very weak nonlasing mode. At a setting of 2.5 mA, the power ratio of the nonlasing mode and lasing mode was 1.2×10^{-3}. Despite the weakness of the nonlasing mode, we have been able to observe the four-wave-mixing peak in the optical spectrum. To optimize the nonlinear effects the measurements were done at a relative high laser current of $i = 2.5$ mA. The relative power in the four-wave-mixing peak compared to that in the nonlasing mode was 1.9(2)%, determined after substraction of the wing of the nonlasing mode. Combining this value for the relative strength in the four-wave-mixing peak with a measured value of $\nu_0 = -5.0$ GHz, gives a value of $\omega_{\text{non}} \approx 8.7$ ns^{-1} [see Eq. (2.10)]. As a next step, we measured the polarization-resolved intensity noise. At the resonance frequency, we found a ra-
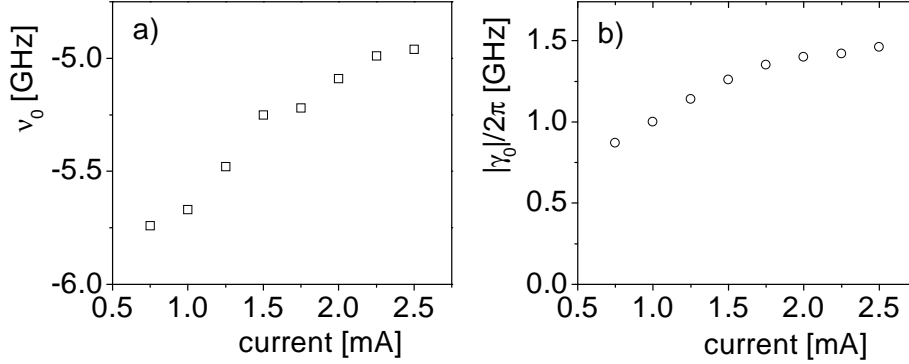
Figure 2.13: The effective birefringence $|\nu_0|$ and dichroism $|\gamma_0|$ of the oxide-confined VCSEL from the University of Ulm as function of current. This device didn't exhibit a polarization switch.

tio of $< |\phi(\omega)|^2 >^{\frac{1}{2}} / < |\chi(\omega)|^2 >^{\frac{1}{2}} = 0.72$ for the fluctuations in the polarization angle ϕ and ellipticity angle χ. Substitution of this ratio into Eq. (2.14), yields $\omega_{\text{non}} = 8.8$ ns^{-1}. This estimate of ω_{non} agrees with the previous value obtained from the relative power in the four-wave-mixing peak.

At a current of $i = 2.5$ mA, we measured a value of $\gamma_0/2\pi = 1.4$ GHz for the dichroism (see Fig. 2.13). From integration of spectral peaks, the power in the nonlasing mode was found to be 0.12 % of that in the lasing mode. Inserting these two values into Eq. (2.21), gives a diffusion coefficient $D = 11$ μs^{-1}. Finally, we obtained a value of $\kappa \approx 150$ ns^{-1} for the cavity loss rate from substitution of measured values of $D=11$ μs^{-1} at $P_{\text{out}} = 0.45$ mW and $i = 2.5$ mA, in combination with $\eta = 46$ % into Eq. (2.7b).

2.11.3 Comparison between different VCSELs

Comparing the etched-post VCSELs and oxide-confined VCSELs to the proton-implanted VCSELs we note that for all types of devices nonlinear effects were observable in three different ways, as: *(i)* a nonlinear redshift and extra dichroism, *(ii)* a FWM peak in the optical spectrum, and *(iii)* a different magnitude of the projected polarization noise. However, we remark that for oxide-confined VCSELs the nonlinear effects were quite difficult to observe, since for these structures the measured dichroism (and its current dependence) was found to be very large. The large dichroism resulted in power ratios between the lasing and non-lasing mode of 30 dB and larger, making oxide-confined VCSELs very attractive for applications where a high polarization stability is required, but very difficult to

Table 2.2: Overview of the measured parameters of the VCSEL structures, where λ is the approximate emission wavelength; i_{thr} the threshold current; i, and P_{out} the current and output power at which the nonlinear birefringence ω_{non}, the nonlinear dichroism γ_{non}, and the diffusion coefficient D were measured; κ the cavity loss rate of the optical field.

	proton-implanted	etched-post	oxide-confined	oxide-confined
λ [nm]	850	850	960	830
i_{thr} [mA]	5	4.3	0.30	0.43
i [mA]	8.5-9	5.5	0.6	2.5
P_{out} [mW]	1.5	0.3	0.07	0.45
ω_{non} [ns^{-1}]	3-4	1.5	2.5	8.8
γ_{non} [ns^{-1}]	1-1.3	0.8	1	
α	3	1.7	2.5	
D [μs^{-1}]	8-11	22	40	11
κ [ns^{-1}]	300	200	150	150

analyse polarization wise. The overall result of our analysis is shown in table 2.2 that summarizes all the measured parameters of the different VCSEL structures. Please, note that the nonlinear anisotropies ω_{non} and γ_{non}, and the diffusion rate D of the structures have been determined at different currents and output powers, which are also mentioned in table 2.2. Comparison of the observed nonlinear anisotropies, relative to the degree of saturation ($\mu = i/i_{\text{thr}} - 1$), shows that the nonlinear effects are comparable for the different structures.

However, one should take into account that the cavity loss rate κ of the etched-post and oxide-confined devices, compared to the values of the proton-implanted devices, are relatively low, so that a given output power corresponds to a relatively high internal field. Experimentally, this difference loss rate was also noticeable in the diffusion coefficient D. The diffusion coefficient of $D \approx 22(3)$ μs^{-1} for the etched-post device is only a factor of 2-3 larger than that of the proton-implanted device, despite the factor of 5 lower output power. Similarly, the diffusion coefficient of oxide-confined VCSEL, emitting at 960 nm, is a factor 4 larger compared to that of the proton-implanted device, for a output power of a factor 20 lower. The diffusion coefficient of the oxide-confined VCSEL, emitting at 830 nm, is almost equal to that of the proton-implanted device, but again the output power is a factor 3-4 lower.

2.12   Summary and conclusions

We have presented a general description of polarization fluctuations in VCSELs, allowing direct comparison with experiment. An overview of the model parameters is given in table 2.1. In total the model involves four anisotropies. The physical mechanism behind these anisotropies is not yet fully understood; we know how the linear birefringence arises from mechanical strain [44] and internal electrical fields [45], and how the nonlinear anisotropies result from the (eliminated) spin dynamics [25,26], but the origin, and in particular the experimental observation of a current dependence, of the linear dichroism $\gamma_{\text{lin}}(i)$ is still somewhat of a mystery.

In the experimental sections we have shown how the various parameters can be extracted from the experimental data. More specifically, the effective birefringence and effective dichroism appear as frequency splittings and widths in both optical spectra and projected-intensity noise spectra. We gave three experimental demonstrations of the presence of nonlinear anisotropies. We have shown how they give rise to a four-wave mixing peak in the optical spectrum and to a nonuniformity in the projected polarization noise. Experimentally, both phenomena can be used to quantify the combined nonlinear anisotropies, but both are inversely proportional to (the square of) the linear birefringence so that the effects are measurable only for small to moderate birefringence. As a third demonstration of nonlinear effects we have shown how they give rise to a spectral redshift and excess width of the nonlasing peak as compared to the lasing peak. Experimentally, these measurements are ideal to separately determine the nonlinear birefringence and the nonlinear dichroism, but they only work for VCSELs that exhibit a polarization switch. Moreover, we have shown how in extreme cases, where the linear and nonlinear anisotropies are comparable, the concept of two polarization modes loses its meaning.

For a batch of proton-implanted VCSELs we have applied the three techniques mentioned above to obtain results that agreed within about 20%. We have also demonstrated to what extent the fluctuations in polarization direction ϕ and ellipticity χ are correlated. In general, we have shown how polarization fluctuations result from a balance between diffusion, due to polarization noise, and a restoring drift, due to dichroism. The diffusion coefficient D, and the related cavity loss rate κ could thus be estimated from the relatively power in the nonlasing polarization.

Repeating the measurements on batches of etched-post VCSELs and oxide-confined VCSELs from different suppliers gave similar results (see table 2.2 in Sec. 2.11). Once more the three different measurements were in reasonable agreement. This shows that both the phenomena and the quoted numbers are rather

general and not limited to a special type of VCSEL. As a remarkable distinction among the different structures, we mention the (current dependent) linear dichroism of the oxide-confined devices, which was observed to be up to an order of magnitude larger compared to that of the proton-implanted and etched-post devices. Oxide-confined VCSELs will therefore typically exhibit much less polarization fluctuations and have a much larger polarization mode suppression than other type of VCSELs.

In conclusion, this work presents an experimental confirmation of the validity of the spin-eliminated model for the polarization behavior of a VCSEL. We have stressed that almost any practical VCSEL satisfies the condition for spin elimination. Also, most practical VCSELs satisfy additionally the condition of relatively strong linear birefringence which, in turn, greatly simplifies the analytic description.

Appendix A

Linearization of polarization dynamics

In this appendix we will derive the steady-state polarization and linearized polarization rate equations for a laser where the linear birefringence and linear dichroism make an arbitrary angle β. For this case, the full rate equations, as found in [25,29,32], are:

$$
2\cos 2\chi \frac{d\phi}{dt} = -\omega_{\text{lin}}\sin 2\chi \cos 2\phi - \gamma_{\text{lin}}\sin 2(\phi-\beta)
$$
$$
-2\alpha\gamma_{\text{non}}\sin 2\chi \cos 2\chi \; , \tag{A.1a}
$$
$$
2\frac{d\chi}{dt} = \omega_{\text{lin}}\sin 2\phi - \gamma_{\text{lin}}\sin 2\chi \cos 2(\phi-\beta)
$$
$$
-2\gamma_{\text{non}}\sin 2\chi \cos 2\chi \; . \tag{A.1b}
$$

These equations are exact in the adiabatic limit, *i.e.*, no assumptions have been made apart from the adiabatic elimination of the difference inversion. To remove the various sine and cosine functions we expand to first order in $\phi, \chi \ll 1$, assuming the intensity I, which codetermines $\gamma_{\text{non}} = \kappa I/\Gamma$, to be more or less constant (valid for operation reasonably far above threshold). The steady-state angles thus found are:

$$
\chi_{\text{ss}} \approx \frac{\gamma_{\text{lin}}\sin 2\beta}{2(\omega_{\text{lin}}+2\alpha\gamma_{\text{non}})} \ll 1 \; , \tag{A.2a}
$$
$$
\phi_{\text{ss}} \approx \Big(\frac{\gamma_{\text{lin}}\cos 2\beta + 2\gamma_{\text{non}}}{\omega_{\text{lin}}}\Big)\chi_{\text{ss}} \ll 1 \; . \tag{A.2b}
$$

Equation (A.2a) is an extension to the nonlinear regime, of Eq. (18) in [24] that was derived from a linear coupled-mode theory. Note that this equation is asymmetric in (the sign of) ω_{lin}; large ellipticity are most likely for negative ω_{lin}, *i.e.*, for the case where the low-frequency mode lases. For the case of dominant linear birefringence ($\omega_{\text{lin}} \gg \gamma_{\text{lin}}, \gamma_{\text{non}}$) we also find $\phi_{\text{ss}} \ll \chi_{\text{ss}}$ [see Eq. (A.2b)].

For $\chi_{\text{ss}}, \phi_{\text{ss}} \ll 1$ the linearized polarization rate equations, including noise, are

$$
\frac{d}{dt}\begin{pmatrix} \phi-\phi_{\text{ss}} \\ \chi-\chi_{\text{ss}} \end{pmatrix} = \begin{pmatrix} -\gamma_{\|} & -\omega_{\text{lin}}-2\alpha\gamma_{\text{non}} \\ \omega_{\text{lin}} & -\gamma_{\|}-2\gamma_{\text{non}} \end{pmatrix}\begin{pmatrix} \phi-\phi_{\text{ss}} \\ \chi-\chi_{\text{ss}} \end{pmatrix} + \begin{pmatrix} f_\phi \\ f_\chi \end{pmatrix} \; , \tag{A.3}
$$

where $\gamma_\parallel \equiv \gamma_{\mathrm{lin}} \cos 2\beta$, and where we have added the Langevin noise sources f_ϕ and f_χ. We want to stress that, as these equations result from a linearization in the adiabatic approximation, they apply to all cases where $\phi, \chi, \chi_{\mathrm{ss}} \ll 1$, including the very interesting cases where linear and nonlinear anisotropies are comparable in strength. Note that Eq. (A.3) becomes identical to Eq. (6) in [26] and Eq. (1) in [22] for the case of aligned linear birefringence and dichroism.

Chapter 3

Correlated fluctuations in the polarization modes of a vertical-cavity semiconductor laser [1]

The correlated intensity fluctuations in the two polarization modes (x and y) of a TEM$_{00}$ vertical-cavity semiconductor laser are studied experimentally and theoretically. We show that the dynamics of laser polarization and total output power are almost completely decoupled and demonstrate how the frequency dependence of the correlation function C$_{xy}$ is related to dichroism and relaxation oscillations.

3.1   Introduction

The vertical-cavity surface-emitting laser (VCSEL) is a novel type of semiconductor laser with an almost circular geometry and a very short cavity. Benefits of this construction are, for example, that the output beam is circular and that lasing occurs in a single longitudinal mode. On the other hand, the almost perfect circular symmetry results in limited polarization stability and may even lead to polarization switching [13,46,30]. This instable behaviour is promoted by the quantum noise which is relatively strong in a VCSEL, due to its small modal volume. It is well known that the light emitted by VCSELs is approximately linearly polarized. More detailed studies have shown that the output light consists of a strong lasing mode and a weak nonlasing mode, which is orthogonally linear polarized with respect to the lasing mode [24]. The relative strength of this nonlasing mode quantifies the polarization fluctuations in the VCSEL.

A proper understanding of polarization fluctuations in VCSELs is important for practical applications and also for more fundamental topics, like the generation of intensity-squeezed light. In applications, polarization sensitive elements may lead to detection of mode-partition noise resulting in a degradation of the signal-to-noise ratio. For the generation of squeezed light, it is important to know how

large the effect of the polarization fluctuations on the total intensity noise is, and whether polarization fluctuations can deteriorate squeezing.

The aim of this paper is to study, experimentally as well as theoretically, the intensity fluctuations of the two polarization modes of a single-transverse-mode TEM_{00} VCSEL and the correlation between these fluctuations. So far, in most studies of the correlation of a two-polarization-mode laser the amount of acquired insight was limited [47–49], since the theoretical description was rather complicated and performed numerically. In this chapter, we present a direct comparison of experimental data obtained on a VCSEL oscillating in the TEM_{00} fundamental mode with an analytic theory. In Section 3.2, we introduce this theory which describes the dynamics of the two polarization modes and the inversion in a VCSEL. In particular, we focus on the validity of this theory for practical VCSELs. In Section 3.3 and 3.4 expressions for the intensity noise spectra and for the polarization correlation function are derived, respectively. In Section 3.5 we present the experimental data; in the successive subsections we discuss the measured intensity and polarization-resolved noise spectra. From these noise spectra we derive the correlation function and demonstrate its frequency dependence. Section 3.6 gives a concluding discussion.

3.2 Two-mode theory for VCSELs

An appropriate theoretical framework for the intensity fluctuations of polarization modes and their correlation is formed by a set of Langevin rate equations for the two polarization modes and the inversion, *i.e.*, we use a two-mode theory for a class-B laser. The advantage of such a two-mode theory is that it is a transparent starting point, formulated in terms of quantities that can be measured experimentally.

The standard theory to describe the polarization dynamics of quantum-well VCSELs is the spin-flip model developed by San Miguel, Feng and Moloney [15]. However, in its full generality this spin-flip theory allows only numerical solutions, permitting limited physical insight into the polarization dynamics. In this Section we describe, by refining our earlier work [50], how one can obtain a simple two-mode description from the spin-flip theory.

The spin-flip theory [15] incorporates the vectorial nature of the optical polarization and models the conduction and heavy-hole valence band by four discrete spin levels, which interact as two pairs with the circular components of the optical field. Effectively this model has two inversion reservoirs corresponding to the average inversion and the spin-difference inversion.

The first approximation that we will apply is the adiabatic elimination of the

spin-difference inversion [50,26,25]. This is allowed when both spin reservoirs are strongly coupled by spin scattering, which corresponds to a large value of Γ, being defined as the ratio of the decay rates of the spin-difference and average inversion. Experimental verification of this assumption has been demonstrated [50,22], yielding a relatively large value of $\Gamma \simeq 100 - 800$. After adiabatic elimination one obtains the following set of equations for the optical fields E_x and E_y and total inversion N,

$$
\frac{dE_x}{dt} = \frac{1}{2}(i\omega_{\text{lin}} + \gamma_\|)E_x + \kappa(1 - i\alpha)(N - 1)E_x
$$
$$
- \frac{\kappa}{\Gamma}(1 - i\alpha)[|E_y|^2 E_x + E_y^2 E_x^*] + F_{Ex}(t) , \tag{3.1a}
$$

$$
\frac{dE_y}{dt} = -\frac{1}{2}(i\omega_{\text{lin}} + \gamma_\|)E_y + \kappa(1 - i\alpha)(N - 1)E_y
$$
$$
- \frac{\kappa}{\Gamma}(1 - i\alpha)[|E_x|^2 E_y + E_x^2 E_y^*] + F_{Ey}(t) , \tag{3.1b}
$$

$$
\frac{dN}{dt} = -\gamma(N - 1 - \mu) - \gamma(|E_x|^2 + |E_y|^2)N
$$
$$
+ \frac{\gamma}{\Gamma}[2|E_x|^2|E_y|^2 - E_x^2(E_y^*)^2 - (E_x^*)^2 E_y^2] + F_N(t) , \tag{3.1c}
$$

where 2κ is the intensity cavity-loss rate, ω_{lin} is the linear birefringence, $\gamma_\|$ is the linear dichroism as projected onto the birefringence axes, α is the amplitude-phase coupling factor [21], N is the total inversion (normalized with respect to lasing threshold), γ is the spontaneous inversion decay rate and μ is the normalized pump parameter (at the lasing threshold $\mu = 0$).

In Eqs. (3.1a) and (3.1b) the one-but-last terms (proportional to $1/\Gamma$) are remnants of the fast spin-dynamics. The terms proportional to $|E_x|^2 E_y$ and $|E_y|^2 E_x$ correspond to the polarization dependence of the optical saturation (or nonlinear dichroism) and nonlinear birefringence. The terms with the complex conjugates correspond to a four-wave-mixing (FWM) effect, which is only observable in VCSELs with small linear birefringence, where it shows up as a weak FWM peak in the optical spectrum [22].

The second approximation needed to obtain a two-mode theory involves a simplification in describing the optical field. In the general vectorial description of a polarized light field, one needs four variables, which we have chosen in our earlier work [50] as total intensity, optical phase, polarization angle ϕ and ellipticity angle χ. In contrast, a two-mode theory requires only two variables, which can be chosen as the intensities of the two polarization modes x and y, or as the total intensity and the polarization angle.

57

The optical phase can always be eliminated, since it is not coupled to other variables due to time translation invariance. Although the steady-state polarization of a VCSEL is approximately linear, elimination of the ellipticity is not trivial. Difficulties arise in particular when polarization fluctuations become nonuniform in ϕ and χ, which is the case when nonlinear anisotropies are as strong or stronger than the linear anisotropies. Luckily, for almost every practical VCSEL linear birefringence is the dominant anisotropy, which results in equal polarization fluctuations in ϕ and χ. In this case one optical degree of freedom can be eliminated by "rotational averaging" of the fluctuations [50]. The polarization can now be described with only one variable, being the polarization angle, remembering that the steady-state polarization is linear and that the fluctuations in the ellipticity can be directly derived from the fluctuations in the polarization angle. Of course one must check for practical cases whether the linear birefringence is indeed dominant. After the rotational averaging one obtains the following set of Langevin equations for the intensities I_x and I_y of the x- and y-polarized TEM$_{00}$ modes and the inversion N,

$$\frac{dI_x}{dt} = 2\kappa(N-1)I_x + \gamma_\parallel I_x - 2\frac{\kappa}{\Gamma}I_xI_y + R_{sp}\beta + F_x(t) \, , \qquad (3.2a)$$

$$\frac{dI_y}{dt} = 2\kappa(N-1)I_y - \gamma_\parallel I_y - 2\frac{\kappa}{\Gamma}I_xI_y + R_{sp}\beta + F_y(t) \, , \qquad (3.2b)$$

$$\frac{dN}{dt} = -\gamma(N-1-\mu) - \gamma(I_x+I_y)N + 2\frac{\gamma}{\Gamma}I_xI_y + F_N(t) \, , \qquad (3.2c)$$

where F_x, F_y and F_N are Langevin noise sources. Note that I_x and I_y are normalized with respect to the saturation intensity, so that $I = \beta n$ with n the number of photons in the laser cavity and β the spontaneous emission factor; finally, $R_{sp} = 2\kappa n_{sp}$, where $n_{sp} \geq 1$ quantifies the degree of inversion. Note that the rotational averaging corresponds to eliminating the FWM terms in Eqs. (3.1a-c), *i.e.*, the assumption of dominant linear birefringence reduces the number of polarization degrees of freedom from 2 to 1 and also removes the FWM effect [22,50].

3.3 Mode-partition noise

In this Section we will derive expressions for the noise spectra of the total intensity and for the intensities in both polarization modes. In order to obtain these expressions, we linearize the Langevin equations [Eqs. (3.2a-c)] around the steady-state values $\overline{I}_x$, $\overline{I}_y$ and $\overline{N} \approx 1$. This results in the following set of Langevin difference

equations for the fluctuations ΔI_x, ΔI_y and ΔN

$$\frac{d}{dt}\begin{pmatrix} \Delta I_x \\ \Delta I_y \\ \Delta N \end{pmatrix} = \begin{pmatrix} F_x \\ F_y \\ F_N \end{pmatrix} + \tag{3.3a}$$

$$\begin{pmatrix} 0 & -\frac{2\kappa}{\Gamma}\bar{I}_x & 2\kappa\bar{I}_x \\ -\frac{2\kappa}{\Gamma}\bar{I}_y & -2\gamma_\parallel - 2\frac{\kappa}{\Gamma}(\bar{I}_x - \bar{I}_y) & 2\kappa\bar{I}_y \\ -\gamma + 2\frac{\gamma}{\Gamma}\bar{I}_y & -\gamma + 2\frac{\gamma}{\Gamma}\bar{I}_x & -\gamma(1 + \bar{I}_x + \bar{I}_y) \end{pmatrix} \cdot \begin{pmatrix} \Delta I_x \\ \Delta I_y \\ \Delta N \end{pmatrix},$$

where the (small) loss in the dominant x-mode was set to zero.

Next we solve these Langevin difference equations in the Fourier domain. As exact solution of the equations gives rather tedious expressions, we make two approximations: (i) the average intensity of the nonlasing mode $(\bar{I}_y)$ is assumed to be much smaller than that of lasing mode $(\bar{I}_x)$; this assumption is valid for practical VCSELs (typically, we find $R \equiv \bar{I}_y/\bar{I}_x < 0.02$, as we will see below). Therefore, we will neglect terms proportional to $\bar{I}_y$ in Eq. (3.3a). (ii) The contributions due to carrier noise are neglected, so that the Langevin noise sources are given by

$$\langle F_i(t) \rangle = 0 \tag{3.4}$$

$$\begin{aligned} \langle F_x(t)F_x(t+\tau) \rangle &= 2R_{\text{sp}}\beta\bar{I}_x\delta(\tau), \\ \langle F_y(t)F_y(t+\tau) \rangle &= 2R_{\text{sp}}\beta\bar{I}_y\delta(\tau), \\ \langle F_x(t)F_y(t+\tau) \rangle &= 0, \\ \langle F_N(t)F_N(t+\tau) \rangle &= \langle F_N(t)F_x(t+\tau) \rangle = \langle F_N(t)F_y(t+\tau) \rangle = 0. \end{aligned} \tag{3.5}$$

With these approximations, we find the following expressions for the noise spectra of the total intensity and the modal intensities:

$$\langle |I(\omega)|^2 \rangle = 2R_{sp}\beta\bar{I}_x\frac{\omega^2 + 4\gamma_{\text{ro}}^2}{(\omega^2 - \omega_{\text{ro}}^2)^2 + 4\gamma_{\text{ro}}^2\omega^2}, \tag{3.6a}$$

$$\begin{aligned} \langle |I_x(\omega)|^2 \rangle &= 2R_{sp}\beta\bar{I}_x\frac{\omega^2 + 4\gamma_{\text{ro}}^2}{(\omega^2 - \omega_{\text{ro}}^2)^2 + 4\gamma_{\text{ro}}^2\omega^2} \\ &+ 2R_{sp}\beta\bar{I}_y\frac{\omega_{\text{ro}}^4}{((\omega^2 - \omega_{\text{ro}}^2)^2 + 4\gamma_{\text{ro}}^2\omega^2)(\omega^2 + 4\gamma_0^2)}, \end{aligned} \tag{3.6b}$$

$$\langle |I_y(\omega)|^2 \rangle = 2R_{sp}\beta\bar{I}_y\left(\frac{1}{\omega^2 + 4\gamma_0^2}\right), \tag{3.6c}$$

where $I = I_x + I_y$ is the total intensity, $\omega_{\text{ro}} = (2\kappa\gamma\bar{I})^{1/2}$ the relaxation oscillation frequency, $\gamma_{\text{ro}} = \gamma(1 + \bar{I})/2$ the relaxation oscillation damping rate and γ_0

59

the dichroism, *i.e.*, the damping of the polarization fluctuations. The dichroism $\gamma_0 = \gamma_{\parallel} + \gamma_{\mathrm{non}}$ consists of two parts [50]; a contribution due to the gain difference between the polarization modes, or projected linear dichroism ($\gamma_{\parallel}$), and a contribution due to cross saturation of the two polarization modes ($\gamma_{\mathrm{non}} = 2\kappa\mu/\Gamma$), resulting from the adiabatic elimination of the difference inversion [25,26].

The shape of the total intensity noise spectrum [Eq. (3.6a)] is determined by the relaxation oscillations [51]. Typical numbers for the relaxation oscillation frequency and damping, found for VCSELs operating well above threshold, are in the range $\omega_{\mathrm{ro}}/2\pi = 2$-10 GHz and $\gamma_{\mathrm{ro}}/2\pi = 0.3$-2 GHz respectively (see also Section 3.5.3). The intensity noise spectrum of the nonlasing mode *y* [Eq. (3.6c)] is due to mode-partition noise; it has a Lorentzian shape, centered at zero frequency and a width of $2\gamma_0$. The mode-partition noise is concentrated at relatively low frequencies, because the dichroism in VCSELs is typically $\gamma_0/2\pi = 0$-1 GHz [50,43].

The noise in the lasing mode *x* [Eq. (3.6b)] depends both on the relaxation oscillations and the mode partition fluctuations. The first term in Eq. (3.6b) is the same as the noise spectrum of the total intensity noise, and dominates at higher frequencies, being resonant around the relaxation oscillation frequency. The second term is important only at low frequencies, where it enhances the noise in the lasing mode as compared to the total intensity noise. For the typical values given above, the second term in Eq. (3.6b), dominates at lower frequencies, where it reduces to the mode-partition noise [Eq. (3.6c)].

At this stage, it is important to note that our approximations, *(i)* and *(ii)* in this Section, have resulted in a relatively simple *decoupled* description of the polarization fluctuations. With the word decoupled we mean that the fluctuations in the total output power are independent of the cavity anisotropies (dichroism and birefringence), which affect the polarization. The dichroism appears only in the noise spectra of the individual polarization modes. Linear birefringence was assumed to be sufficiently large, in order to perform the "rotational averaging" of the polarization fluctuations. A quantitative estimate of the remaining small effects of the polarization dynamics on the total intensity, in particular on intensity squeezing, will be given in ref. [52], where the present results are taken as a starting point.

Previously, we have derived an expression for the average modal ratio $R = \overline{I}_y/\overline{I}_x$, as $R = D/\gamma_0$ (see Sec. 2.6 and ref. [50]). More spontaneous emission noise (D) makes the nonlasing mode (y) stronger, whereas more dichroism (γ_0) makes it weaker. In fact, the light in the nonlasing mode is "chaotic" or "thermal", since integration of Eq. (3.6c) gives $\langle |\Delta I_y|^2 \rangle^{1/2} = \overline{I}_y$.

The amount of mode-partition noise will change in the same way as the average mode ratio. Weak dichroism will result in a strong nonlasing mode and large mode-partition noise. In this case, the noise level at low frequencies of the lasing

mode will be only slightly higher than that of the nonlasing mode, and both noise levels will be very large as compared to the noise in the total output power. On the other hand, strong dichroism will damp the nonlasing mode and the mode partition noise of the nonlasing mode will disappear below the total intensity noise, while the noise level of the lasing mode will decrease towards that of the total intensity noise.

3.4   Modal correlations

In this Section we will derive analytic expressions for the correlation function in the case of decoupled polarization noise presented in Section 3.3.

The total intensity is given by the sum of intensities in the orthogonally linear polarized lasing and nonlasing mode, $I(t) = I_x(t) + I_y(t)$. The spectral density of the total intensity noise (or the intensity noise spectrum) is given, via the Wiener-Khinchin theorem, as the Fourier-transform of the auto-correlation function,

$$
\begin{aligned}
S(\omega) = \quad \langle |I(\omega)|^2 \rangle \quad &= \int_{-\infty}^{\infty} \langle I(t)I(t+\tau) \rangle e^{i\omega\tau} d\tau \\
&= S_x(\omega) + S_y(\omega) + S_{xy}(\omega) + S_{yx}(\omega) ,
\end{aligned} \tag{3.7}
$$

where the individual noise spectra $S_{ij}(w)$ are given by similar integrals. The correlation function for the fluctuations in the lasing and nonlasing mode is defined by

$$
C_{xy}(\omega) = \frac{\mathrm{Re}(S_{xy}(\omega))}{\sqrt{S_x(\omega)\,S_y(\omega)}} , \tag{3.8}
$$

where $\mathrm{Re}(S_{xy})$ is the real part of the cross-spectral density.

To obtain this correlation from experimental data, it is more convenient to rewrite the correlation as

$$
C_{xy}(\omega) = \frac{S(\omega) - S_x(\omega) - S_y(\omega)}{2\sqrt{S_x(\omega)\,S_y(\omega)}}. \tag{3.9}
$$

The correlation is now expressed as a normalized balance between the total intensity noise and the fluctuations of both polarization modes.

For decoupled fluctuations, *i.e.*, $\langle \Delta I(t_1)\Delta I_y(t_2) \rangle = 0$, a case which naturally occurs when the power in the nonlasing mode is much smaller than that in the lasing mode ($\overline{I}_y \ll \overline{I}_x$), the correlation function can be reduced to,

$$C_{xy}(\omega) = \frac{-1}{\sqrt{1 + S(\omega)/S_y(\omega)}}. \tag{3.10}$$

Comparison of the measured correlation analyzed according to Eq. (3.9) or Eq. (3.10) can demonstrate whether polarization fluctuations are indeed decoupled from total intensity fluctuations.

A theoretical expression for the correlation can be obtained by substituting the noise spectra of Eqs. (3.6a-c) in Eq. (3.9), which gives a rather cumbersome result. Since in most experiments the correlation is investigated at low (MHz) frequencies, we will focus on the low-frequency limit

$$C_{xy}(\omega = 0) = \frac{-1}{\sqrt{1 + (4\frac{\gamma_0\gamma_{ro}}{\omega_{ro}^2})^2/R}}, \tag{3.11}$$

where $R = \overline{I}_y/\overline{I}_x$ is the mode ratio. Eq. (3.11) shows that for smaller dichroism, which corresponds to a relatively strong nonlasing mode and thus more mode-partition noise, the polarization fluctuations become perfectly anti-correlated. The degree of anti-correlation is a measure for the amount of mode-partition noise, as the correlation results from a balance between total intensity noise and polarization noise of the modes [see Eq. (3.9)]. Increasing the damping and/or decreasing the frequency of the relaxation oscillations leads to an increase of the low frequency noise in the total output power and lasing mode. This reduces the degree of anti-correlation [see Eq. (3.9) and (3.10)].

A demonstration of the frequency dependence of the correlation can be given by an expansion for $\omega \ll \omega_{ro}$,

$$C_{xy}(\omega \ll \omega_{ro}) \approx -1 + \frac{8}{R}\left(\frac{\gamma_{ro}\gamma_0}{\omega_{ro}^2}\right)^2 \left(1 + \omega^2/(4\gamma_0^2)\right)\left(1 + \omega^2/(4\gamma_{ro}^2)\right), \tag{3.12}$$

where we have used $\gamma_{ro} \ll \omega_{ro}$. The expansion of the square root in Eq. (3.10) is only valid when $C_{xy}(\omega \approx 0) \leq -0.8$. Eq. (3.12) shows that at higher frequencies the degree of anti-correlation decreases, because the amount of Lorentzian mode-partition noise decreases, whereas the total intensity noise increases.

3.5 Experimental results

In this Section, we compare results from experiments, performed on a VCSEL oscillating in the two TEM$_{00}$ polarization modes, with the theoretical results pre-

sented in Sections 3.2-3.4. Specifically, in Section 3.5.1 we discuss measured intensity and polarization-resolved noise spectra. In Section 3.5.2 we check whether the polarization fluctuations are decoupled from the total intensity noise. In Section 3.5.3, we verify specific results for the correlation based upon the developed two-mode theory, being the dependence of the correlation on the dichroism and relaxation oscillations, and on the frequency.

3.5.1 Intensity and polarization-resolved noise spectra

For the experiments we have used a batch of about 50 proton-implanted VCSELs [16]. The lasers consist of 1-λ cavity with three 8-nm-thick quantum wells. The VCSELs have a threshold injection current around 5 mA, while higher-order spatial modes start lasing above 10 mA. We have limited ourselves to the regime of fundamental transverse mode operation.

Almost every individual device fulfilled the requirements for a two-mode description discussed in Section 3.2; specifically, the condition for adiabatic elimination of the difference inversion has previously been shown to be valid for this particular set of VCSELs [50] and more than 90 % of the lasers had a sufficiently large birefringence to allow the "rotational averaging"of the state of polarization.

We concentrated on the devices that exhibited a polarization switch. As the polarization stability of these switching devices changes a lot as a function of current, they allow for a rather accurate comparison with theory. The requirement that the VCSEL should exhibit a polarization switch was quite a strong one for the batch under study and decimated the amount of suitable VCSELs to 6. Since a detailed study showed the polarization resolved intensity noise of the remaining devices to be similar, we will give the results for one laser only.

The selected VCSEL had a birefringence of 11 GHz and a polarization switch at a current of 8.2 mA, centered in its studied fundamental transverse mode regime between 6.0 mA and 9.5 mA. The threshold of this device was 5.0 mA and higher-order modes appeared at a current of 10.0 mA.

To measure the intensity noise of the lasing and nonlasing polarization mode, the emitted light was passed through a $\lambda/4$ wave-plate, a $\lambda/2$ wave-plate and an optical Faraday isolator. The polarization-resolved intensity noise was first measured with a 6-GHz photo receiver (New Focus 1534). In Fig. 3.1 the intensity noise of the lasing and nonlasing polarization mode is shown as traces (a) and (b), respectively, at a laser current of 7.5 mA. At low frequencies the intensity noise of the nonlasing and lasing mode is relatively high. The amount of low-frequency noise decreased when a combination of the two polarization modes was selected. A more detailed inspection of the mode-partition noise showed that the spectra
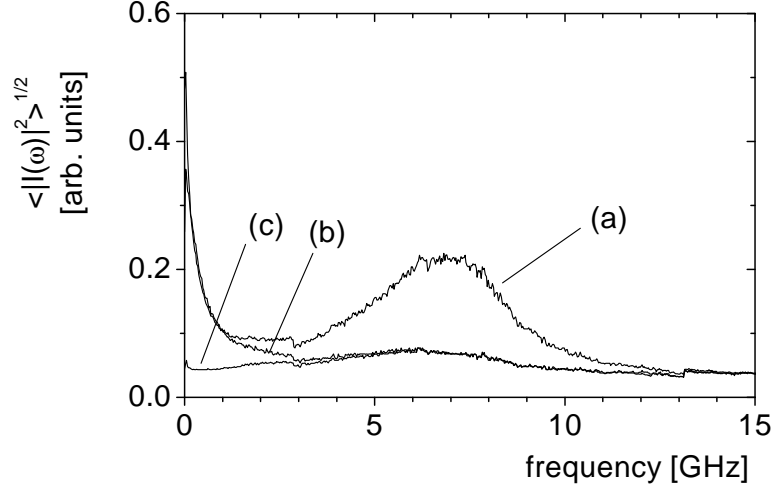
63

Figure 3.1: Broad-band intensity noise of the lasing (a) and nonlasing (b) polarization mode measured with a 6-GHz photo receiver. The lowest trace is the background noise (c). The spectrum of the lasing mode contains mode-partition noise and fluctuations due to relaxation oscillations, whereas the spectrum of the nonlasing mode only contains mode-partition noise.

were Lorentzian, having the same width for the lasing and the nonlasing mode. At higher frequencies the relaxation oscillations are visible in the spectrum of the lasing mode, but not in the (much weaker) nonlasing mode. The fits of the measured noise spectra were in qualitative good agreement with the theoretical expressions (3.6b) and (3.6c).

Next we measured the total intensity noise (not shown): it exhibited only the relaxation oscillation peak, but was somewhat noisy due to unintentional optical feedback, that existed after the necessary removal of the optical isolator. The 6-GHz detector is a fiber-coupled detector, in order to facilitate alignment, which made feedback from the fiber ends hard to avoid. Better measurements of the total intensity noise were done with a slower 1-GHz detector (New Focus 1601), which was aligned at a small angle to prevent feedback. In Fig. 3.2 four noise traces (a-d) are shown at laser current of 7.75 mA; traces (a) and (b) are from the lasing mode and nonlasing mode, respectively, and traces (c) and (d) are the total intensity noise and a reference measurement in the absence of light, respectively. Figure 3.2 demonstrates that the mode-partition noise in polarization-resolved spectra is much larger than the total intensity noise.

To measure the intensity noise more accurately at low frequencies, we used a detector with a home-built preamplifier with a bandwidth of 40 MHz. The noise
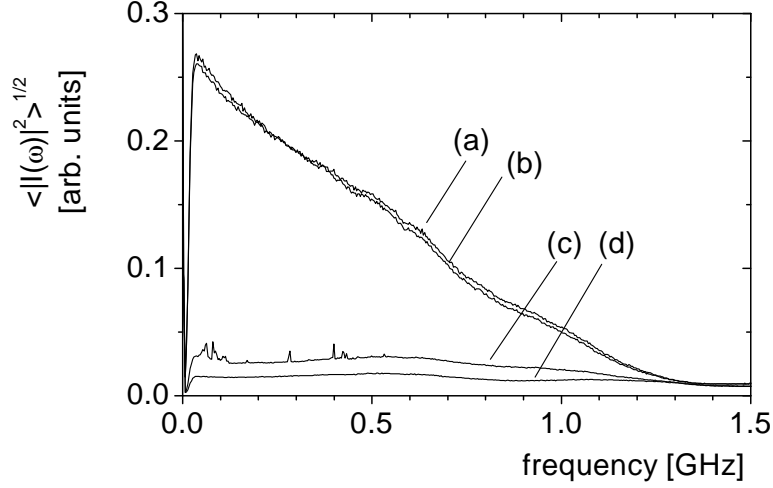
Figure 3.2: Intensity noise measurements with a 1-GHz photo receiver of : lasing mode (a), nonlasing mode (b), total intensity (c) and no-light reference (d). The polarization mode-partition noise clearly dominates over the total intensity noise.

level of this detector was calibrated with a white-light source and was found to be shot-noise limited above 0.2 mW (in the measurements, the total output power of the VCSEL was always above 1 mW). In Fig. 3.3 we show the noise spectra of the polarization modes and of the total output power, measured with the 40-MHz detector at a laser current of 7.75 mA. The lowest trace (d) displays the background noise. The absolute level of the total intensity noise [trace (c)] around 20 MHz was -148 dB/Hz, which was 3.7 dB above the shot noise level. Note that the low-frequency measurements with the 40-MHz detector zoom-in on the top of Lorentzian shaped mode-partition noise in Figs. 3.1 and 3.2. The frequency dependence of the noise traces is due to the detector response; after compensation for this, the polarization-resolved intensity noise [traces (a) and (b)] was found to be approximately flat up to 50 MHz (not shown), as expected from the other measurements. The intensity noise of the lasing mode was slightly higher than that of the nonlasing mode, again as expected from theory.

3.5.2 Decoupled fluctuations

In this Section we will check whether or not intensity and polarization fluctuations are decoupled. This is done by measuring the correlation and analyzing it according to Eq. (3.9) and Eq. (3.10) over the full range of fundamental transverse mode operation. Before we make this analysis, we will first study the mode partition
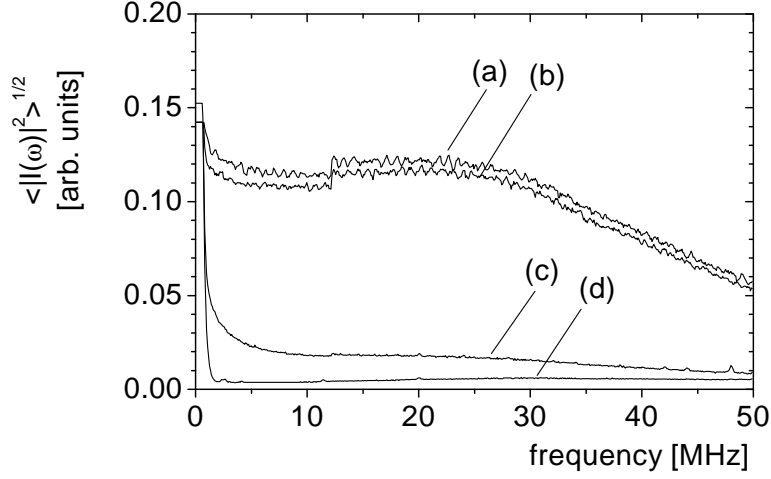
Figure 3.3: Intensity noise measurements with a 40-MHz photo receiver of: lasing mode (a), nonlasing mode (b), total intensity (c) and no-light reference (d).

noise as a function of laser current, starting with the 40-MHz detector.

Increasing the current towards the polarization switch ($i_{\text{switch}} \approx 8.2$ mA) we observed an increase in the noise levels of the lasing mode and nonlasing mode, whereas after the switch the noise levels decrease. The noise level of the lasing mode was always slightly higher than that of the nonlasing mode. The reason that the noise levels of the polarization modes reach a maximum at the hop is that the mode-partition noise is strongest where the polarization competition is also strongest, being around the switching current.

By monitoring the mode-partition noise with the 6-GHz detector, we found that the mode partition became stronger towards the hop, while the width of the Lorentzian ($2\gamma_0$) decreased. This explains the observed increase of the noise at MHz frequencies, since less damping (dichroism) results in a stronger nonlasing mode and more polarization noise concentrated around lower frequencies. After the hop the Lorentzian noise spectrum becomes weaker and broader. A more detailed discussion of the dichroism as a function of current will be given in Section 3.5.3.

The mode-partition dynamics discussed above had no observable effect on the total intensity noise. In fact it was impossible to distinguish between VCSELs with or without a polarization hop by observing only the total intensity noise. This confirms the decoupled polarization-fluctuation framework that we introduced in Sec. 3.3.

To determine the correlation of the polarization fluctuations, measured with

the 40-MHz detector, we first used Eq. (3.9). Since the correlation is proportional to the difference in total intensity noise and polarization-resolved intensity noise, it is obvious from the data (Fig. 3.3) that the fluctuations are anti-correlated because the intensity noise in each of the two polarization modes is almost equal and relatively large as compared to the total intensity noise. The correlation for low frequencies, as derived from the measurements in Fig. 3.3 using Eq. (3.9), is shown in Fig. 3.4 (solid curve); in the transformation of Fig. 3.3 into Fig. 3.4 we have compensated for the loss due to the polarization projection and subtracted the background noise quadratically. The fluctuations in the two polarization modes are indeed found to be almost completely anti-correlated.
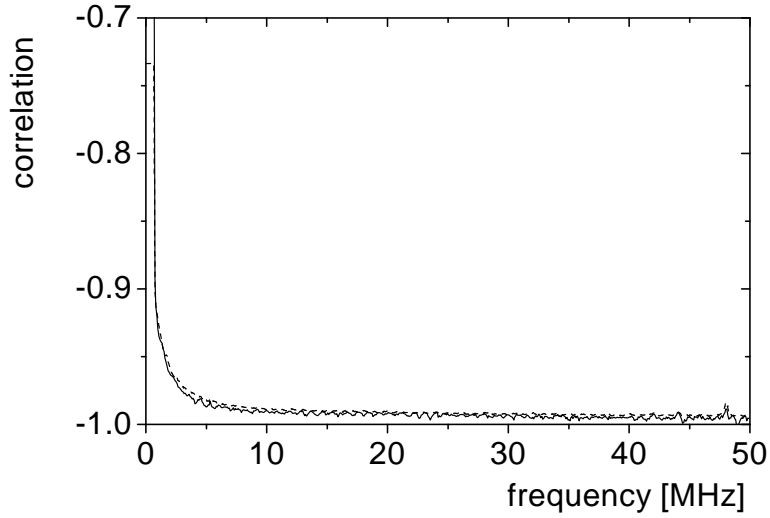

Figure 3.4: Correlation C_{xy} as a function of frequency calculated from measurements in Fig. 3.3, using Eq. (3.9) (solid curve) and Eq. (3.10) (dashed curve).

To check whether or not the polarization noise is decoupled from the intensity noise, we also calculated the correlation from the measured noise spectra of the nonlasing polarization mode and the total output power according to Eq. (3.10). This result is depicted as the dashed curve in Fig. 3.4. As it agrees with the correlation found from the analysis based upon Eq. (3.9), this proves again the validity of a decoupled description.

As a next step we measured the total intensity noise and the intensity noise in both polarizations as a function of current, to calculate the correlation as before. The result is shown in Fig. 3.5, where the correlation at 20 MHz is plotted as a function of laser current; circular and square data points show the correlation deduced using Eq. (3.9) and Eq. (3.10), respectively. From the good agreement

between the two methods of analysis, we conclude that the polarization fluctuations are decoupled from the total intensity noise over the full range of TEM$_{00}$ operation.
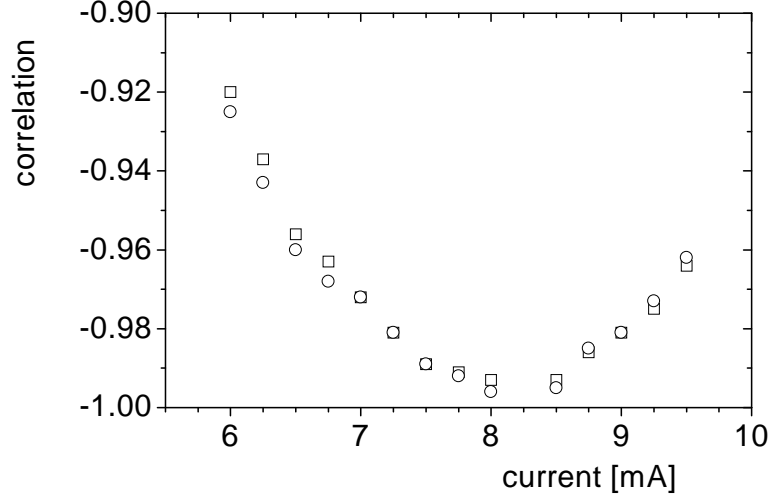

Figure 3.5: Correlation at 20 MHz as a function of the laser current. The circles show the correlation calculated from Eq. (3.9). The squares show the correlation calculated from Eq. (3.10), where it was assumed that the intensity and polarization fluctuations are decoupled.

When the current is increased towards the hop ($i_{\text{switch}} \approx 8.2$ mA) the degree of anti-correlation increases because the mode-partition noise becomes larger, whereas the total intensity noise is almost constant. Around the hop the modal fluctuations were found to be almost exactly anti-correlated, as $C_{xy} = -0.997(2)$. After the hop, where the mode-partition noise becomes again smaller due to larger damping (dichroism), the degree of anti-correlation decreases accordingly.

3.5.3 Correlation and its frequency dependence

So far, we have analyzed the correlation directly from its definition, as a normalized balance between total intensity fluctuations and the intensity fluctuations of the polarization modes [Eq. (3.9)]. We will now verify the theoretical predictions for the correlation [Eq. (3.11) and Eq. (3.12)], which are based on the two-mode theory developed in Sec. 3.2. In order to do this we will first independently determine the parameters ω_{ro}, γ_{ro}, γ_0 and R.

The relaxation oscillations were investigated by fitting the high-frequency intensity noise of the lasing mode to Eq. (3.6b). The upper box of Fig. 3.6 shows the

relaxation oscillation frequency (ω_{ro}) and damping (γ_{ro}) determined as a function of current. The relaxation oscillations were measured with the 6-GHz detector. Since for higher currents the relaxation oscillations frequency approaches almost 10 GHz, the response of the detector was calibrated and corrected for, which made measurements possible up to 12 GHz.
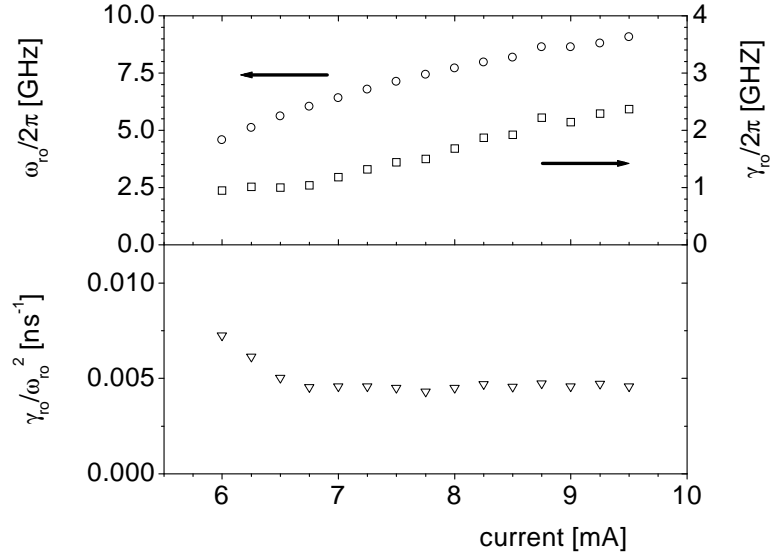

Figure 3.6: Current dependence of the relaxation oscillation frequency ω_{ro} and damping rate γ_{ro} (upper graph) and the ratio $\gamma_{\mathrm{ro}}/\omega_{\mathrm{ro}}^2$ (lower graph).

The important parameter for the correlation is the ratio $\gamma_{\mathrm{ro}}/\omega_{\mathrm{ro}}^2$ [Eq. (3.11)]. The lower box of Fig. 3.6 shows that this ratio is almost constant as a function of current, being 5×10^{-3} ns^{-1}; near threshold the ratio increases somewhat.

The effective dichroism (γ_0), which is the difference in gain between the lasing and nonlasing mode, can be measured in three different ways. The first method, as has been discussed in Section 3.5.1, is to measure the width $2\gamma_0$ of the Lorentzian shaped mode-partition intensity noise spectrum. In the second method, the dichroism γ_0 is obtained from the optical spectrum, as the difference in width (HWHM) of the Lorentzian shaped peaks of the lasing and nonlasing mode. The third method is to pass the VCSEL light through a polarizer oriented at 45°, which transmits 50% of the lasing and nonlasing mode. The intensity noise spectrum after this polarization projection contains a beat, with a resonance frequency equal to the birefringence, or frequency difference of the lasing and nonlasing mode. The width (HWHM) of this beat is equal to the effective dichroism. The dichroism as function of current is plotted in Fig. 3.7. All three methods reveal that the

69

dichroism becomes smaller towards the hop. The three methods are in reasonable agreement; there is no obvious cause for the remaining differences. Note that after the switch the dichroism (*i.e.*, the polarization stability) increases again. Figure 3.7 demonstrates that the current dependence of the dichroism, which results in a minimum at a certain current, is the actual origin of the polarization switch at that current. Recently we have shown experimentally that the remaining dichroism at the polarization hop is in fact the nonlinear dichroism ($2\kappa\mu/\Gamma$), *i.e.*, the polarization-dependent cross saturation [50,53]. The physical mechanism of the current dependence of the linear dichroism is still somewhat of a mystery. However, we have observed that this current dependence of the dichroism is roughly the same in almost every VCSEL in this batch; this includes VCSELs with small or large positive birefringence and even negative birefringence (see also [50]).
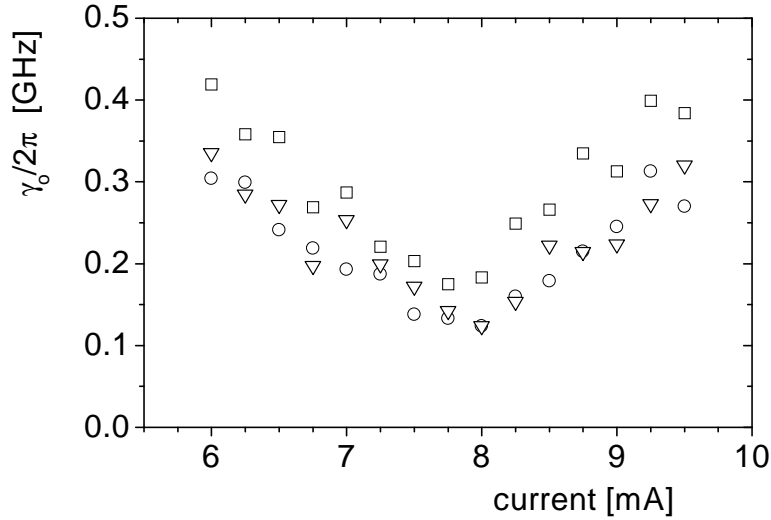

Figure 3.7: Dichroism as a function of laser current. The dichroism was determined from optical spectra with a Fabry-Pérot (triangles), from mode-partition noise spectra (circles) and from beat spectra between the polarization modes (squares).

The average intensity ratio of the nonlasing mode and lasing mode (R) was determined from polarization-resolved power measurements and Fabry-Pérot spectra. From power measurements we obtained values for R ranging between 8×10^{-3} and 1.7×10^{-2}, whereas the mode ratio determined from the areas under the peaks in the optical spectrum resulted in values between 5×10^{-3} and 1.7×10^{-2}. For both methods the mode ratio was maximum (1.7×10^{-2}) near the polariza-

tion switch. As mentioned in Sec. 3.3, one expects the mode ratio R to be approximately equal to the spontaneous emission noise strength D divided by the effective dichroism γ_0 (see Sec. 2.6 and ref. [50]). Larger dichroism increases the polarization stability and thus the mode ratio, whereas more noise makes the nonlasing mode stronger and decreases the mode ratio.

Comparing the measured mode ratios to the measured variations in the dichroism γ_0, we found somewhat better agreement for the spectral measurements of the mode ratios. We attribute the difference to very weak spontaneous emission in many very heavily damped higher-order transverse modes. This was confirmed by the observation of a flat offset in the Fabry-Pérot spectrum of the nonlasing mode. In order to put this into the proper perspective, we emphasize that it was not possible to identify individual higher-order modes with a grating-based spectrum analyzer at intensities above $10^{-3}\times$ that of the nonlasing mode. For our calculation of the correlation function [Eq. (3.11)] we will use the mode ratios from the power measurements, since these are more closely related to the direct measurement of the correlation.
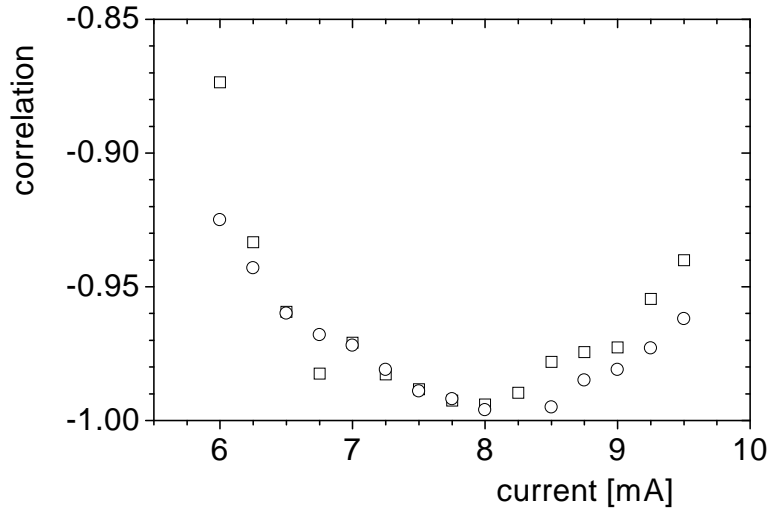

Figure 3.8: Correlation at 20 MHz as a function of the laser current. The circles show the directly measured correlation function (same circular points as in Fig. 3.5). The squares show the correlation calculated from measurements of the relaxation oscillations, dichroism and mode ratio using Eq. (3.11).

The correlation of polarization fluctuations as calculated from the measured relaxation oscillation frequency and width, the dichroism from the Fabry Pérot, and

the mode ratio is shown in Fig. 3.8 (squares). Figure 3.8 demonstrates that the correlation "calculated"from Eq. (3.11) is in quantitative agreement with the directly measured correlation from the noise spectra based upon Eq. (3.9) (circles).

An experimental demonstration of the frequency dependence of the correlation is given in Fig. 3.9 (solid curve), where the correlation was determined from the noise in the total intensity and the individual polarization modes measured with the 1-GHz detector. We note that the detector responsivity divides out in the calculation of $C_{xy}(\omega)$. At higher frequencies the degree of anti-correlation drops, since the Lorentzian shaped mode-partition noise spectrum decreases and approaches the total intensity noise spectrum. Fitting the measured correlation with Eq. (3.12) (dashed curve in Fig. 3.9) resulted in a value of $\gamma_0/2\pi = 0.16$ GHz and $\gamma_{\mathrm{ro}}/2\pi = 1.0$ GHz for the damping of the polarization fluctuations and of the relaxation oscillations, respectively. These values are in reasonable agreement with direct measurements, which yield $\gamma_0/2\pi = 0.15$ GHz and $\gamma_{\mathrm{ro}}/2\pi = 1.5$ GHz, respectively.
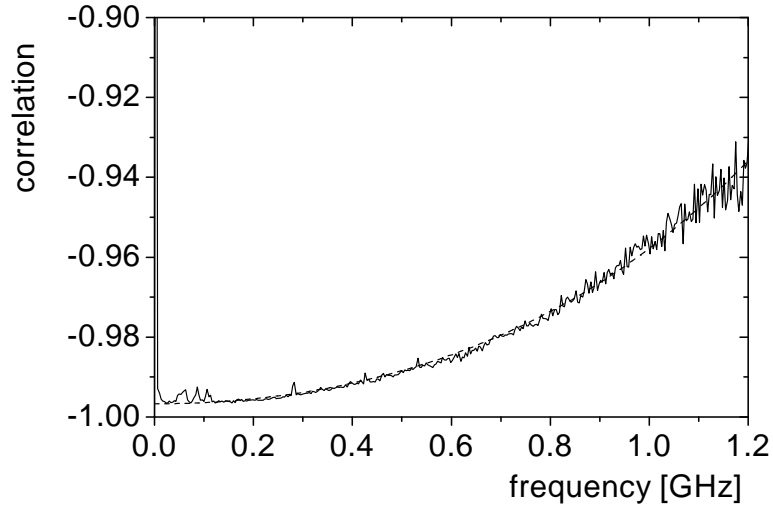

Figure 3.9: Correlation C_{xy} as a function of frequency determined from measurements in Fig. 3.2 with Eq. 3.9 (solid curve). The dashed curve is a fit to Eq. (3.12).

3.6 Conclusion

In conclusion, we have presented a two-mode theory valid for the two polarization modes of a practical VCSEL. With practical VCSELs we mean VCSELs that

have dominant linear birefringence, strongly coupled spin reservoirs and a non-lasing mode that is much weaker than the lasing mode. We have derived noise spectra for the total output power and for the intensities of the separate polarization modes and predicted that for practical VCSELs, polarization fluctuations are *decoupled* from the total intensity noise. We have quantitatively shown how the correlation function C_{xy} is expected to depend on the dichroism and relaxation oscillations. Furthermore we have demonstrated that the correlation function is frequency dependent.

The experimental results confirm this remarkably simple description of decoupled polarization dynamics. Specifically, *(i)* we have observed no effect on the total intensity noise from the polarization dynamics, *(ii)* we have checked polarization fluctuations to be decoupled from the intensity fluctuations by analyzing the correlation with Eq. (3.9) and Eq. (3.10), *(iii)* the measured correlation was found to depend on the dichroism and relaxation oscillations as was expected from theoretical predictions, *(iv)* we have also experimentally demonstrated the frequency dependence of the correlation function.

Furthermore we have demonstrated, by three independent methods, that the dichroism has a minimum at the polarization switch (Fig. 3.7). A physical explanation of this current dependence of the linear dichroism, *i.e.*, the actual origin of the polarization switch, is still under investigation.

The validity of a decoupled description of the polarization noise has interesting consequences for the generation of squeezed light in a single-transverse-mode VCSEL. Since we have observed the polarization fluctuations to be decoupled from the total intensity noise, one expects that polarization dynamics cannot deteriorate squeezing. We have addressed these aspects in detail elsewhere [52].

Polarization switching of a vertical-cavity semiconductor laser as a Kramers hopping problem [1]

We report stochastic polarization switching in vertical-cavity semiconductor lasers, with residence times that vary by eight orders of magnitude for a single such laser by changing its switch current with a hot-spot technique. In spite of the potentially complicated polarization dynamics of VCSELs, the experimental results agree with Kramers hopping in a 1D double-well potential initiated by quantum fluctuations. We confirm the validity of this surprisingly simple theoretical model by independent measurements of the potential barrier between the wells and the spontaneous emission noise strength.

4.1   Introduction

The vertical-cavity surface-emitting laser (VCSEL) is a novel type of semiconductor laser, which is not completely understood. This refers in particular to important issues like polarization stability, polarization switching and polarization modulation. It is generally believed that polarization behaviour of VCSELs is extremely complicated, in particular when considering multi-transverse-mode devices [13,30,54–56]. However, a greatly simplified theory was developed, which allows analytical solutions and which predicts that the polarization dynamics of VCSELs reduces to the Kramers hopping problem of a 1D double-well potential (see Sec. 2.6 and [50]). We note that the Kramers double-well potential model has a long history [39] and has been applied in many subfields of physics and chemistry [57,40]. In this chapter, we validate this surprisingly simple theory for practical VCSELs by observing and analyzing stochastic polarization switching.

---

[1]M. B. Willemsen, M. U. F. Khalid, M. P. van Exter, and J. P. Woerdman, Phys. Rev. Lett. **82**, 4815-4818 (1999)

The important quantity in the Kramers model is the average residence time $\langle T \rangle$ (also called average dwell time [50] or first-passage time [57,40]) which is the average time before a switch takes place; $\langle T \rangle$ depends on the potential barrier between the wells and the strength of the quantum fluctuations that initiate switching. The experimental validation of the analytical VCSEL theory [50] has become possible by using a hot-spot technique; this has allowed us to manipulate the Kramers potential of a *single* VCSEL. In this way we have been able to change the average residence time $\langle T \rangle$ by eight orders of magnitude, in quantitative agreement with theory.

The reason for this dramatic change in residence times is that a VCSEL has a rather critical balance between the deterministic force that pins the polarization and the stochastic force due to quantum fluctuations (spontaneous emission) that triggers switching. The anisotropies which determine the stationary polarization are relatively small, because of the nominal cylindrical symmetry of the cavity, whereas the spontaneous emission noise is relatively large due to the small size of the device [50].

4.2   1D Kramers model

In this section we will discuss the 1D Kramers model for polarization switching. As the underlying theoretical framework has already been reviewed in chapter 2, we will only briefly highlight its essentials. Starting point is theoretical and experimental work [50,25,22] showing that the polarization dynamics of quantum-well VCSELs, as derived from a split-level inversion model [23,15,26], after adiabatic elimination of the spin-difference inversion is similar to that of a class A type (gas or dye) laser when the anisotropies are not too big. In this description the polarization, described by the polarization angle (ϕ) and ellipticity angle (χ), is driven by dispersive and absorptive anisotropies. Specifically, the effective birefringence (ω_0) and effective dichroism (γ_0) create a difference in frequency and gain between the lasing and nonlasing polarization, respectively. Both ω_0 and γ_0 consist of a linear part, which quantifies how much the cylindrical symmetry of the cavity is broken, and a nonlinear part, which corresponds to a polarization dependence of the optical saturation and is thus proportional to the pump parameter $\mu = (i/i_{\mathrm{thr}}) - 1$. When linear birefringence is the dominant anisotropy (which is the case for practical VCSELs [50,25,22]), we have

$$\omega_0 = \sqrt{\omega_{\text{lin}}^2 + 2\omega_{\text{lin}}\omega_{\text{non}} - \gamma_{\text{non}}^2} \, , \tag{4.1a}$$

$$\gamma_0 = \gamma_{\text{lin}} \cos(2\beta) + \gamma_{\text{non}} \, , \tag{4.1b}$$

$$\omega_{\text{non}} = \alpha\gamma_{\text{non}} = \alpha\frac{\kappa}{\Gamma}\mu \, , \tag{4.1c}$$

where ω_{lin} and ω_{non} are the linear and nonlinear birefringence, γ_{lin} and γ_{non} the linear and nonlinear dichroism, κ the decay rate of the intra-cavity field, Γ the decay rate of the spin-difference inversion divided by that of the spin-averaged inversion and α the phase-amplitude coupling factor. The angle β, between the axes of the linear birefringence and linear dichroism, is introduced to describe nonaligned linear anisotropies. For $\beta \neq 0$ the effect of linear dichroism is reduced, because the linear dichroism must be projected onto the axis of the linear birefringence, since linear birefringence has been assumed to be the dominant anisotropy.

Besides the deterministic force due to anisotropies, which sets the steady-state polarization, there is also a stochastic force due to quantum fluctuations. The presence of spontaneous emission results in a "noise cloud" around the steady-state polarization (ϕ, χ) on the Poincaré sphere (Fig. 4.1). (On the Poincaré sphere the equator corresponds to all states of linear polarization, the poles to the two states of circular polarization, and the rest to elliptically-polarized light.)

In general, the fluctuations in ϕ and χ can be quite different. However, for practical VCSELs, where the linear birefringence is the dominant anisotropy, this difference in fluctuations of both angles is negligible and the polarization dynamics can be reduced to that of single angle φ, where $\cos(2\varphi) = \cos(2\chi)\cos(2\phi)$ [50]. The very complicated polarization dynamics of VCSELs is then reduced to the standard model of diffusion in a one-dimensional potential. To obtain more insight into the statistics we derive from the Fokker-Planck equation for the polarization [50] as steady-state probability density

$$P(\varphi)\,d\varphi \propto \sin(2\varphi)\,e^{-V(\varphi)/D}\,d\varphi \, , \tag{4.2a}$$

$$V(\varphi) = -\frac{\gamma_{\text{lin}}\cos(2\beta)}{2}\cos(2\varphi) - \frac{\gamma_{\text{non}}}{8}\cos(4\varphi). \tag{4.2b}$$

The parameter D is the strength of the Langevin noise source that models spontaneous emission. We will now limit ourselves to a *symmetric* double-well potential $V(\varphi)$, where the modes are equivalent ($\gamma_{\text{lin}}\cos(2\beta) = 0$). This potential has in

Chapter 4

fact two series of minima, at $2\varphi = 0 \pmod{2\pi}$ and $2\varphi = \pi \pmod{2\pi}$, which corresponds to pure *x*- and *y*-polarized emission. Noise can make the system switch between two neighboring minima. A sketch of the evolution of the two polarization angles ϕ and χ on the Poincaré sphere during a switch is shown in Fig. 4.1. The switch trajectory is discussed in more detail in chapter 5. The switching occurs between two orthogonally linear polarized states, which lie diametrically in the equatorial plane. The trajectory which connects the polarization before and after the switch is a spiraling motion because we assumed the linear birefringence to be dominant. The angle 2φ measures the azimuthal position of the almost circular orbits around the *x,y*-axis.
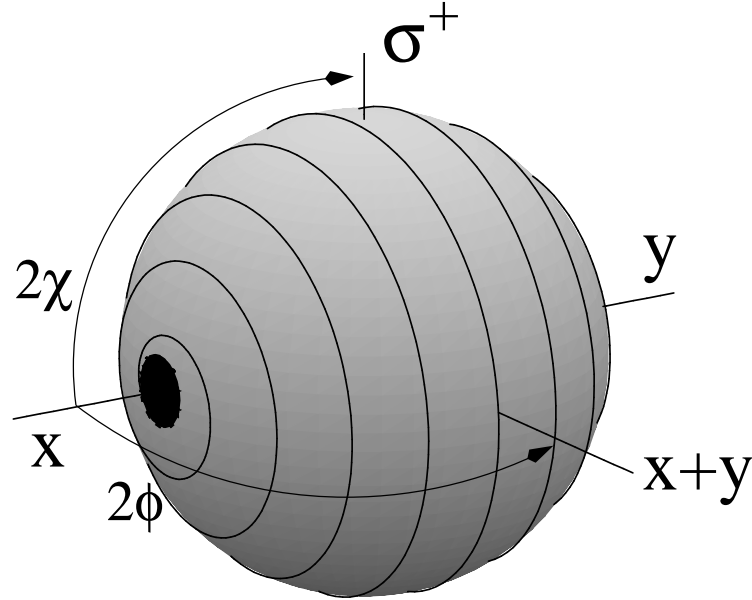

Figure 4.1: Sketch of the evolution of the polarization angles χ and ϕ during the switch, plotted on the Poincaré sphere. The switch corresponds to a spiraling motion between two linear polarizations, diametrically opposed in the equatorial plane. The black dot indicates the "noise cloud".

Straightforward calculation yields an exponential distribution of residence times, with an average residence time of each eigenpolarization (for $\gamma_{\text{non}} > D$) given by

$$\langle T \rangle \approx \sqrt{\frac{\pi D}{\gamma_{\text{non}}}} \frac{1}{\gamma_{\text{non}}} \exp\left(\frac{\gamma_{\text{non}}}{4D}\right) . \tag{4.3}$$

78

Since the potential is symmetric, $\langle T \rangle$ is the same for both linear polarizations, *i.e.*, the laser switches symmetrically. The rate of switching is thus expressed in terms of the nonlinear dichroism γ_{non}, which specifies the barrier between the two potential wells, and the diffusion coefficient D. The exponent in Eq. (4.3) depends quadratically on the pump parameter μ, because the potential barrier scales with the pump ($\gamma_{\mathrm{non}} \propto \mu$), due to polarization-dependent saturation, and $D \propto 1/\mu$ (Schawlow-Townes). This "quadratic exponential" dependence makes the residence time a very sensitive function of the pump parameter.

4.3   Observation of stochastic polarization switching

For the experiments we had a batch of about 50 proton implanted $Al_xGa_{1-x}As$ VCSELs available, operating at 850 nm [16]. Within the range of fundamental transverse mode operation, between $i_{\mathrm{thr}} \approx 5$ mA and $i \approx 11$ mA, only a few of these lasers switched polarization. Most of these polarization-switching devices exhibited hysteresis, because the switching occurred at relatively large currents, whereas some showed stochastic hopping since they switched at lower currents. To make a comparison with theory, very large numbers of VCSELs would be needed to end up with a reasonable number that switch at relatively low currents. Furthermore such a comparison is always hindered by unintentional differences from device to device. In order to solve this problem we used the so called hot-spot technique [58] to vary the switch current of a *single* laser.

With this tool we changed the strength and orientation of the linear birefringence by applying stress with a focussed 780-nm laser beam (typically 30 mW) that locally heats the wafer surface next to the VCSEL. In experiments with the hot spot we have not noticed a direct effect on the dichroism, only an indirect one. By changing the position of the hot spot we can rotate the axes of the birefringence, so that the *projected* dichroism will change, assuming that linear birefringence is still the dominant anisotropy. By rotating the birefringence axes the projected dichroism, *i.e.*, the first term in Eq. (4.2b), was cancelled, which results in a bistable system with the laser hopping symmetrically between two linear polarizations determined by the axes of the linear birefringence. By adjustment of the hot-spot power the VCSEL can now be forced to hop at any current within the range of the fundamental transverse mode.

To measure the polarization of the emitted VCSEL light we use three different tools (see Fig. 2.3 in chapter 2): a Fabry-Pérot interferometer to measure the optical spectrum, a fast photo-diode in combination with a spectrum analyzer to measure polarization-resolved intensity noise spectra (detection bandwidth 6 GHz) and a fast photo-diode in combination with an oscilloscope to measure time
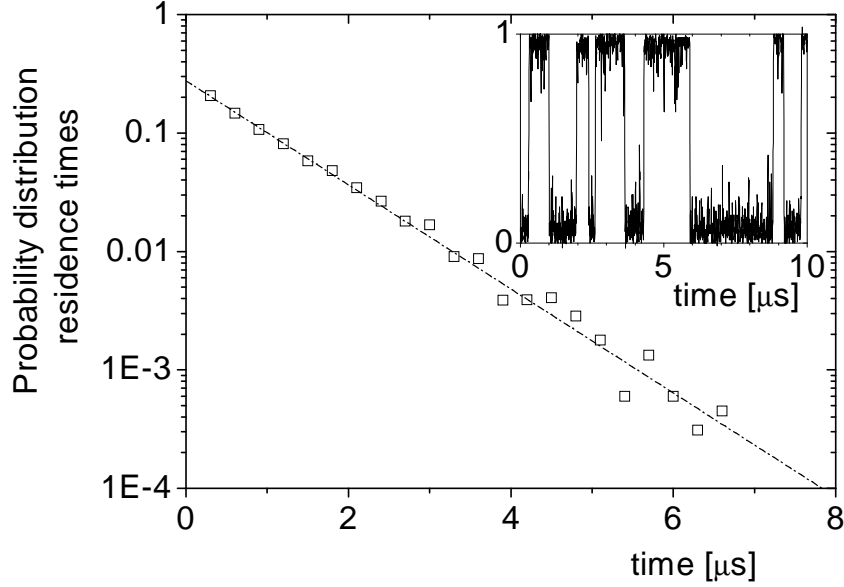
traces (detection bandwidth 500 MHz).

Figure 4.2: Distribution of residence times of a polarization switching VCSEL at $i = 6.4$ mA. From the exponential fit the average residence time was found to be 1.0 μs. The inset shows a small part of the polarization resolved time-trace, the full trace was used to calculate the distribution.

The inset of Fig. 4.2 shows a typical time trace of the *x*-polarized part of the output power of a single-transverse-mode VCSEL that hops at current of 6.4 mA. Spectral measurements with a Fabry-Pérot interferometer (not shown) confirmed that the two levels in the time trace corresponded with the two different linear VCSEL polarizations in the optical spectrum, only one of which was lasing at each time; from this we conclude that hopping occurs between the two polarizations in the fundamental transverse mode. A very long time trace, containing more than 10^4 switches, was used to calculate the probability distribution of residence times, as shown in Fig. 4.2. This distribution is exponential, as expected from theory, with a fitted average residence time of 1.0 μs. We checked that the statistics of both levels in the time-trace were the same.

Next we increased the current and adjusted the hot-spot power and/or position until the VCSEL hopped again. In this way the residence times were determined for different hop currents; the combined result is shown in Fig. 4.3. Note that each point corresponds with symmetric hopping. As one can see in Fig. 4.3, for low currents switching occurs on a sub-microsecond time scale, whereas for higher

currents the time scale rapidly increases to seconds. Such a huge change in the residence times (about eight orders of magnitude) has never been observed before.
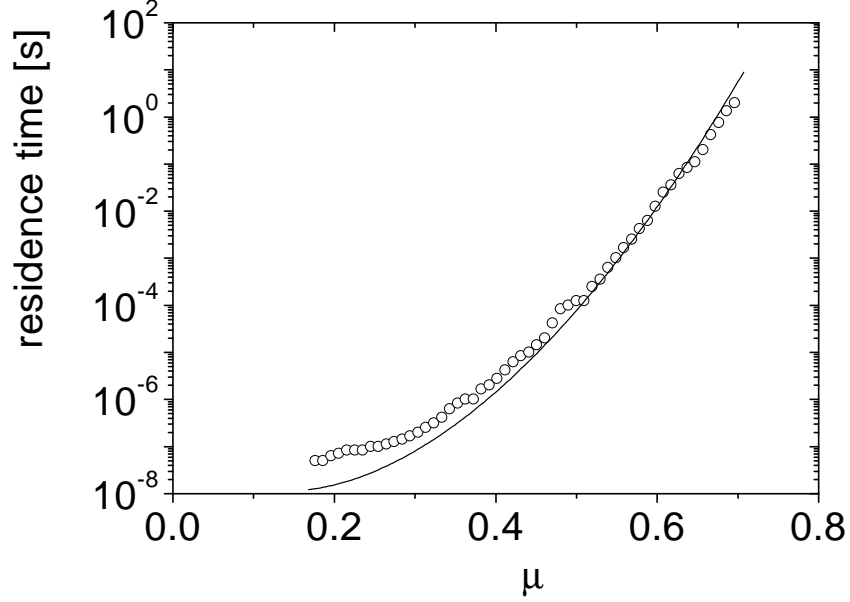

Figure 4.3: Residence times as a function of the normalized pump parameter μ ; the dots are experimental data and the line is a theoretical fit corresponding to Eq. (4.3).

Measurements have been repeated for different VCSELs of our batch; the results shown in Fig. 4.3 are also representative for the other devices. An attempt to measure the time it takes for the polarization to actually switch gave an upper limit of several nanoseconds. Real-time measurements of the polarization during a polarization switch are presented in chapter 5. For the theory to be valid the inverse of this time must be much smaller than the linear birefringence ω_{lin}, which causes the spiral motion during the switch [50]. As $\omega_{\mathrm{lin}} \approx 15$ ns^{-1} (see below) we satisfy this condition.

We will now discuss the independent measurements of both the deterministic and stochastic force which determine the residence time. First we have measured the effective anisotropies of the switching laser (Fig. 4.3) with polarization homodyne detection [50,26]. The nonlinear parts of the anisotropies (and thus also the linear parts) can be extracted from the discontinuities in the effective anisotropies around the switch [see Eq. (4.1a-c)], where the linear anisotropies change sign, but the nonlinear ones do not. (This is because linear anisotropies generate dif-

ferences with respect to two orthogonal linear polarizations, whereas nonlinear anisotropies act the same on every linearly polarized state). As the switch current could be set with the hot spot, we could measure the nonlinear birefringence and nonlinear dichroism (= depth of the potential well) as a function of $\mu = (i/i_{\mathrm{thr}}) - 1$ (see Fig. 4.4). From the straight-line fits [Eq. (4.1c)] we determined the absolute strength of the nonlinear anisotropies (at $\mu = 1$) as $\omega_{\mathrm{non}} = 4.5$ ns^{-1} and $\gamma_{\mathrm{non}} = 1.5$ ns^{-1}, which implies $\alpha \approx 3$ and $\Gamma \approx 200$, assuming the cavity decay rate to be $\kappa = 300$ ns^{-1}. Furthermore we found that $\omega_{\mathrm{lin}} \approx 15$ ns^{-1}, so that linear birefringence is indeed the dominant anisotropy, $\omega_{\mathrm{lin}} \gg \omega_{\mathrm{non}}, \gamma_{\mathrm{non}}$. The fitted threshold current in Fig. 4.4 was 5.1 mA, which is slightly higher than the value of 4.8 mA determined from the output-input curve.
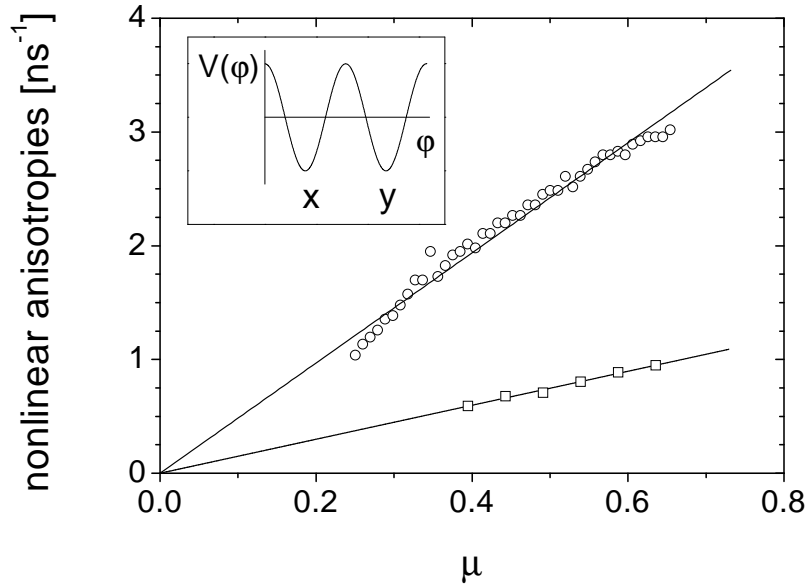

Figure 4.4: Measured nonlinear birefringence ω_{non} (circles) and nonlinear dichroism γ_{non} (squares) as a function of the normalized pump μ ; the lines are theoretical fits [Eq. (4.1c)]. The inset shows a sketch of the potential; the barrier between two adjacent wells is proportional to γ_{non}.

To measure the amount of spontaneous emission we have determined the optical linewidth with a self-heterodyne fiber-delay setup. The measured linewidth $\Delta \nu = (1 + \alpha^2) D / \pi$ was about 20 MHz at $\mu = 1$, which corresponds with a diffusion rate $D^{\mu=1}$ of 7-12 μs^{-1}, where the spread accounts for uncertainties in α and $\Delta \nu$.

These experimentally determined values of the potential well depth and the

spontaneous emission noise are fully consistent with the fit values of $\kappa/\Gamma = 1.5$ ns^{-1} and $D^{\mu=1} = 7.5$ μs^{-1} that we obtained when Eq. (4.3) was fitted to the data shown in Fig. 4.3. Note the good quality of the fit; we attribute the deviations for low pump values in Figs. 4.3 to the break down of the validity condition $\gamma_{\mathrm{non}} > D$ of Eq. 4.3.

4.4 Conclusion

Our work has an interesting consequence for controlled polarization switching in VCSELs, where the double-well potential is made asymmetric, and the laser is forced to switch, by changing the laser current across a deterministic hop. In that case there are two parameters that determine the residence times; *(i)* the noise strength, *(ii)* the asymmetry of the potential set by the change in current. For polarization modulation it is preferable, for technical reasons, to have a small current-modulation depth. However, too small a modulation depth will not reduce the double well to a single well, leading to the response time and switch rate being limited by the amount of spontaneous emission noise. Furthermore we note that the signal-to-noise ratio for polarization modulated devices depends on the noise strength in a similar way as in the so-called stochastic-resonance phenomenon [59,60].

In conclusion, we have experimentally studied symmetric polarization switching in VCSELs by changing their switch current with the hot-spot technique and thus tailoring the Kramers potential of an individual device. The results confirm the validity of an analytical theoretical framework for the polarization of practical VCSELs [50].

Chapter 5

Anatomy of a polarization switch of a vertical-cavity semiconductor laser [1]

Using a streak camera we have measured the three Stokes polarization parameters during a polarization switch of a vertical-cavity semiconductor laser. The switch occurs along a cork-screw path on the Poincaré sphere and takes on average a few nanoseconds; this value agrees with a theoretical treatment based upon the Fokker-Planck equation.

5.1 Introduction

The semiconductor vertical-cavity surface-emitting laser (VCSEL) is the simplest conceivable micro-cavity laser, with a basically one-dimensional cavity matched to a single wavelength of light. VCSELs allow experimental study of basic issues in microlaser noise [48,61]. The small modal volume of a VCSEL results in strong spontaneous emission noise; in combination with the high degree of cylindrical symmetry, this leads to polarization switching between linear polarizations (*x* and *y*) [13]. In this chapter, we report a study of the *transient* aspects of polarization bistability of a VCSEL as observed with a *single-shot* streak camera. Polarization bistability and switching in lasers in general, and VCSELs in particular, are issues that have attracted a lot of attention over the years [13,30,55,40,23,62–65,53]. The most important quantity that has been studied experimentally so far is the residence time, *i.e.*, the average time before a switch actually takes place (see chapter 4 and refs. [63,40,53]). However, the "jump"between the steady-states has not been addressed directly, presumably because it occurs on a much faster time scale. Proper understanding of the switching route, which is generally embedded in a 3D state space (see below), requires *time-resolved* measurements.

5.2   Polarization switch trajectory

To discuss our results we use the Poincaré sphere to represent all states of polarization. As spherical coordinates we introduce 2ϕ and 2χ, where ϕ corresponds to the polarization orientation and χ to the ellipticity. The equator corresponds to all linear polarizations, the poles to the two circular polarizations, and the rest to elliptically polarized states. The Cartesian axes of the Poincaré sphere are the normalized Stokes parameters, given by $s_1 = \cos(2\phi)\cos(2\chi)$, $s_2 = \sin(2\phi)\cos(2\chi)$, and $s_3 = \sin(2\chi)$, with $s_1^2 + s_2^2 + s_3^2 = 1$. The polarization during a polarization switch between the linear x and y-polarization can be visualized as a trajectory on the Poincaré sphere between $s_1 = 1$ and $s_1 = -1$.

Our theoretical framework is a rate-equation model, which is based upon an approximation of the quantum-well band structure of the VCSEL by discrete spin levels [15]. The spin-difference inversion can be eliminated adiabatically [26]; this procedure has been experimentally validated for practical VCSELs [22,50]. Furthermore, the fluctuations of the spin-averaged inversion and the total intensity are almost decoupled from the polarization fluctuations [15,66] and can be neglected in the present context. All this results in the following set of rate equations for the normalized Stokes parameters s_1, s_2 and s_3 (see Sec. 2.6 and ref. [50]):

$$\frac{ds_1}{dt} = \gamma_\parallel(s_2^2 + s_3^2) + 2\omega_{\text{non}}s_2s_3 + 2\gamma_{\text{non}}s_1s_3^2 + f_{s_1} , \tag{5.1a}$$

$$\frac{ds_2}{dt} = -\gamma_\parallel s_1s_2 - \omega_{\text{lin}}s_3 - 2\omega_{\text{non}}s_1s_3 + 2\gamma_{\text{non}}s_2s_3^2 + f_{s_2} , \tag{5.1b}$$

$$\frac{ds_3}{dt} = -\gamma_\parallel s_1s_3 + \omega_{\text{lin}}s_2 - 2\gamma_{\text{non}}s_3(s_1^2 + s_2^2) + f_{s_3} . \tag{5.1c}$$

The polarization dynamics is determined by dispersive anisotropies (ω_{lin} and ω_{non}) and absorptive anisotropies ($\gamma_\parallel$ and γ_{non}), which create a difference in frequency and gain between the two polarizations, respectively. Both anisotropies consist of a linear part (ω_{lin} and $\gamma_\parallel$), which quantifies how much the cylindrical symmetry of the cavity is broken, and a nonlinear part (ω_{non} and γ_{non}), which corresponds to polarization-dependent saturation of the gain medium. The nonlinear anisotropies, which are remnants of the adiabatically eliminated spin-difference inversion, are the nonlinear birefringence $\omega_{\text{non}} = \alpha\gamma_{\text{non}}$ and the nonlinear dichroism $\gamma_{\text{non}} = (\kappa/\Gamma)\mu$, where α is the amplitude-phase-coupling factor, κ the cavity decay rate, Γ the decay rate of the spin-difference inversion divided by that of the spin-averaged inversion, and $\mu - 1$ is the normalized pump parameter [50]. Eqs. (5.1a-c) describe the interplay between the stochastic Langevin forces (f_{s_1},

f_{s_2}, f_{s_3}) and the deterministic anisotropy forces, which drive the polarization back to its steady state.

In practical VCSELs $|\omega_{\text{lin}}| \gg |\gamma_{\parallel}|, \omega_{\text{non}}, \gamma_{\text{non}}$ [50], so that the emitted light is either x or y-polarized, depending on the sign of $\gamma_{\parallel}$ (for $\omega_{\text{lin}} > 0$ and $\gamma_{\parallel} > 0$ the x polarization, *i.e.* $s_1 = 1$, has the highest eigenfrequency and highest modal gain). The fast ω_{lin}-rotation around the s_1-axis [see Eqs. (5.1b) and (5.1c)] results in a rapid out-of-phase oscillation for s_2 and s_3 that can be averaged over in Eq. (5.1a), reducing the s_1 dynamics to a Kramers problem. Specifically, the second term in Eq. (5.1a) averages out (as $\langle s_2 s_3 \rangle \approx 0$) and the third term at the rhs, with $\langle s_3^2 \rangle \approx (1 - s_1^2)/2$, acts as a symmetric Kramers double well potential, with minima at $s_1 = \pm 1$ and a barrier height $\gamma_{\text{non}}/4$ at $s_1 = 0$. Previously it has been demonstrated that switches occur when $\gamma_{\parallel} \simeq 0$ [50,66], *i.e.*, the first term at the rhs of Eq. (5.1a) is zero. In this case the VCSEL is bistable and switches stochastically between the x and y-polarization [53]. We thus predict that during a polarization switch the s_1 Stokes parameter will gradually change from $s_1 = 1$ to $s_1 = -1$; this is the escape from one well to the other.

One may wonder if there is a different time duration of uphill paths (from $s_1 = 1$ to $s_1 = 0$), which are mainly stochastic, and downhill paths (from $s_1 = 0$ to $s_1 = -1$), which are mainly deterministic. For the calculation of the average transit time and in the experiment (see below) the probabilities of both paths are important. We have found that the various escapes obey a "stochastic inversion symmetry" around the potential maximum at $s_1 = 0$, in the sense that each uphill path has a mirror-imaged downhill path that is equally likely [2]. It is thus sufficient to consider only the downhill evolution. When we approximate the potential barrier around $s_1 = 0$ by an inverted parabola and use ref. [67] we find that the conditional probability to find a value of s_1, assuming a start at $s_1 = 0$, is a Gaussian with a width that eventually increases exponentially in time. As the parabolic description is only valid close to $s_1 = 0$, we define the transit time T_{tr} as the time it takes to go from $s_1 = 1/2$ to $s_1 = -1/2$. The mean transit time $\langle T_{\text{tr}} \rangle$, thus defined, is given by

$$\langle T_{\text{tr}} \rangle \approx \frac{1}{\gamma_{\text{non}}} \ln\left(\frac{\gamma_{\text{non}}}{8D} + 1\right), \tag{5.2}$$

---

[2]The "stochastic inversion symmetry" is a consequence of the inversion symmetry of the stationary Kramers potential. It represents an extended form of detailed balance, which states that the joint probability to go from A to B in a certain time interval is equal to the joint probability to go from B to A [67], as the low conditional probability for an uphill path is compensated by the high probability to start at the bottom. Similarly, the high conditional probability for a downhill path is compensated by the low probability to start at the barrier.

where γ_{non} and D are proportional to the barrier height and spontaneous emission noise strength (with $\langle f_{s_i}(t) f_{s_i}(t+\tau)\rangle = 4D[1 - s_i^2]\delta(\tau)$).
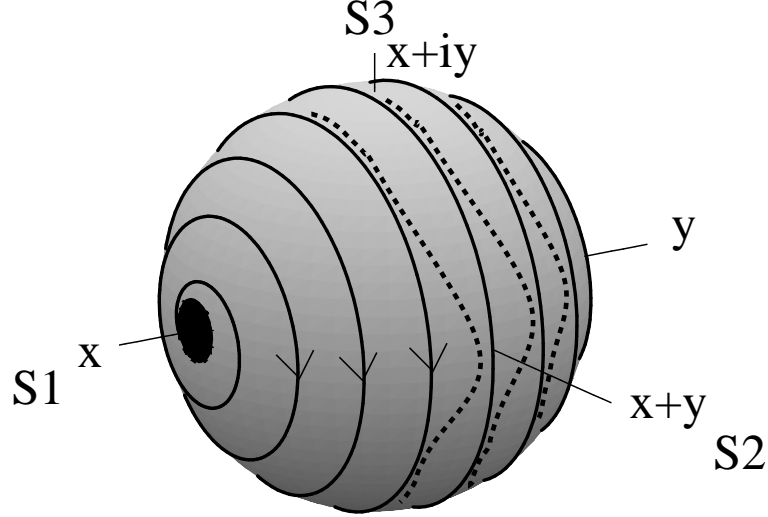

Figure 5.1: The drawn curves show a sketch of the cork-screw evolution of the Stokes parameters s_1, s_2 and s_3 on the Poincaré sphere during the polarization switch of a VCSEL. The dashed curves, which lie in the surface of the sphere, show the deformation of the circular orbits into a boomerang shape that occurs for VCSELs with very small, negative linear birefringence ω_{lin}.

Addressing now the s_2 and s_3 Stokes parameters, Eqs. (5.1b) and (5.1c) predict that these parameters oscillate during the switch with a frequency $\approx \omega_{\text{lin}}$ (in the case $\omega_{\text{lin}} \gg \omega_{\text{non}}, \gamma_{\text{non}}$), leading to a "cork-screw" trajectory of the polarization switch (Fig. 5.1). A more detailed analysis shows that the ω_{lin}-rotation around the s_1 axis is perturbed by a $2\omega_{\text{non}}$-rotation around the s_3 axis [see Eqs. (5.1a) and (5.1b)], which is clockwise on the northern hemisphere and counter-clockwise on the southern hemisphere, resulting in the following expression for the frequency ω of the cork-screw oscillation during the switch:

$$\omega(s_1) \approx \omega_{\text{lin}} + s_1 \omega_{\text{non}} \tag{5.3}$$

The birefringence beat frequency is thus "dressed" with the nonlinear birefringence, arising from the spin-dynamics. During the first part of the switch ($s_1 > 0$) the frequency ω is larger because the linear birefringence and nonlinear birefringence "cooperate", whereas they "cancel" during the second part of the switch ($s_1 < 0$).

5.3 Real-time observation of polarization switches

For the experiments we have used a batch of 80 proton-implanted $Al_xGa_{1-x}As$ VCSELs with a 1λ cavity operating at 850 nm [50]. From this batch we selected the devices (10) that exhibited a polarization switch within the fundamental transverse mode regime. We used a single-shot streak camera (Hamamatsu M1952, S25 photocathode) to measure the polarization in real-time during the switch. The light emitted by the VCSEL is projected on a specific Stokes parameter by a $\lambda/4$ and a $\lambda/2$-wave plate, and an optical Faraday isolator.
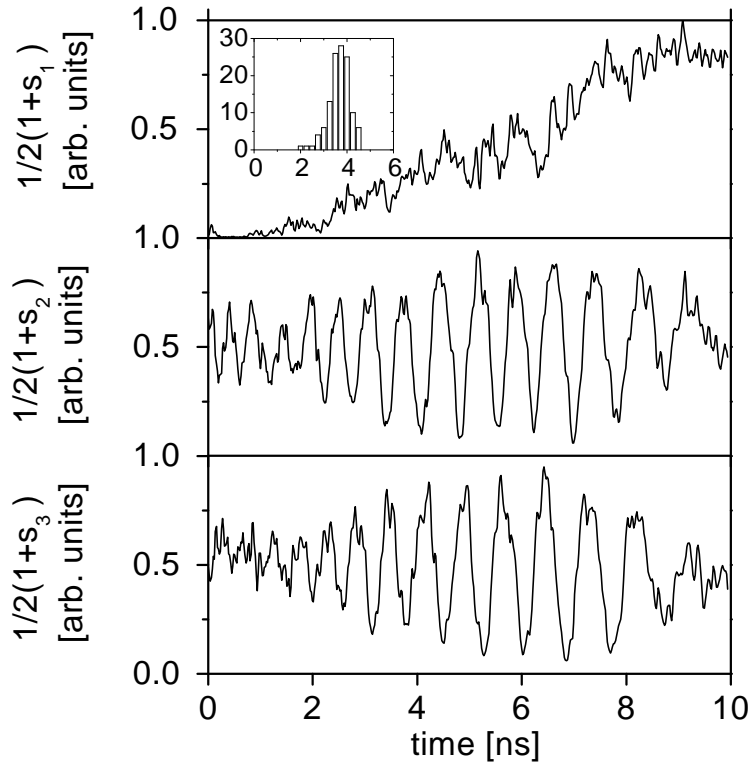
Figure 5.2: Time-resolved measurements of the polarization during the switch. Each box shows the intensity projection on one of the Stokes-parameters. The inset shows a distribution of transit times (ns), defined as the passage time from 25% to 75% in the $1/2(1+s_1(t))$ curve, obtained from 120 polarization switches of the same device.

We address now experimental results obtained from a typical VCSEL polarization switch within the range of fundamental transverse mode operation, the VCSEL polarization being bistable at the switch current [53]. Measured time traces of subsequent polarization switches are shown in Fig. 5.2, where each time the polarization is projected on one of the Stokes parameters. The results clearly demonstrate the predicted cork-screw motion on the Poincaré sphere, as the polarization projection on s_1 shows a gradual increase whereas the projections on s_2 and s_3 show a transient oscillation. Note that the oscillation frequency in Fig. 5.2 indeed decreases during the switch as predicted by Eq. (5.3). To check this quantitatively, we determined ω_{lin} and ω_{non} independently with polarization homodyne detection [50], where we found a value of 2.1 GHz and 0.55 GHz for ($\omega_{lin}/2\pi$) and ($\omega_{non}/2\pi$). This agrees with Fig. 5.2 and Eq. (5.3), as the frequency in the s_2/s_3 time-traces indeed varies between the sum and difference of the quoted values of ω_{lin} and ω_{non}.

The stochastic origin of the switches gives rise to a distribution of T_{tr} (see histogram in the inset of Fig. 5.2). The value of T_{tr} is determined from s_1 time traces by measuring the time interval [3] during which the intensity is between the 25% and 75% levels of the intensity after the switch (this criterion corresponds to $s_1 = +1/2 \rightarrow s_1 = -1/2$). On average no difference between uphill paths and downhill paths was observed, validating the "stochastic inversion symmetry". The mean value $\langle T_{tr} \rangle$ was found to be 3.7(3) ns. To compare this with Eq. (5.2), we measured γ_{non} with polarization homodyne detection [50] and determined D from linewidth measurements with a selfheterodyne fiber-delay setup [53], resulting in a value of $\gamma_{non} \simeq 1.1(2)$ ns^{-1} and $D \simeq 7(1)$ μs^{-1} for this VCSEL. According to Eq. (5.2), this gives a value of $\langle T_{tr} \rangle \simeq 2.8(5)$ ns, which is in reasonable agreement with the directly measured value, which is expected to be somewhat larger anyhow due to the non-parabolic form of the potential further away from the symmetry point.

Due to the stochastic nature of the problem, one must also expect events where the polarization makes a large excursion from its minimum in the potential (*x* or *y* polarized) but where the spontaneous emission noise is not strong enough to actually cross the barrier. A demonstration of such an event is shown in Fig. 5.3 (same laser as before), where the streak camera triggered on $\approx$ 45 % of the level corresponding to a complete switch. The s_1 time trace shows that there is no switch, whereas the s_2/s_3 time traces still oscillate, as expected. A closer inspection of the s_2/s_3 traces confirms that the polarization did not switch, because there

---

[3]To determine the transit time T_{tr} from s_1 time traces, like Fig. 5.2a, we filtered the sharpest spikes by coarse-grain averaging and took average values in the case of multiple crossings of the 25% and 75% lines.
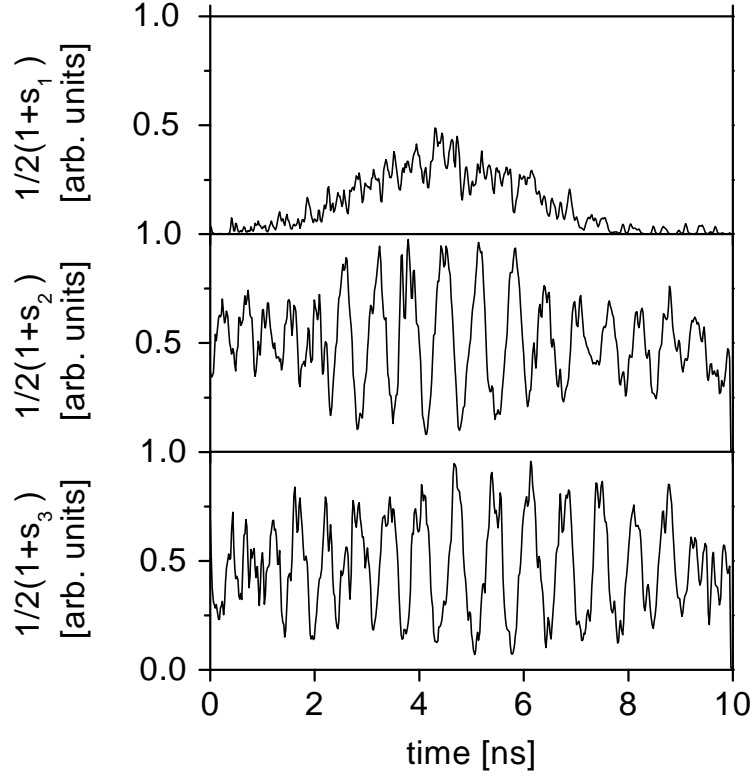
Figure 5.3: Time-resolved measurements of a very large polarization fluctuation, where the size of the fluctuation is about half (in fact: 45%) of that of a complete polarization switch.

is no observable change in the oscillation period before and after the transient; the polarization stays on one side of the Poincaré sphere, $s_1 > 0$, [see Eq. (5.3)]. Figure 5.3 thus demonstrates that polarization fluctuations and switching have a common basis; after a polarization fluctuation the polarizations spirals back to its steady state on the Poincaré equator.

When performing the measurements on different VCSELs, we generally found the same corkscrew-scenario as discussed above. However, theory [23,50] predicts that switches at small negative ω_{lin} have a different nature. In this case the nonlinear birefringence ω_{non} can compensate the linear birefringence ω_{lin} so that the lasing and nonlasing polarization mode overlap in the optical spectrum, giv-

ing rise to a different switching mechanism. When $\omega_{\mathrm{non}} \approx |\omega_{\mathrm{lin}}|$, the ω_{non}-rotation around the s_3 axis (being cw/ccw on the northern/southern hemisphere) has a dramatic effect on the ω_{lin}-rotation, *i.e.*, on the circular orbits around the s_1 axis. During the first part of this type of switch the deterministic orbits disappear effectively, whereas they appear during the second part, but heavily deformed into boomerang-shaped orbits (see the dashed curves in Fig. 5.1). These boomerang-shaped orbits should be visible as a "second harmonic" in the s_1 time trace as the bulges sketched in Fig. 5.1 also appear at the backside of the Poincaré sphere.
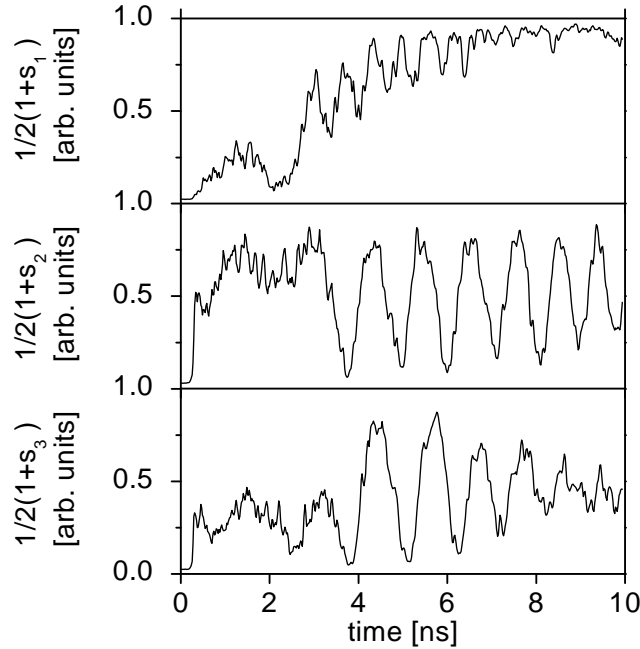

Figure 5.4: Time-resolved measurements of a polarization switching VCSEL with extremely small, negative linear birefringence ($|\omega_{\mathrm{lin}}/2\pi| \leq 0.5$ GHz). Note that for negative linear birefringence the frequency increases during the switch.

For experimental verification of this prediction we selected a rare VCSEL with very small birefringence $|\omega_{\mathrm{lin}}/2\pi| \leq 0.5$ GHz. Figure 5.4 shows the time traces of the Stokes parameters during the switch for this rare VCSEL. The first part of the s_2/s_3 traces shows no oscillation, confirming that ω_{lin} and ω_{non} roughly cancel, whereas in the last part an oscillation appears as ω_{lin} and ω_{non} now add up. The

deformation into boomerang orbits is demonstrated in the s_1 time trace of Fig. 5.4, which displays roughly double the frequency of the oscillations in the s_2/s_3 time traces.

5.4 Conclusion

Our work thus shows that the origin of a VCSEL polarization switch may be absorptive (Fig. 5.2) or dispersive (Fig. 5.4), as theoretically proposed [23]. We found experimentally that a dispersive switch has *two* conditions: a dispersive condition of small negative linear birefringence ω_{lin}, as outlined above, as well as an absorptive condition of small linear dichroism $\gamma_{\parallel}$. These two conditions are very rarely fulfilled: for practically all VCSELs $\omega_{\text{lin}} \gg \omega_{\text{non}}, \gamma_{\text{non}}$ and absorptive switching ($\gamma_{\parallel} \approx 0$) occurs.

In conclusion, we have addressed optical bistability in the transient regime by studying real-time polarization switching in VCSELs. The measurements, which are on a time-scale that is generally not included in a Kramers description, agree with theory [50,67].

Polarization loxodrome of a vertical-cavity semiconductor laser [1]

We present a theoretical analysis of the polarization dynamics of a vertical-cavity surface-emitting laser (VCSEL) with <u>either</u> linear anisotropies <u>or</u> nonlinear anisotropies. In both cases, we demonstrate that the polarization excursions follow a loxodrome spiral curve on the Poincaré sphere of the polarization.

6.1   Introduction

The semiconductor vertical-cavity surface-emitting laser (VCSEL) is a micro-cavity laser with a planar geometry. Although this construction has many benefits, for instance the integration of solitary lasers into two-dimensional arrays, a big disadvantage of the planar symmetry is that the polarization stability of practical devices is limited [13]. Polarization stability and polarization noise in VCSELs have been addressed extensively, using a range of techniques: stability analysis of the steady-state polarization [15,23,68,32,62,69]; calculation of two-time correlation functions [26,70]; measurements of polarization modal correlations [47,48,71,49,72,66,73,74]; and statistics of polarization switching [56,53].

Nevertheless, a transparent picture displaying the real-time evolution of polarization fluctuations is still missing. The reason for this is twofold: the theory is too complicated to allow analytical results, and the experiment is rather difficult because polarization fluctuations in VCSELs occur on relative fast time scales (typically nanoseconds [50]). Consequently, most studies are based on time or statistical averaging [15,23,68,32,62,69,26,70,47,48,71,49,72,66,73,74,56,53], so that the details of the actual polarization excursions are lost; if individual evolution paths are studied at all, this is usually restricted to a numerical treatment.

Our aim is to present an elucidating picture of polarization fluctuations in the time domain, by visualizing polarization excursions as analytical trajectories on

---

[1]M. B. Willemsen, M. P. van Exter, J. P. Woerdman, manuscript submitted for publication

the Poincaré sphere. For two relevant cases, we show that the polarization trajectory reduces to a loxodrome, *i.e.*, a spiral curve embedded on the surface of a 3D sphere; we derive expressions for the Stokes parameters of these polarization orbits on the Poincaré sphere. This study is a theoretical extension of our previous experimental and theoretical work on time-resolved polarization switching of VCSELs (see chapter 5 and ref. [75]).

We start with an introduction to loxodromes in Sec. 6.2. In Sec. 6.3 we briefly summarize the polarization properties of practical VCSELs. In subsection 6.3.1 we discuss the polarization loxodromes of VCSELs with only linear anisotropies, *i.e.*, symmetry-breaking due an almost cylindrical cavity. In subsection 6.3.2 we address VCSELs with only nonlinear anisotropies, *i.e.*, symmetry-breaking due to the quantum-well gain medium. We end with a summary and conclusions in Sec. 6.4.

6.2   Loxodrome

A loxodrome is a curve on the surface of a 3D sphere, say the earth, that spirals in a specific way from a fixed point towards the diametrically opposed point [76]. The specific property of a loxodrome spiral is that it intersects *all* great circles, that pass through these two opposite points, at a *constant* angle. Figure 6.1a shows an example of such a loxodrome, spiraling from the north pole to the south pole. For this north-south orientation of the loxodrome, the great circles that are cut at a constant angle are the meridians (see Fig. 6.1b). The consequence of intersecting all meridians at a constant angle is that near the poles the number of windings increases rapidly. In fact a loxodrome is a generalization of a logarithmic spiral in a flat 2D-plane, but now embedded on the surface of a 3D-sphere [76]. Note that a loxodrome is a fractal; it is "self-similar" in the sense that around the poles its shape reproduces itself on smaller and smaller length scales [77]. As an aside, this example shows that navigation on the earth at a constant compass course, *i.e.*, at a constant angle with respect to the local meridian, corresponds to traveling on a loxodrome.

It is straightforward to derive a mathematical expression for a loxodrome. Using spherical coordinates $(x,y,z)=(\cos\psi\sin\theta,\sin\psi\sin\theta,\cos\theta)$, with $\theta \in [0,\pi]$ and $\psi \in [0,2\pi]$, the infinitesimal length of a segment on the sphere is given by $d\sigma = \sqrt{d\theta^2 + \sin^2\theta d\psi^2}$. In order to profit fully from the spherical coordinates, it is easiest to choose the *z*-axis such that it coincidences with the direction of "propagation" or "flow" of the loxodrome, so that the angle θ gives approximately the azimuthal position of a winding on the axis of propagation and ψ is the (projected) angle in a plane perpendicular to the direction of flow. The criterion for the seg-
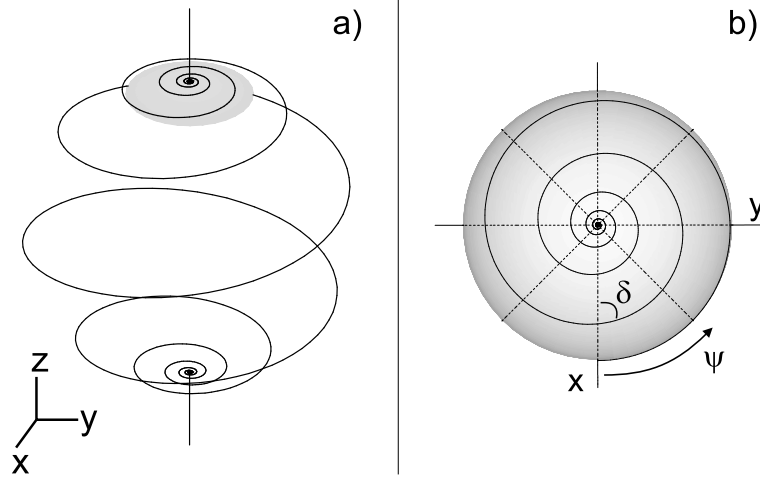
Figure 6.1: Loxodrome spiraling between the north pole and the south pole. Figure 6.1a shows a side view of the loxodrome, whereas Fig. 6.1b shows a top view from the north pole ($\theta = 0$). The dashed lines in Fig. 6.1b are meridians, which are intersected at a constant angle δ by the loxodrome. In this example we have chosen $\delta \approx 85°$.

ment $d\sigma$ to be loxodrome is that it locally cuts the segment $d\theta$ of the great circles at a constant angle δ (see Fig. 6.1b), leading to the condition

$$d\psi = -\frac{\tan\delta}{\sin\theta}d\theta. \tag{6.1}$$

Solving this equation gives the following explicit expression for the loxodrome

$$\psi = \tan(\delta)\tanh^{-1}(\cos\theta) + C, \tag{6.2}$$

where the constant C determines the starting point or angular orientation of the loxodrome. Integration of $d\sigma$ shows that the length L of a loxodrome segment, that spirals between two azimuthal angles θ_B and θ_A is finite and equal to

$$L = \frac{\theta_B - \theta_A}{\cos\delta}. \tag{6.3}$$

For $\delta = \pi/2$ (mod π), the loxodrome cuts the great circles perpendicular and reduces to a circle on the sphere with fixed azimuthal angle θ.

6.3   Polarization loxodromes

To visualize polarization excursions in VCSELs, we will use the Poincaré sphere. On the surface of this sphere, all polarization states can be represented; the poles correspond to right-and left-handed circularly-polarized light, in the equatorial plane the polarization is linear, and the points on the northern and southern hemispheres correspond to elliptical polarizations. On the Cartesian axes the Stokes parameters (s_1,s_2,s_3) are plotted, as

$$s_1 \equiv \cos(2\chi)\cos(2\phi) , \tag{6.4a}$$
$$s_2 \equiv \cos(2\chi)\sin(2\phi) , \tag{6.4b}$$
$$s_3 \equiv \sin(2\chi) , \tag{6.4c}$$

where the Poincaré angles $\phi \in [0,\pi]$ and $\chi \in [-\pi/4, \pi/4]$ correspond to the polarization angle and ellipticity, respectively. Note that these angles are related to the spherical angles of Sec. 6.2 via $\psi = 2\phi$ and $\theta = 2\chi + \pi/2$. The Stokes parameters are normalized according to $s_1^2 + s_2^2 + s_3^2 = 1$. This mapping of the polarization states onto the Poincaré sphere corresponds in magnetic resonance to the mapping of all possible spin-$\frac{1}{2}$ states onto the Bloch sphere.

Polarization fluctuations originate from the imperfect nature of the balance between, on the one hand, deterministic forces associated with intrinsic polarization preferences or anisotropies of the laser, which damp the fluctuations, and, on the other hand, a stochastic force associated with spontaneous emission noise [50]. The steady-state polarization, as determined by the anisotropies, corresponds to a stable point on the Poincaré sphere. However, due to inevitable spontaneous emission which is uniform on the Poincaré sphere, the polarization will always fluctuate. By plotting the deterministic forces of the anisotropies as flow lines on the Poincaré sphere one can understand in a quantitative way how the polarization escapes from, and is driven back to, its steady-state, via these flow lines.

In our previous theoretical and experimental work on time-resolved polarization switching in VCSELs [75] we showed that the polarization dynamics on the Poincaré sphere contains stochastic and deterministic aspects. Moreover, we demonstrated that for large polarization fluctuations far away from the stable point the deterministic evolution ($\equiv$ flow lines) rules, whereas for small polarization fluctuations the stochastic component dominates the polarization dynamics. In this paper, we will restrict ourselves to the deterministic component of the "polarization flow", which is valid if the polarization fluctuations are large; this can indeed easily occur in practical VCSELs [50].

For practical VCSELs, there are several different types of anisotropies [25]. Most important are the linear anisotropies, which model the symmetry breaking of the nominal cylindrical VCSEL cavity, due to for example the linear electro-optic effect [45] and mechanical strain [78]. The linear anisotropies consist of a dispersive and adsorptive part, linear birefringence and linear dichroism, respectively.

However, even for a perfect symmetric device the polarization diffusion will not be isotropic, as it will be affected by the nonlinear polarization preferences of the gain medium. The gain-medium of quantum-well VCSELs is described by the spin-flip model [15]. In this model the heavy-hole valence band and the conduction band of the quantum-well gain medium are approximated by four discrete spin-levels, which interact pair-wise each with one circular component of the optical field. This specific interaction scheme leads to polarization-dependent saturation, or nonlinear anisotropies. An important difference between the linear and nonlinear anisotropies in VCSELs is that the former discriminate between the linear x and y polarization, whereas the latter differentiate between circular polarizations and linear polarizations, irrespective of the linear polarization direction.

In the following subsections, we will discuss the polarization fluctuations of VCSELs for two relevant limits: VCSELs with *either* linear anisotropies *or* nonlinear anisotropies. VCSELs with only linear anisotropies are a fair description of practical devices, since in these devices linear anisotropies have been found to be much larger than nonlinear anisotropies [50,24]. On the other hand, VCSELs with only nonlinear anisotropies, having an isotropic cavity, are an intriguing fundamental limit, since in these lasers the polarization dynamics is fully determined by the spin dynamics of the quantum well gain medium.

6.3.1 Linear polarization loxodrome

Experimentally, it has been demonstrated that linear anisotropies generally dominate over nonlinear anisotropies in VCSELs [50,24]. Considering *only* linear anisotropies, the deterministic evolution equations for the Stokes parameters (see Sec. 2.6 and ref. [50]) are given by

$$\frac{ds_1}{dt} = \gamma_{\text{lin}}\left(s_2^2 + s_3^2\right), \tag{6.5a}$$

$$\frac{ds_2}{dt} = -\gamma_{\text{lin}}s_1 s_2 - \omega_{\text{lin}}s_3, \tag{6.5b}$$

$$\frac{ds_3}{dt} = -\gamma_{\text{lin}}s_1 s_3 + \omega_{\text{lin}}s_2, \tag{6.5c}$$

where ω_{lin} is the linear birefringence and γ_{lin} the linear dichroism, which is assumed to have the same *xy* orientation. The steady-state solutions Eqs. (6.5a-c) are $s_1 = 1, -1$, corresponding to the linear *x* and *y* polarization, respectively. For the considered case of $\gamma_{lin} > 0$ and $\omega_{lin} < 0$ the *x* polarization is stable and lasing with the lowest eigenfrequency, whereas the orthogonal *y* polarization is the unstable nonlasing mode.

Figure 6.2 shows a side view of the Poincaré sphere with the flow lines of the linear anisotropies. The curved arrows on the circles correspond to the linear birefringence ω_{lin}, leading to a rotation of the polarization around the steady-state. The arrows pointing radially inwards correspond to the linear dichroism γ_{lin}, driving the polarization directly back to its steady-state.
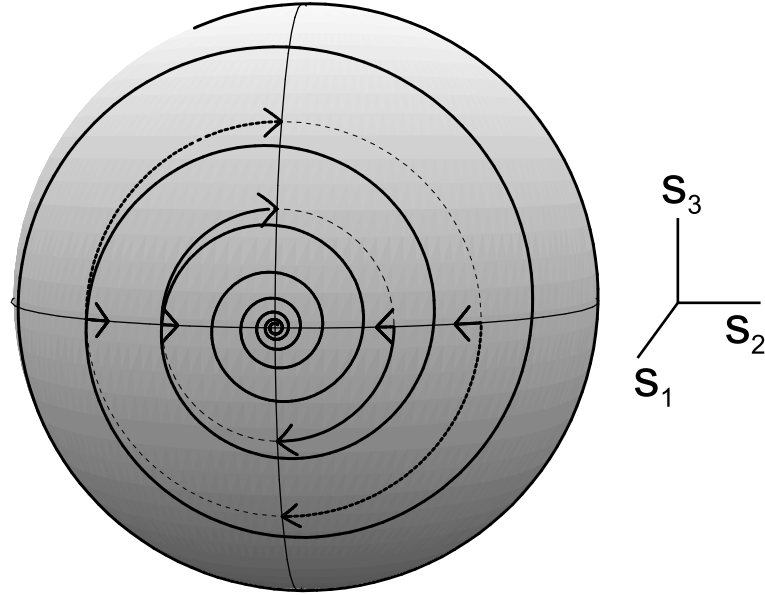
Figure 6.2: Polarization loxodrome of a VCSEL with only linear anisotropies. The flow lines due to the linear birefringence ω_{lin} are on the dashed circles, whereas the flow lines due to the linear dichroism γ_{lin} are pointing inwards. The polarization evolution correspond to a loxodrome (spiral curve), spiraling between the stable lasing polarization and the orthogonal nonlasing polarization, diametrically opposed on the backside of the Poincaré sphere. In this figure we have chosen $\omega_{lin}/\gamma_{lin} = 10$.

Suppose now that the polarization is away from its steady-state point, for instance due to a strong spontaneous emission event. The combined flow line pat-

tern of linear birefringence and linear dichroism, being spiral-like and pointing inwards, will drive the polarization back to the steady state. To demonstrate that the overall flow defined by Eqs. (6.5a-c) indeed moves along loxodromes, we will transform these equations to spherical coordinates θ and ψ as defined with respect to the s_1-axis. Substitution of $(s_1,s_2,s_3) = (\cos\theta, \sin\theta\cos\psi, \sin\theta\sin\psi)$ yields

$$\frac{d\psi}{dt} = \omega_{\text{lin}} , \tag{6.6a}$$

$$\frac{d\theta}{dt} = -\gamma_{\text{lin}}\sin\theta , \tag{6.6b}$$

which are directly recognizable as the defining equations of a loxodrome that makes a constant angle $\delta_{\text{lin}} = \arctan(\omega_{\text{lin}}/\gamma_{\text{lin}})$ with the great circles through the eigenpolarizations $s_1 = \pm 1$. Consequently, the polarization evolution is along loxodrome trajectories on the Poincaré sphere, as shown by the spiral curve in Fig. 6.2. For VCSELs, typical values measured for the ratio $\omega_{\text{lin}}/\gamma_{\text{lin}}$ are between 10 and 100, so that the angle δ_{lin} is only slightly smaller than $90°$.

Equations (6.5a-c) can be solved analytically, using the normalization condition $s_1^2 + s_2^2 + s_3^2 = 1$, to yield the following polarization trajectories for the Stokes parameters

$$s_1(t) = \tanh(\gamma_{\text{lin}}t + C_1) , \tag{6.7a}$$

$$s_2(t) = \frac{1}{\cosh(\gamma_{\text{lin}}t + C_1)}\cos(\omega_{\text{lin}}t + \psi_0) , \tag{6.7b}$$

$$s_3(t) = \frac{1}{\cosh(\gamma_{\text{lin}}t + C_1)}\sin(\omega_{\text{lin}}t + \psi_0) , \tag{6.7c}$$

where $\psi_0 \in [0, 2\pi]$ and $C_1 = \tanh^{-1}[\cos(\theta_0)]$, with $\theta_0 \in [0, \pi]$, are the starting conditions at $t = 0$. The angle θ_0 is the azimuthal position of the starting winding, whereas the angle ψ_0 refers to the position in the plane perpendicular to the s_1-axis. Equations (6.7a-c) quantitatively show how, via a simple combination of hyperbolic and geometric functions, the polarization rotates back to the lasing eigenstate $s_1 = 1$. For large excursions, each of these "returning-to-the-lasing-mode" paths [Eqs. (6.7a-c)] has a mirror-imaged "escaping-from-the-lasing-mode" path with an equal probability due to the "stochastic-inversion" symmetry [75].

6.3.2   Nonlinear polarization loxodrome

In this section, we will discuss the polarization fluctuations of a VCSEL with a "perfect" cylindrical symmetry, which is interesting from a fundamental point of view. Although we assume now that the VCSEL-cavity has a perfect cylindrical symmetry, the polarization diffusion will not be isotropic, but will be affected by the nonlinear anisotropies of the quantum well gain medium. We will show that the polarization trajectories can be described by *two* half-loxodromes. In practice, it will be of course difficult to realize such a symmetric cavity. Possible schemes of realization are (*i*) compensation of intrinsic of asymmetries in ordinary devices by applying strain [78], and/or (*ii*) growing VCSELs on misoriented substrates that have a higher in-plane degree of symmetry, for example VCSELs on [111]-substrates [79].

To incorporate the polarization-dependent saturation of the gain medium, the spin-flip model [15] was used as a starting point. As a next step the four discrete spin levels, that interact as pairs, were rewritten as an average and a spin-difference inversion. Since these spin reservoirs are strongly coupled [50], the spin-difference inversion can be eliminated adiabatically. This elimination procedure results in a description of the polarization-dependent saturation, due to the gain-medium, by two nonlinear anisotropies. The deterministic rate-equations for the Stokes parameters (see Sec. 2.6 and ref. [50]) are now given by

$$\frac{ds_1}{dt} = 2\gamma_{\mathrm{non}}s_1 s_3^2 + 2\omega_{\mathrm{non}}s_2 s_3 \,, \tag{6.8a}$$

$$\frac{ds_2}{dt} = 2\gamma_{\mathrm{non}}s_2 s_3^2 - 2\omega_{\mathrm{non}}s_1 s_3 \,, \tag{6.8b}$$

$$\frac{ds_3}{dt} = -2\gamma_{\mathrm{non}}s_3\left(s_1^2 + s_2^2\right) \,, \tag{6.8c}$$

where ω_{non} is the nonlinear birefringence and γ_{non} the nonlinear dichroism. The nonlinear anisotropies are given by $\omega_{\mathrm{non}} = \alpha(\kappa/\Gamma)\mu$ and $\gamma_{\mathrm{non}} = (\kappa/\Gamma)\mu$, where κ is the cavity loss rate, Γ the normalized spin-flip rate, $\mu + 1$ the pump rate normalized to threshold, and α the linewidth enhancement factor [50].

A linear stability analysis of Eqs. (6.8a-c) shows that we do *not* deal with a single stable polarization, but that the set of all linear polarizations is stable and favored as compared to the elliptically and circularly polarized states. The preferred states are thus all linear polarizations $s_1^2 + s_2^2 = 1$, whereas the circular polarizations $s_3 = -1, 1$ are the unstable eigenpolarizations.

Figure 6.3 shows the Poincaré sphere with the flow lines of the nonlinear anisotropies. The clockwise and counter-clockwise rotating arrows on the
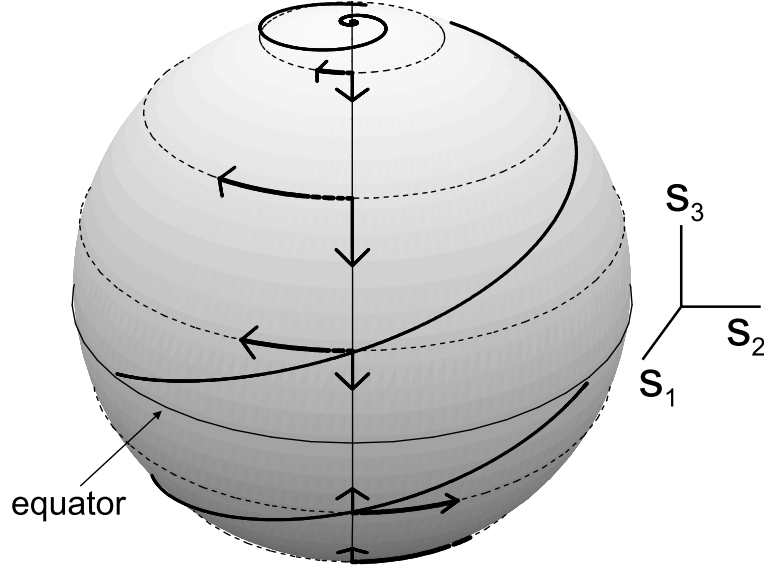
Figure 6.3: Polarization loxodrome of a VCSEL with only nonlinear anisotropies. The flow lines due to the nonlinear birefringence $\omega_{non} = \alpha\gamma_{non}$ are on the dashed circles, whereas the flow lines due to the nonlinear dichroism γ_{non} are pointing to the equatorial plane. The polarization fluctuations correspond to two disjoint loxodromes on either hemisphere, spiraling between the pole (circular polarization) and the equatorial plane (all linear polarizations). In this figure we have chosen $\alpha = 3$.

northern and southern hemispheres result from the nonlinear birefringence ω_{non}. Whereas the arrows pointing from the north and south pole to the equatorial plane result from the nonlinear dichroism γ_{non}.

The great circles spanned by the eigenstates, *i.e.*, passing through the eigenstates, are the meridians. The flow lines of the nonlinear dichroism γ_{non} overlap with the meridians, and the flow lines of the nonlinear birefringence ω_{non} are always perpendicular to the meridians. The combined flow line pattern of γ_{non} and ω_{non} always cuts the meridians at a constant angle. A transformation of Eqs. (6.8a-c) to the Poincaré angles defined in Eqs. (6.4a-c) yields

$$\frac{d\phi}{dt} = -\omega_{non}\sin 2\chi , \tag{6.9a}$$

$$\frac{d\chi}{dt} = -\gamma_{non}\sin 2\chi \cos 2\chi , \tag{6.9b}$$

which is the definition of a loxodrome, spiraling with a constant angle $\delta_{\text{non}} = \omega_{\text{non}}/\gamma_{\text{non}} = \alpha$. The corresponding polarization excursions will thus again be loxodromes.

However, besides the trivial difference that the direction of flow in the nonlinear case is now along the s_3-axis instead of the s_1-axis, there are some important distinctions with the linear case. Comparison of both sets of rate-equations [Eqs. (6.5a-c) and Eqs. (6.8a-c)] shows that, after permutation of the Stokes indices so that Eq. (6.5a) corresponds to Eq. (6.8c), the deterministic terms at the rhs in Eqs. (6.8a-c) of the nonlinear anisotropies are multiplied with an extra s_3-factor. The same multiplication with $s_3 \equiv \sin 2\chi$ shows up when we compare the angular rate-equations in case of the nonlinear anisotropies [Eqs. (6.9a-b)] to those for the linear anisotropies [Eqs. (6.6a-b)]. Note that the $\sin\theta$ term in Eq. (6.6b) corresponds to the $\cos 2\chi$ term in Eq. (6.9b), as $\theta = 2\chi + \pi/2$.

This multiplication introduces a nonlinearity, which leads to a modulation of the flow lines with an effective $\sin(4\chi)$-amplitude. The nonlinear anisotropies are strongest at $2\chi = \pm\pi/4$ and zero on the poles and in the equatorial plane. The first effect of this modulation is that the nonlinear anisotropies have an opposite sign on the northern ($\chi > 0$) and southern ($\chi < 0$) hemisphere, resulting in two disconnected counter-rotating loxodromes on either hemisphere. The second effect of this modulation is a variation in the propagation speed on the loxodrome. Note that, despite the nonlinearity, the angle of the combined flow line pattern of ω_{non} and γ_{non} with respect to the meridians is constant, and determined only by the α-factor.

Direct integration of Eqs. (6.8a-c), again using the normalization condition $s_1^2 + s_2^2 + s_3^2 = 1$, yields the following expressions for polarization trajectories

$$s_1(t) \quad = \quad \sqrt{\frac{1}{2}[1 + \tanh(2\gamma_{\text{non}}t) + C]} \cos[\alpha \sinh^{-1}(e^{-2\gamma_{\text{non}}t})] \,, \qquad (6.10a)$$

$$s_2(t) \quad = \quad \pm\sqrt{\frac{1}{2}[1 + \tanh(2\gamma_{\text{non}}t) + C]} \sin[\alpha \sinh^{-1}[e^{-2\gamma_{\text{non}}t}]] \,, \qquad (6.10b)$$

$$s_3(t) \quad = \quad \pm\sqrt{\frac{1}{2}[1 - \tanh(2\gamma_{\text{non}}t)]} \,, \qquad (6.10c)$$

where the time axis is chosen such that $2\chi = \pm\pi/4$ at $t = 0$, where the constant C determines the starting position as projected onto the s_1-s_2 plane, and where the $\pm$-sign refers to the loxodrome on the northern and southern hemisphere, respectively. As the propagation speed on the half-loxodromes approaches zero at the equator, the polarization takes infinitely long to reach the equator, keeping a con-

stant angle α.

6.4   Conclusion

In conclusion, we have introduced a transparent time-domain description of the polarization dynamics in VCSELs, by mapping polarization excursions as trajectories on the Poincaré sphere. For two relevant cases, (*i*) a "practical"VCSEL with dominant linear anisotropies and (*ii*) an "ideal" symmetric VCSEL with dominant nonlinear anisotropies, we have shown that these polarization trajectories are loxodromes embedded on the surface of the 3D Poincaré sphere. Specifically, for a "practical"VCSEL, the loxodrome spirals between the linear lasing polarization and the orthogonal nonlasing polarization diametrically opposed to it on the Poincaré sphere. For the "ideal" symmetric VCSEL, there are two disjoint loxodromes, each spiraling on one of the hemispheres between the circular polarization on the pole and the linear polarizations on the equator of the Poincaré sphere. If both linear and nonlinear anisotropies are important the path on the Poincaré sphere does not reduce to a loxodrome [50,75].

Polarization-resolved linewidth-power product of a vertical-cavity semiconductor laser [1]

We have studied the linewidth around threshold of the lasing and nonlasing polarization mode (x and y) in a TEM$_{00}$ oxide-confined vertical-cavity semiconductor laser (VCSEL). We experimentally demonstrate: (i) that the nonlasing mode shows surprising behavior when the lasing mode passes through threshold, and (ii) that the polarization fluctuations in a VCSEL are limited by the same quantum noise that sets its finite Schawlow-Townes linewidth.

7.1   Introduction

The vertical-cavity semiconductor laser (VCSEL) is not a true single-mode laser, as typically 1% of the emitted power is present as polarization noise in a weak nonlasing mode orthogonally polarized to the lasing mode [43]. The strong polarization noise in VCSELs is a limiting factor for many applications, since any polarization dependence of a detection scheme converts polarization noise into intensity noise, leading to a large degradation of the signal-to-noise ratio. As we will show here, insight in the polarization behavior can be obtained by studying both the dynamics of the lasing mode, which exhibits phase fluctuations [80,81], as well as that of the nonlasing mode, which contains the polarization fluctuations. In this chapter, we quantitatively compare phase and polarization fluctuations by performing polarization-resolved linewidth measurements on a TEM$_{00}$ VCSEL below and above threshold. These linewidth measurements show that polarization fluctuations occur on a nanosecond time scale and that the nonlasing mode is incoherent or thermal, *i.e.*, the fluctuations in this mode are equal to its average power, which explains that even 1% orthogonal polarized emission can be a serious limitation for applications. Finally we demonstrate that the modal purity

is limited by the same quantum noise that sets the finite Schawlow-Townes (ST) linewidth.

7.2   Linewidth

For a laser below threshold both the amplitude and phase fluctuate, so that the linewidth below threshold is twice the "standard" ST-linewidth ($\Delta\nu_{ST}$),

$$\Delta\nu^{\text{below}} = 2\Delta\nu_{ST} = 2\Big(\frac{h\nu\eta^{\text{ext}}\Gamma_c^2}{4\pi P}\Big), \tag{7.1}$$

where Γ_c is the cavity loss rate, *i.e.*, the sum of the mirror loss rate Γ_m and the internal loss rate Γ_i, $h\nu$ the photon energy, $\eta^{\text{ext}} = \Gamma_m/\Gamma_c$ the external quantum efficiency, and P the output power. We introduce the normalized injection current $M \equiv i/i_{\text{thr}}$, where i is the injection current and i_{thr} the threshold current. Above threshold ($M > 1$) the ST-linewidth in semiconductor lasers is modified due to the linewidth enhancement factor α,

$$\Delta\nu^{\text{above}} = (1 + \alpha^2)\Delta\nu_{ST} = (1 + \alpha^2)\frac{h\nu\eta^{\text{ext}}\Gamma_c^2}{4\pi P}. \tag{7.2}$$

From Eqs. (7.1) and (7.2) follows that the prefactor of the linewidth-power product of the lasing mode changes from 2 to $1 + \alpha^2$ by passing through threshold. The nonlasing polarization mode is by definition always below threshold, so that Eq. (7.1) is expected to hold both below and above threshold of the lasing mode. However, we will see that the nonlasing mode still exhibits peculiar threshold behavior.

7.3   Experimental results

For the experiments we used oxide-confined VCSELs emitting around 830 nm. The VCSEL output beam was passed through a $\lambda/4$ wave plate, a $\lambda/2$ wave plate, and an optical Faraday isolator (60 dB) in order to prevent optical feedback and to select either of the two polarization modes. For spectral diagnostics we used mostly a Fabry-Pérot interferometer (FP) with an adjustable free spectral range (FSR) between 5 and 150 GHz.

7.3.1 Lasing mode

First we discuss the threshold behavior and linewidth of the lasing polarization mode. Curve (a) in Fig. 7.1 shows the power of this mode, selected with the FP, as a function of M. The threshold current i_{thr} was found to be 0.43 mA and the VCSEL still emitted in the fundamental transverse mode up to currents of 2.0 mA.
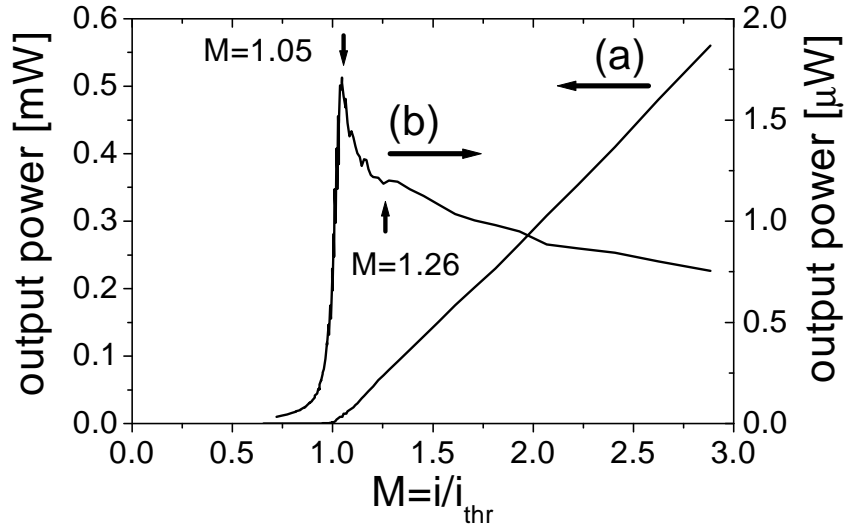

Figure 7.1: Output-input curve of the lasing (a) and the nonlasing (b) polarization mode, as measured with the Fabry-Pérot interferometer.

Figure 7.2 shows the linewidth [full width at half maximum (FWHM)] of the lasing mode below and above threshold. Please note the high quality of the data, which run over four orders of magnitude in both the horizontal and vertical scale. The linewidth below and around threshold was determined from the Lorentzian peak in the optical spectrum, as measured with the FP with several convenient FSRs, resulting in errors less than 5%. The linewidth below threshold was found to be proportional to the inverse output power, and the corresponding ST-fit (dashed curve in Fig. 7.2) yields a value of 1.6(2) MHz·mW for the linewidth-power product below threshold.

Higher above threshold ($M > 1.2$) the linewidth was measured with a self-heterodyne setup (kHz-resolution), where one path contained a 650-MHz acoustic optic modulator while the other path contained either a fiber-delay of 200 m or a free-space delay of 2 m, *i.e.*, a super and sub-coherence delay, respectively. Generally, we found a good agreement between the linewidth determined from the

long (fiber) and short (free-space) delay [2], as demonstrated by the triangles and squares in Fig. 7.2. After passing through the threshold transition from below, the linewidth was again found to be proportional to the inverse output power, and we extracted a value of 4.6(3) MHz·mW for the linewidth-power product (dotted curve in Fig. 7.2). The α-factor can be determined [82] from the ratio of the linewidth-power products above and below threshold, which is $(1 + \alpha^2)/2$ according to Eqs. (7.1) and (7.2), yielding a value of α=2.2(3).
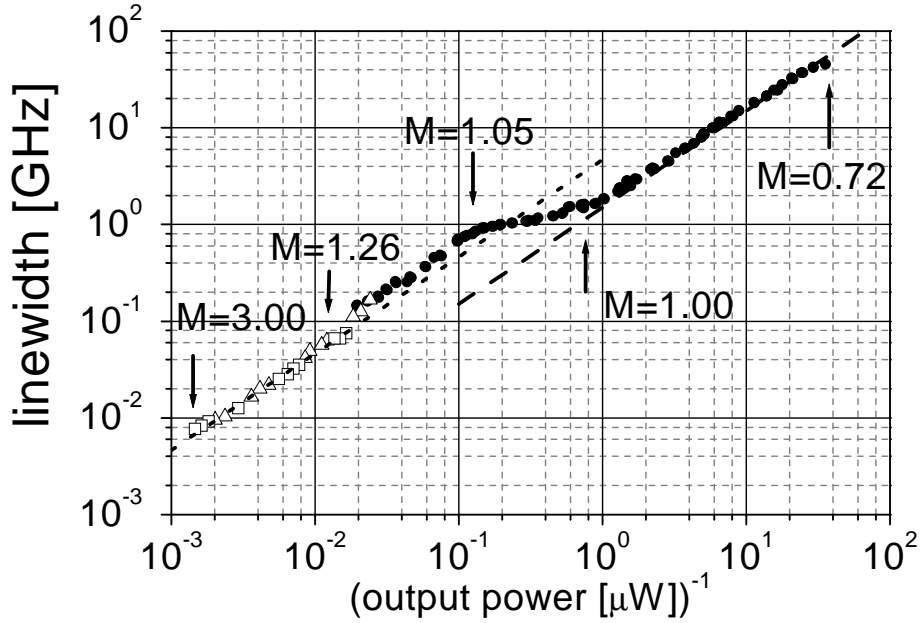
Figure 7.2: Linewidth (FWHM) of the lasing polarization mode below and above threshold as a function of the inverse power. The measurements around and below threshold were done with the Fabry-Pérot interferometer (solid circles), whereas higher above threshold we used a self-heterodyne technique with a super- and sub-coherence delay, triangles and squares, respectively.

The cavity loss rate can be determined from the linewidth-power product below threshold in combination with the measured slope in the input-output curve (a) in Fig. 7.1; the latter slope corresponds to a quantum efficiency of $\eta^{\text{eff}} = \eta^{\text{int}}\eta^{\text{ext}} = 0.46$. If we assume 100% internal efficiency ($\eta^{\text{int}} = 1.0$) and insert $\eta^{\text{ext}} = 0.46$

---

[2]Using a self-heterodyne setup we are also sensitive to optical frequency fluctuations during the delay time. This was a problem for measurements with the longer fiber-delay high above threshold, where the linewidth is narrow. In this case we determined the linewidth by extracting the Lorentzian component out of a noise-spectrum, with a Voigt-like shape.

in Eq. (7.1) we find $\Gamma_c = 3.0 \times 10^{11} s^{-1}$. If we assume the other extreme of low internal efficiency $\eta^{\text{int}} = 0.46$ we get $\Gamma_c = 2.0 \times 10^{11} s^{-1}$. An alternative way to determine Γ_c is from the relaxation oscillations (not shown). Here we find $\Gamma_c = 2.0(5) \times 10^{11} s^{-1}$, which is in reasonable agreement with the latter value and suggests that η^{int} is considerably smaller than 1; this has been found previously for proton-implanted VCSELs [83].

7.3.2   Nonlasing mode

Figure 7.1 also shows the input-output curve (b) of the nonlasing polarization mode, selected with the FP. One can distinguish three regimes: *(i)* below threshold, *(ii)* around threshold, where the intensity in the nonlasing mode increases rapidly, peaks at $M = 1.05$, and drops fast from $M = 1.05$ to $M = 1.26$, followed by *(iii)* a slower decrease in power for $M > 1.26$. Regime *(ii)*, which might be called anomalous spontaneous emission is rather intriguing, as a corresponding effect shows up in the linewidth of the nonlasing mode.
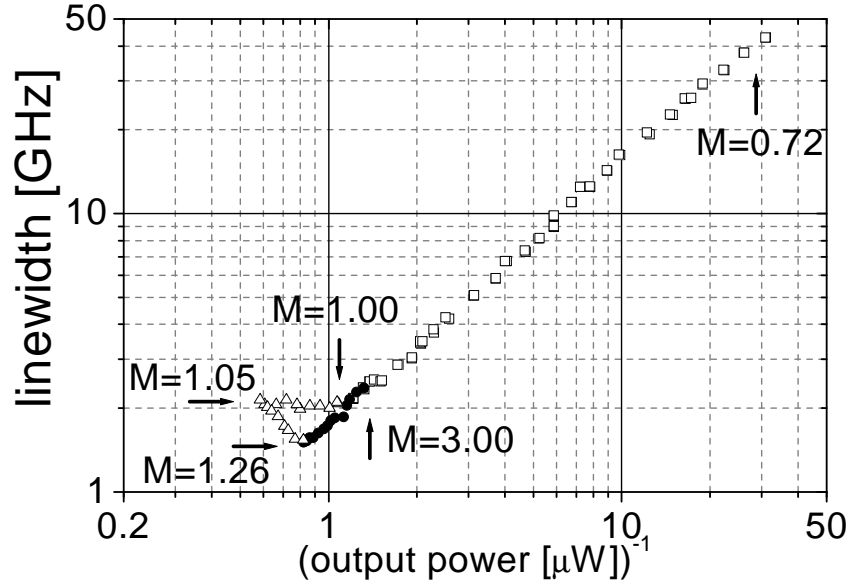

Figure 7.3: Linewidth (FWHM) of the nonlasing polarization mode as a function of its inverse power, measured with the Fabry-Pérot interferometer. The squares, triangles, and solid circles correspond to $0.72 < M < 1.00$, $1.00 < M < 1.26$, and $1.26 < M < 3.00$ respectively. The linewidth-power product for $M > 1.26$ is the same as below threshold ($M < 1.0$).

The linewidth of the nonlasing mode as a function of its inverse output power is shown in Fig. 7.3. The linewidth below threshold ($M < 1$, squares) was found to be proportional to the inverse power, with a linewidth-power product of 1.6(2) MHz·mW, which is, as expected, exactly the same as that of the lasing mode below threshold. Above threshold ($1.26 < M < 3.0$, solid circles) the linewidth of the nonlasing mode was also found to be proportional to the inverse output power, with a linewidth-power product of 1.7(2) MHz·mW. As this is the same as that for the polarization modes below threshold this demonstrates the incoherent or thermal nature of the nonlasing mode. As for $M > 1.26$ the power in the nonlasing mode decreased (Fig. 7.1), the linewidth follows the sub-threshold curve in the opposite direction as a function of M (Fig. 7.3). From the measured linewidths of typically a few GHz follows that polarization fluctuations occur on a nanosecond time scale. The fact that we find the same value for the linewidth power product for the nonlasing polarization mode as for the lasing mode below threshold demonstrates that the polarization fluctuations in a TEM$_{00}$ VCSEL are limited by the same quantum noise that sets its finite ST-linewidth.

Surprisingly, however, we observed that around threshold the linewidth of the nonlasing mode tries to follow the linewidth of the lasing mode, resulting in a similar plateau from M=1.00 to M=1.05 (triangles in Fig. 7.3, compared to Fig. 7.2). For drive currents higher above threshold ($M \geq 1.05$) the linewidth decreased and finally approached the below-threshold curve at M=1.26. This anomaly in the linewidth from M=1.00 to M=1.26 is a clear signature of the lasing threshold being visible in the orthogonally polarized nonlasing mode.

An explanation for this anomaly are the (carrier-induced) refractive index fluctuations, which give a contribution $\alpha^2 \Delta\nu_{ST}$ to the linewidth of the lasing mode above threshold and which disappear below threshold, thus peaking around threshold[3]. These index fluctuations will give the same absolute contribution to the linewidth of the nonlasing mode. They will therefore only affect the linewidth of the nonlasing mode significantly slightly above threshold ($1 < M < 1.26$), where the contribution $\alpha^2 \Delta\nu_{ST}$ from the lasing mode cannot be neglected as compared to the linewidth of the nonlasing mode (compare Figs. 7.2 and 7.3).

7.3.3 Modal impurity

We have also verified that the polarization modal impurity or modal ratio (R) of a VCSEL, being defined as the ratio of the power in the nonlasing mode (P_{non}) and lasing mode (P_{lasing}), is limited by the same quantum noise that sets the ST-

---

[3]A closer inspection of Fig. 7.2 shows that the linewidth of the lasing mode also exhibits anomalous behavior, as for M=1.0 to 1.26 it is slightly above the ST-value.

linewidth. For a VCSEL operating above threshold, it has been derived theoretically (see Sec. 2.6 and ref. [50]) that (for $D \ll \gamma_0$)

$$R = \frac{P_{\text{non}}}{P_{\text{lasing}}} = \frac{D}{\gamma_0}, \tag{7.3}$$

where γ_0 is the dichroism, or the difference in gain between the polarization modes, and D the phase diffusion coefficient ($D = 2\pi\Delta\nu_{\text{ST}}$). Figure 7.4 shows the modal impurity as a function of M, determined either directly from the input-output curves of Fig. 7.1 or from a calculation based on Eq. (7.3). In the latter case we determined D from the measured product of $(D/2\pi).P_{\text{out}}=0.8$ MHz.mW (see above), and the measured total output power. The dichroism γ_0 was determined, as a function of laser current, from the difference in width (HWHM) of the polarization modes in the optical spectrum. The good agreement demonstrates that the modal purity of a VCSEL, given a certain dichroism γ_0, is indeed limited by the inevitable spontaneous emission noise. Far below threshold the two Lorentzian shaped polarization modes had almost the same (large) width, resulting in a modal impurity that approaches 1 (see Fig. 7.4).
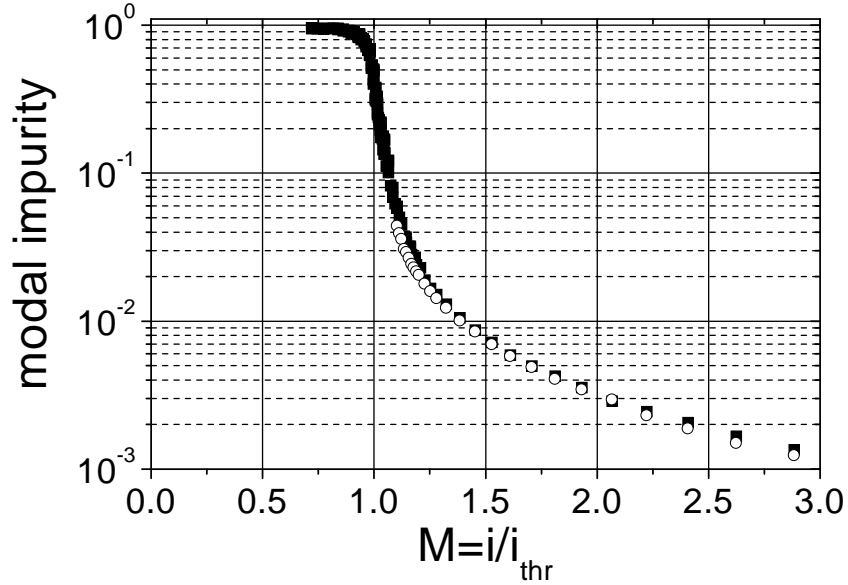

Figure 7.4: Modal impurity R vs M. The solid squares are determined from the input-output curves in Fig. 1, and the open circles above threshold ($M > 1.1$) are based upon Eq. (7.3).

7.4 Conclusion

In conclusion, polarization-resolved linewidth measurements show that not only the lasing mode but also the nonlasing polarization mode shows clear threshold behavior. The linewidth-power product of the lasing mode changes relatively from 2 to $1 + \alpha^2$ by passing through threshold. For the nonlasing polarization mode the linewidth-power product below and above threshold was found to be the same, demonstrating that polarization fluctuations are thermal-like. However, around threshold an anomaly in the linewidth showed up, due to (carrier-induced) refractive index fluctuations.

Self-pulsations in vertical-cavity semiconductor lasers [1]

We report the observation of strong self-pulsations in oxide-confined vertical-cavity surface-emitting lasers. From optical spectra and intensity noise spectra, we deduce that the pulses are strongly chirped.

8.1 Introduction

Self-pulsations in semiconductor edge-emitting lasers are well known; they can occur in a certain current range just above threshold. These self-pulsations can be seen as anomalously strong relaxation oscillations, and they transform into conventional relaxation oscillations at higher laser currents [84–86]. For applications of semiconductor lasers, like reading out optical-storage disks, self-pulsations play an important role, as lasers that exhibit self-pulsations are far less sensitive to optical feedback [86,33,87]. For vertical-cavity surface-emitting lasers (VCSELs) only short-pulsed emission at kHz repetition rates has been reported [88].

In this chapter, we report self-pulsations in VCSELs resulting from anomalously strong relaxation oscillations. We have observed this phenomenon most prominently in small oxide-confined VCSELs [89], and also in optically pumped VCSELs [90] and proton-implanted VCSELs [16]. In particular, we show that these self-pulsations are strongly chirped.

Already for edge emitters several physical explanations have been given for self-pulsations, being based on nonlinearities such as saturable absorption [84–86] or intensity-dependent waveguiding, as in Kerr-mode locking [91–93]. As it is difficult to discriminate between these models, in this chapter we focus on experimental results.

8.2   Spectral analysis of self-pulsations

The VCSELs that we have used are oxidized devices with three InGaAs quantum wells operating at 962 nm. The oxide is 25 nm thick and centered at a node of the optical field close to the active layer. The light emitted by the VCSEL was passed through a $\lambda/4$ and $\lambda/2$ waveplate in combination with a Faraday isolator ($\sim$ 60 dB) to select the lasing polarization mode and to prevent optical feedback. Figure 8.1 shows the output-input curve of a typical VCSEL, where the threshold current was 0.81 mA and higher-order transverse modes started lasing above 2.0 mA. Note that the output-input curve is superlinear as a function of current. We will show that one can distinguish, based upon the spectral width, four regimes within fundamental transverse-mode operation: (I) below threshold, (II) around threshold, (III) moderately above threshold, and (IV) relatively high above threshold. The width [full width at half maximum (FWHM)] of the optical spectrum as function of laser current is also shown in Fig. 8.1. These optical spectra were measured with a home-built Fabry-Pérot interferometer with a free spectral range (FSR) that can be adjusted between 5 and 150 GHz. Each width, as plotted in Fig. 8.1, was determined from different measurements with convenient FSRs, resulting in an error in the widths of less than 5%. Moreover, the measurements for settings with very broad spectra were checked with a grating-based spectrometer (resolution 10 GHz), whereas the small linewidths for higher drive currents were verified with a self-heterodyne fiber delay setup (resolution kHz). The most intriguing is regime (III), where anomalous spectral broadening occurs and where the optical spectrum is about a thousand times wider than typical VCSEL linewidths[2].

The optical spectra, as measured with the Fabry-Pérot interferometer, are shown in detail in Fig. 8.2. The spectra were taken at currents of i=0.82 mA, i=1.26 mA, and i=1.53 mA, respectively. Below threshold we observe a very broad Lorentzian-shaped spectrum, with typical widths of 5-20 GHz (not shown). Increasing the laser current toward threshold, the linewidth narrows rapidly to $\approx$ 1.5 GHz around threshold. An optical spectrum in this regime (II) is shown as Fig. 8.2a. For currents higher above threshold the width increases again [regime (III) in Fig. 8.1]. Besides this anomalous spectral broadening, also two "ears" appear at the edges of the spectrum, where the ear at the low frequency side is relatively stronger. Increasing the current, the asymmetry becomes stronger, and local minima and maxima between the ears become visible in the spectrum. Such a spectrum is shown as Fig. 8.2b (Note the different frequency scale). At a cur-

---

[2]We found linewidths (FWHM) of 50 MHz for identical VCSELs with larger oxidation apertures.
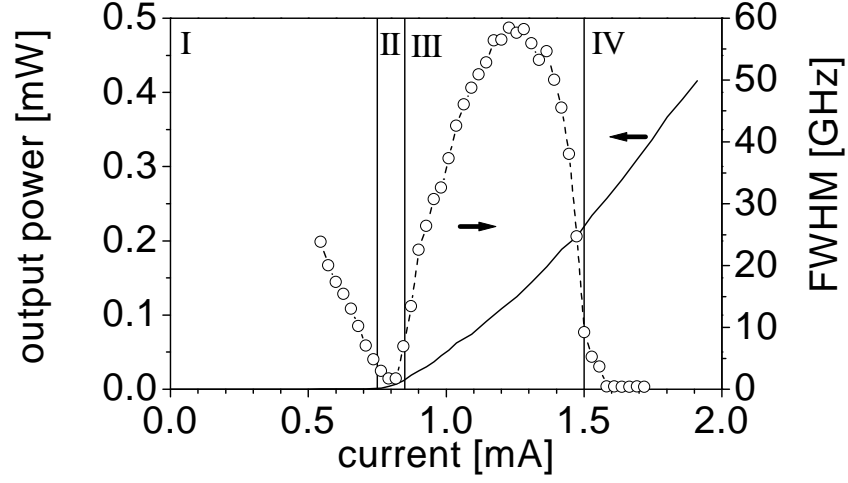
Figure 8.1: Output-input curve of a self-pulsating VCSEL (solid curve) and width (FWHM) of the optical spectrum as measured with a Fabry Pérot interferometer (dashed curve with circles).

rent of i=1.23 mA the optical spectrum had its maximum width of 58 GHz, being much broader than the emission spectrum *below* threshold.

We found a transition to fourth regime (IV) around a current of i=1.50 mA, where we started to resolve sharp peaks at the position of the weaker (high-frequency) ear in the optical spectrum (not shown). For a slightly higher current, the spectrum consisted of a strong main mode with several relaxation oscillation sidebands, as shown in Fig. 8.2c. At increasing current, these sidebands shifted to higher frequencies and rapidly became weaker and disappeared (not shown). The linewidth (FWHM), as measured with the self-heterodyne fiber delay setup, decreased to below 200 MHz.

Concurrently, we also measured intensity noise spectra with a 6-GHz photo receiver (New Focus 1514) and a 25-GHz RF-analyzer (HP 8563E). Typical intensity noise spectra of each regime are shown in Fig. 8.3, which were measured at currents of i=0.82 mA, i=1.26 mA, and i=1.64 mA, respectively. Figure 8.3a displays the intensity noise in regime (II), which consisted of a rather asymmetric peak. Increasing the laser current, the damping of the intensity noise decreased, resulting in an intensity noise spectrum with a very narrow peak with several (up to six) higher-order harmonics (see Fig. 8.3b, which corresponds to the same setting as Fig. 8.2b). Increasing the current leads to regime (IV); the intensity noise power decreased roughly two orders of magnitude, and normal relaxation oscillations were measured. This is shown in Fig. 8.3c, where all higher-order harmonics
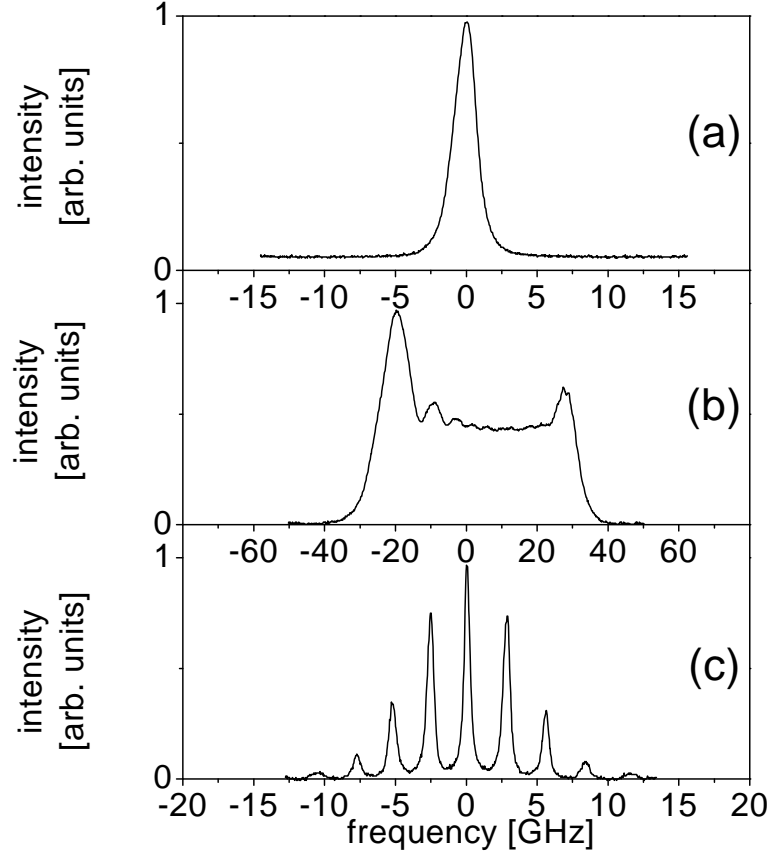
Figure 8.2: Optical spectra, as measured with a planar Fabry-Pérot cavity, at three different laser currents; namely at i=0.82 mA (a), i=1.26 mA (b), and i=1.53 mA (c).

have disappeared at i=1.64 mA. The dashed curve is a fit based on a standard expression for the intensity noise in the presence of relaxation oscillations [51]. The additional low-frequency peak arises from polarization modal noise [50,43].

The frequency and width (FWHM) of the intensity noise, as determined from the fundamental harmonics in Fig. 8.3, are plotted in Fig. 8.4 as a function of current. Typical values of 25 MHz for the width in regime (III) were obtained. The dependence of the relaxation oscillation frequency on the current, as displayed in Fig. 8.4, is surprisingly similar to that found for edge-emitters [86].

Much information can be extracted from a more-detailed analysis of Figs. 8.2 and 8.3. As a first example we analyze the strong modulation of regime (III).
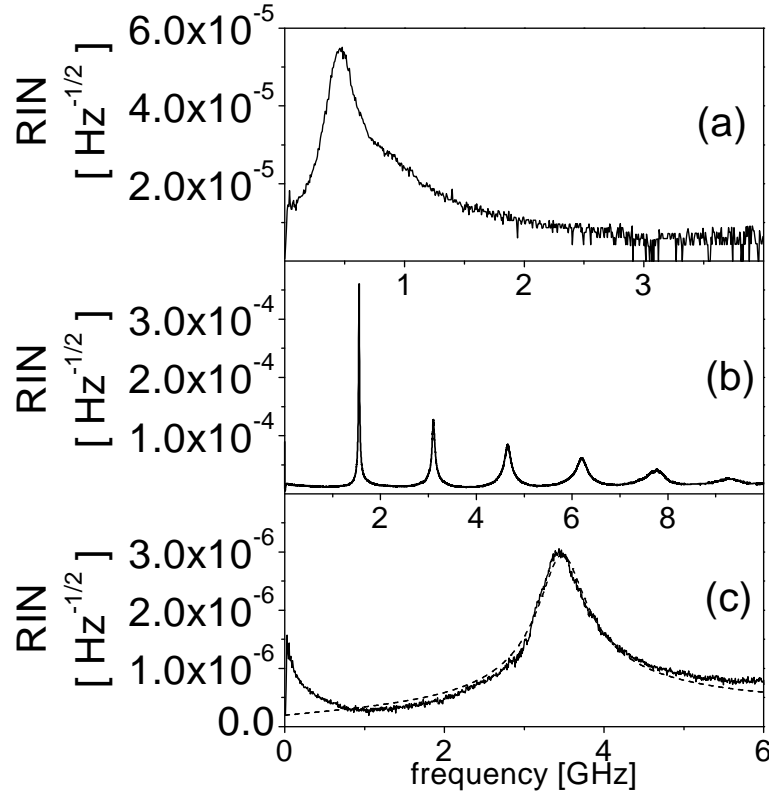
Figure 8.3: Intensity noise-spectra at three different laser currents; namely at i=0.82 mA (a), i=1.26 mA (b), and i=1.64 mA (c). The dashed curve in the lower box is a fit.

In Fig. 8.3b, the "area underneath the intensity noise peaks" can be used to estimate the modulation depth, for which we find approximately 100%, *i.e.*, from on to off. Furthermore, although the peak RIN of the various harmonics falls off rather rapidly, their spectral width also increase rapidly (roughly quadratically with harmonic order), so that the integrated noise power per harmonic decreases only mildly. This shows that the output intensity in regime (III) is concentrated in short optical pulses, with a high degree of periodicity determined by the spectrally narrow fundamental peak. During each pulse the inversion (and gain) is expected to drop rapidly, followed by a gradual buildup toward the next optical pulse (as in Q-switching). Due to a nonzero linewidth enhancement factor α, the refractive index of the gain medium will change simultaneously and the optical pulse will exhibit a considerable amount of frequency chirping, from high to low frequency.

119

This explains why the optical spectrum of Fig. 8.2b, which resembles that of a phase-modulated laser [94], is so much broader than the accompanying intensity noise spectrum of Fig. 8.3b. In fact, a comparison of the 58 GHz width in Fig. 8.2b with the 1.55 GHz fundamental frequency in Fig. 8.3b gives an estimated phase sweep of as much as $2m=58/1.55=37$ rad, where m is the modulation index.
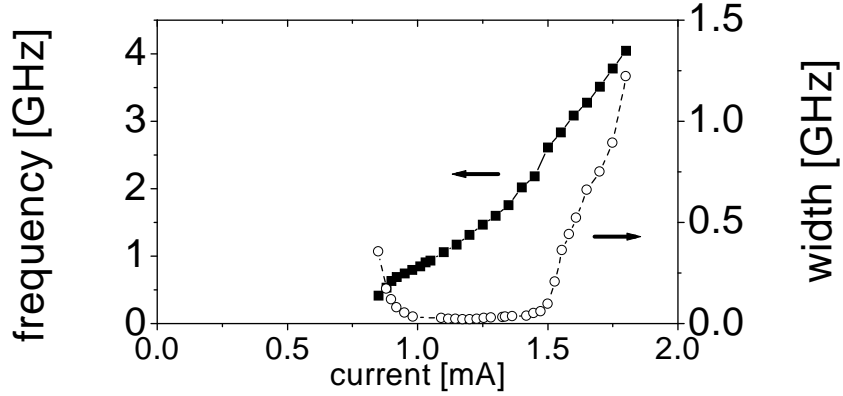

Figure 8.4: Frequency (solid squares) and width (open circles) of the self-pulsations, determined from the first harmonics of the intensity noise, as a function of laser current.

In regime (IV) the modulation is less deep and approximately harmonic, so that the optical field experiences the usual combination of amplitude (AM) and phase or frequency (FM) modulation. From the integrated noise power in Fig. 8.3c we deduce an AM field modulation of 6(1)%. From the relative strength of the sidebands in the accompanying optical spectrum (not shown) we find a phase modulation index of $m = 0.58(5)$ rad, which would suggest an unreasonably large value of $\alpha = 0.58/0.06 = 9(2)$. This shows that there must be additional damping mechanisms, which damp only intensity but not phase fluctuations; nonlinear gain is an obvious candidate [34].

The VCSELs used in the experiments have an oxidation mask diameter of d=2.3 μm. For identical VCSELs with larger values of d, we found a strong dependence of the strength of the intensity fluctuations on the oxidation diameter. For d=3.1 μm we observed, at most, a second harmonic in the intensity noise spectra (to be compared to Fig. 8.3b), whereas devices with d=3.9 and d=4.7 μm showed only very weak relaxation oscillations. This dependence can easily be understood, since for oxide-confined VCSELs with smaller apertures, the modal overlap with the unpumped regions outside the oxide aperture increases, thus resulting in stronger waveguiding effects [95] and in stronger saturable absorption.

Other properties of the oxide, besides its diameter, that could effect the strength of the self-pulsations are under study; the lateral position of the oxide compared to the field node may be important, whereas defects in the oxide (or stress) are expected to have a minor effect.

Furthermore, we observed these self-pulsations in a limited range around threshold also for 850-nm proton-implanted VCSELs, with d=10 μm, and in optically pumped VCSEL; in both cases a third harmonic in the intensity noise showed up. As the dimensions of the various structures are rather different, we conclude that their size alone does not fully determine the strength of self-pulsations in VCSELs.

8.3   Conclusion

In conclusion, we have observed strong, chirped self-pulsations in oxide-confined VCSELs, and a strong dependence of the self-pulsation strength on oxidation diameter. We have shown that large anharmonic oscillations are the cause of the anomalous broadening of the optical spectrum [see regime (III)]. By using standard compression techniques [96] the chirped pulses are, in principle, compressible to less than 20 ps pulse duration.

Chapter 9

Polarization supermodes of phase-coupled arrays of vertical-cavity semiconductor lasers [1]

We have experimentally investigated the supermodes of two-dimensional arrays of phase-coupled vertical-cavity surface-emitting lasers (VCSELs). By analyzing the individual lasing pixels, we demonstrate, surpisingly, that the polarization of a single supermode is highly nonuniform.

9.1   Introduction

Vertical-cavity surface-emitting lasers (VCSELs) have a planar symmetry that allows scaling in two dimensions (2D). Integration of VCSELs into 2D-arrays offers a wide range of applications, for instance, parallel optical data communication and applications that require a high output power. VCSELs in 2D-arrays can be organized, depending on the wafer processing, as individually addressable devices or as densely-packed elements (see Fig. 9.1). Individually addressable VCSELs organized in 2D-arrays can be used for parallel optical data communication [97,98]. In constrast, 2D-arrays of densely-packed elements have a high potential to increase the output power, which currently limits several applications of VCSELs. Densely-packed VCSELs will communicate with each other as the optical fields in neighbouring cavities overlap. As a consequence of this communication, phase-coupling occurs and the complete array starts to lase in an overall energetically favourable mode, a so-called supermode [18–20]. Whereas scalar aspects of supermodes have been studied extensively [18–20], polarization supermodes have not been addressed experimentally.

In this chapter, we analyze the polarization-mode structure of phase-coupled arrays, where all the lasing pixels are locked into a *single* supermode. We will demonstrate, quite surprisingly, that the individual pixels have a *different* polarization orientation and ellipticity.
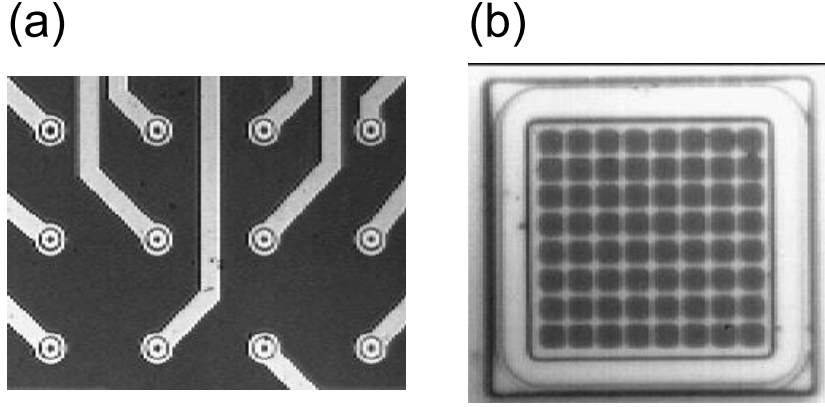

Figure 9.1: Top-view microscope images of a two-dimensional array of solitary VCSELs with 3×4 individually addressable devices (a) and of a two-dimensional array of densely-packed coupled VCSELs with 8×8 elements (b). For the array with individually addressable VCSELs (a), the array period is 250 μm, and the white stripes are current contacts. For the densely-packed VCSELs (b), the array period is 5 μm. The current for the total array (b) is injected via the white metal grid lines between the elements. Both structures were fabricated at Avalon Photonics, Zürich, Switzerland.

9.2   Spectrally-resolved spatial-imaging of polarization supermodes

For the experiment, we have used top-emitting phase-coupled arrays with an overall mesa geometry (see right-hand side of Fig. 9.1 and ref. [20]). In order to have electrical confinement a selective oxidation with a lateral dimension of 10 μm was used. The devices have a 1λ cavity, containing three InGaAs quantum wells, and emit at $\lambda \approx 960$ nm. The individual micro-cavities were defined by evaporating a metal grid (PtTiPtAu) on top of the mesa. This grid had a line width of 1 μm and openings of 4×4 μm. Phase-coupling can be achieved by properly adjusting the coupling strength between the optical resonators in the lattice, which is done by modifying the reflectivity difference between GaAs/metal and GaAs/air. The phase-coupling, or supermode oscillation, of a practical device can be checked easily by measuring the far-field intensity pattern; this consists of 4 lobes, as a consequence of the out-of-phase relation between neighboring elements [20]. The structures that we address have 4×4 and 8×8 pixels (see right-hand side of Fig. 9.1) and lase continuously (cw). The corresponding output-input curves are shown in Fig. 9.2. The threshold currents of these arrays are 4 mA and 15 mA,

respectively. Higher-order supermodes started lasing at currents of 10 mA (4×4) and 25 mA (8×8) according to a 20 dB criterion. We will restrict the analysis to the regime of fundamental supermode emission.

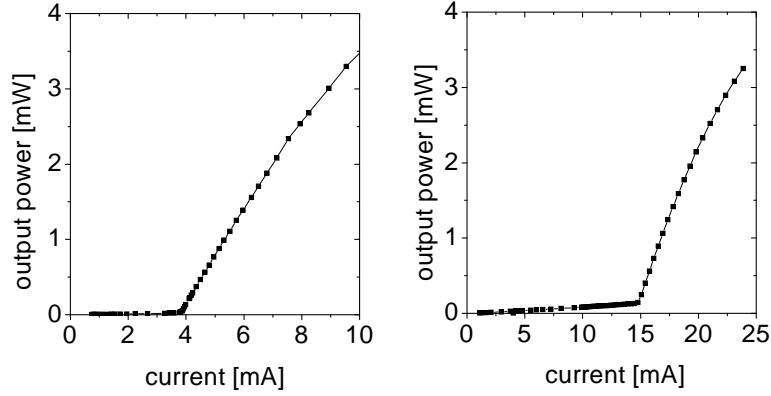**Figure 9.2**: Output-input curves of 4×4 phase-coupled array (left figure), and a 8×8 phase-coupled array (right figure).

To determine the full structure of these supermodes, we have performed a combined polarization and spectral projection together with spatial imaging. The experimental setup is shown in Fig. 9.3. The emission of a phase-coupled VC-SEL array was first passed through a polarization filter, which consisted of a $\lambda/4$ and a $\lambda/2$ waveplate in combination with an optical Faraday isolator (~ 60 dB). With this filter, the polarization orientation (ϕ) and ellipticity (χ) can be measured. Subsequently, the light was passed through a scanning Fabry-Pérot (FP) and sent to a photo-diode or a CCD camera. Detection with the photo-diode yields polarization-resolved optical spectra. Detection with the CCD camera, which was triggered by the scanning signal of the FP, yields any desired combination of polarization, spectral and spatial near-field selection.
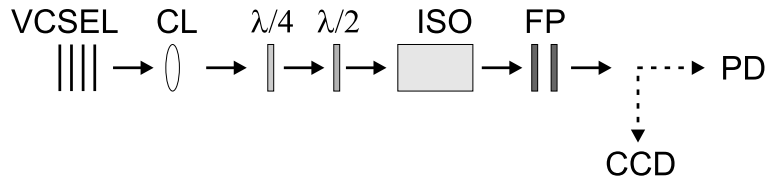

Figure 9.3: *Experimental setup; CL: collimating lens; ISO: optical isolator; FP: scanning Fabry Pérot; PD: photo diode; CCD: CCD camera.*

Figure 9.4 shows a typical optical spectrum of a phase-coupled array (4×4), operating at a drive current of 7.2 mA. In Fig. 9.4a the dominant (vertical) polarization was selected, showing that the phase-coupled array lases in a *single* supermode, whereas in Fig. 9.4b a projection onto the orthogonal (horizontal) polarization was performed. This second spectrum shows an additional, broader peak due to a nonlasing fundamental supermode, having approximate the same spatial profile as the lasing supermode but an orthogonal polarization. The difference in frequency between the lasing and nonlasing supermode, *i.e.* the birefringence, was found to be 10 GHz. The difference in width [Full Width at Half Maximum (FWHM)] between the lasing and nonlasing supermode, *i.e.* the dichroism, was found to be 0.5 GHz. For the 8×8 phase-coupled array we measured a value of 7.5 GHz for the birefringence and 0.5 GHz for the dichroism. The magnitudes of these optical anisotropies are comparable to values found from the doublet spectrum of solitary VCSELs (see chapter 2 and refs. [50,43]).
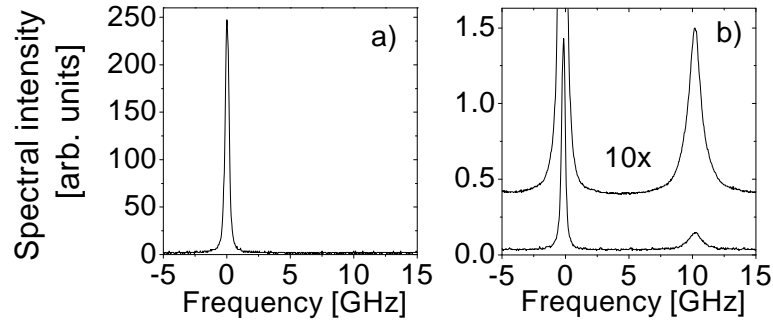

Figure 9.4: Optical Fabry-Pérot spectra of a 4×4 phase-coupled array of VCSELs at a current of 7.2 mA (I_{thr}=4 mA). Fig. 9.4a shows the dominant (vertical) polarization, whereas Fig. 9.4b shows the orthogonal (horizontal) polarization.

To our surprise, we could not suppress the lasing supermode in the orthogonal polarization projection better than shown in Fig. 9.4b. For the 4×4 phase-coupled array, we found a maximum suppression ratio of 200, whereas the lasing supermode of the 8×8 phase-coupled array could only be suppressed by a factor of 80. In contrast, for solitary VCSELs we generally reach a suppression of more than 40 dB (the polarization optics itself can easily reach 60 dB). Note that this suppression ratio refers to the *lasing* mode *only*; it has a different meaning than the usual mode ratio (see Sec. 2.6 and refs. [43,50]). The latter is equal to the modal power in the *lasing* polarization mode divided by that of the *nonlasing* polarization mode.

To understand physically these very modest suppression ratios, we have mea-
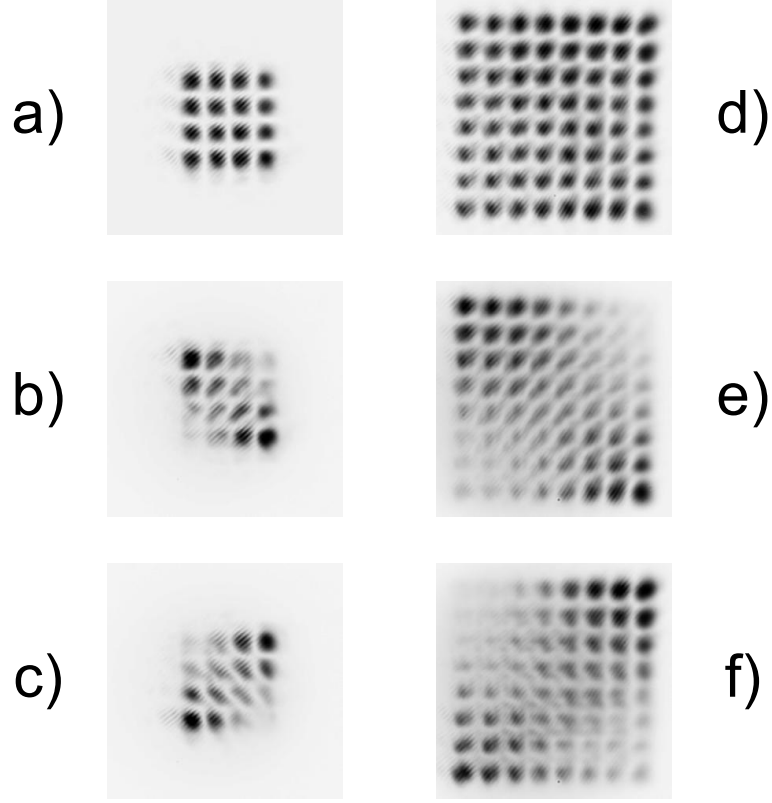
Figure 9.5: Spectrally and polarization-resolved near-field CCD images of the lasing supermode of a 4×4 (left column) and a 8×8 (right column) phase-coupled array. The distance between two pixels is 5 μm in all the images. The polarization projection angles (ϕ,χ) are in a) (90°,0°); b) (0°,-4°); c) (0°,4°); d) (88°,0°); e) (-2°,-10°); f) (-2°,10°).

sured near-field CCD images behind the FP. Using the scanning signal of the FP as a trigger for the CCD camera, we could spectrally select the lasing supermode and avoid the nonlasing supermode (see Fig. 9.4b). This is important for accurate determination of the polarization state (ϕ,χ).

Figure 9.5 shows the results for the 4×4 phase-coupled array (left column) and the 8×8 phase-coupled array (right column). Figures 9.5a and 9.5d show near-fields of the lasing supermode with the polarization filter optimized for maximum transmission (vertical polarization). By trying to block the supermode in the CCD image we observed that the individual pixels had a different polarization orientation and ellipticity. This is illustrated in Figs. 9.5b-c, where for different

orientations of the polarization filter ($\chi = \pm 4°$) some pixels can be blocked and other pixels not. The same effect was observed for the 8×8 phase-coupled array, shown in Figs. 9.5e-f, but for even larger ellipticity angles ($\chi = \pm 10°$).
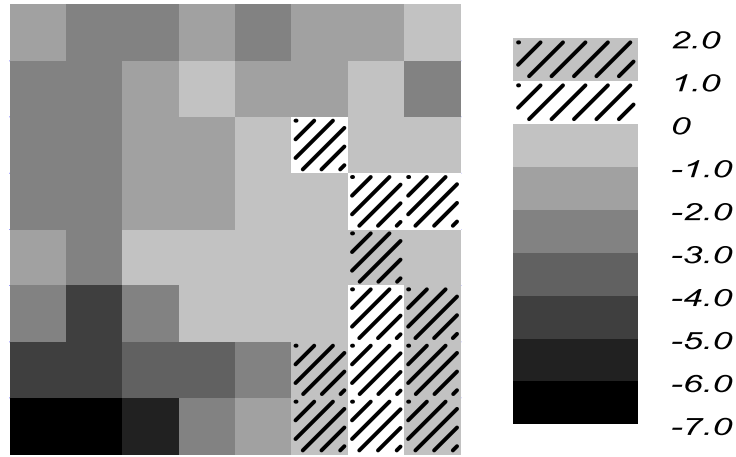

Figure 9.6: Two-dimensional distribution of the polarization blocking angle $\phi - 90$ (°) for a 8×8 phase-coupled array.

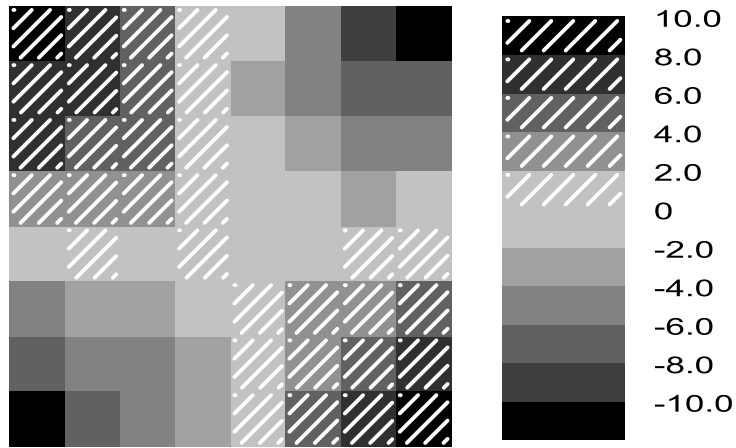**Figure 9.7**: Two-dimensional distribution of the ellipticity angle χ (°) for the same 8×8 phase-coupled array as in Fig. 9.6.

The overall result of our polarization analysis is shown in Fig. 9.6, with a map of the polarization blocking angle, and in Fig. 9.7, with a map of the ellipticity, of each lasing pixel of a 8×8 phase-coupled array. The differences in polarization angles and ellipticity of individual pixels are remarkably large: for the 8×8 phase-coupled arrays we have measured maximum differences in ϕ and χ of $8°$ and $20°$; for the 4×4 phase-coupled array we measured variations in ϕ and χ of $4°$ and $8°$. Note the different spatial symmetry of the ϕ distribution shown in Fig. 9.6 and the χ distribution shown in Fig. 9.7. Whereas the ϕ distribution deviates mainly in the lower left quadrant, the χ distribution has the diagonal symmetry already observed in Figs. 9.5e-f.

The observed spread in ϕ and χ over the VCSEL array provides a simple explanation for the limited suppression ratio found in Fig. 9.4b. When the polarization filter is set for optimum suppression of the central pixels, it will still pass light emitted by the outer pixels with their different ϕ and χ. A calculation based on the ϕ and χ distributions shown in Figs. 9.6 and 9.7, yields a suppression ratio of 100. For the 4×4 array this calculation gives a value of 400, both being in reasonable agreement with the measured values cited earlier.

If we translate the spread in ϕ and χ displayed in Figs. 9.6 and 9.7 into spread in birefringence and dichroism [44,24], we find that the latter spreads are of the same order of magnitude. This is different from the case of a 850 nm solitary VCSELs, where strain-induced birefringence dominated [44,24].

9.3 Discussion

From the ϕ and χ distributions in Figs. 9.6 and 9.7, it is obvious that the local polarization is not modified at random but in a deterministic way. This could have a thermal origin, as for solitary VCSELs it has been demonstrated that by applying strain with a focused laser beam, *i.e.*, a hot spot, the polarization state can be tailored [24,44]. In the case of the array, neighboring pixels could act as hot spots and affect the pixel polarization by thermally-induced strain. To study this potential thermal cross-talk, the phase-coupled arrays were operated with a *pulsed* current. CCD images were now taken directly behind the polarization filter; the FP could not be used, as current modulation causes a frequency chirp. To minimize errors from detection of the nonlasing supermode, the polarization filter was now set half way in between the orthogonal components. When increasing the pulse width from 100 ns to 1 ms (at a repetition period of 10 ms), no change in the blocking angles of separate pixels was observed, not even compared to cw operation. This proves that the nonuniform supermode polarization does *not* have a thermal origin, as it appears "instantaneously".

Another effect that could cause the nonuniform supermode polarization is vector diffraction [99]. A full vector description of the electro-magnetic field shows that the modes cannot be polarization pure, as a consequence of the finite aperture of the beam. However, vector diffraction effects are extremely small and scale with the fourth power of the numerical aperture [99]; a straight forward estimate shows that vector diffraction is *not* a likely explanation in view of the large experimental spread in ϕ and χ.

Having ruled out the previous two effects, we are left with unintentional local effects due to the oxide confinement and the evaporated metal grid and small nonuniformities due to imperfect device fabrication.

9.4   Conclusion

In conclusion, we have investigated the supermode structure of phase-coupled 2D arrays of VCSELs. High resolution FP measurements showed that all elements are locked into a *single*-frequency supermode. However, we observed large differences in the polarization states of the individual pixels; it is quite remarkable that, despite the large variation in the polarization states of individual pixels, lasing occurs in a single supermode. Generally, for practical phase-coupled arrays an uniform polarization is preferred since it presumably leads to lower threshold currents and higher output powers. However, for special applications one may consider phase-coupled arrays with tailored polarization patterns having a high spectral purity.

References

[1] R. N. Hall, G. E. Fenner, J. D. Kingsley, T. J. Soltys, and R. O. Carlson, Phys. Rev. Lett. **9**, 366 (1962).

[2] H. Soda, K. Iga, C. Kitahara, and Y. Suematsu, Jpn. J. Appl. Phys. **18**, 2329 (1979).

[3] J. L. Jewell, A. Scherer, S. L. McCall, Y. H. Lee, S. Walker, J. P. Harbison, and L. T. Florex, Electron. Lett. **25**, 1124 (1989).

[4] G. M. Yang, M. H. MacDougal, and P. D. Dapkus, Electron. Lett. **33**, 886 (1995).

[5] J. Hecht, Laser Focus World **37**, 123 (2001).

[6] S. Nakagawa, E. Hall, G. Almuneau, J. K. Kim, D. A. Buell, H. Kroemer, and L. A. Goldren, Appl. Phys. Lett. **78**, 1337 (2001).

[7] R. Jäger, M. Grabherr, C. Jung, G. Reiner, B. Weigl, and K. J. Ebeling, Electron. Lett. **33**, 330 (1997).

[8] D. L. Huffaker, D. G. Deppe, K. Kumar, and T. J. Rogers, Appl. Phys. Lett. **65**, 97 (1994).

[9] J. M. Dallesasse, N. Holonyak, A. R. Sugg, T. A. Richard, and N. Elzein, Appl. Phys. Lett. **57**, 2844 (1990).

[10] K. D. Choquette, K. M. Geib, C. I. H. Ashby, R. D. Twesten, O. Blum, H. Q. Hou, D. M. Follstaedt, B. E. Hammons, D. Mathes, and R. Hull, IEEE J. Sel. Top. Quantum. Electron. **3**, 916 (1997).

[11] M. Grabherr, R. Jäger, M. Miller, C. Thalmaier, J. Heerlein, R. Michalzik, and K. J. Ebeling, IEEE Phot. Tech. Lett. **10**, 1061 (1998).

[12] Y. Yamamoto and R. E. Slusher, Physics Today **46**, 66 (1993).

[13] K. D. Choquette, R. P. Schneider Jr., K. L. Lear, and R. E. Leibenguth, IEEE J. Sel. Top. Quantum. Electron. **1**, 661 (1995).

[14] A. K. Jansen van Doorn, *Symmetry breaking in vertical-cavity semiconductor lasers* (PhD. thesis, Leiden University, the Netherlands, 1996).

[15] M. San Miguel, Q. Feng, and J. V. Moloney, Phys. Rev. A **52**, 1728 (1995).

[16] Vixel Corporation, 325 Interlocken Parkway, Broomfield, CO 80021, USA, model PRI-LA-S-850-1x8-3S.

[17] H. Pier, E. Kapon, and M. Moser, Nature **407**, 880 (2000).

[18] R. A. Morgan, K. Kojima, T. Mullaly, G. D. Guth, M. W. Focht, R. E. Leibenguth, and M. Asom, Appl. Phys. Lett. **61**, 1160 (1992).

[19] M. Orenstein, E. Kapon, J. P. Harbison, L. T. Florez, and G. Stoffel, Appl. Phys. Lett. **60**, 1535 (1992).

[20] F. Monti di Sopra, M. Brunner, H.-P. Gauggel, H. P. Zappe, M. Moser, R. Hövel, and E. Kapon, Appl. Phys. Lett. **77**, 2283 (2000).

[21] C. H. Henry, IEEE J. Quantum. Electron. **18**, 259 (1982).

[22] M. P. van Exter, A. Al-Remawi, and J. P. Woerdman, Phys. Rev. Lett. **80**, 4875 (1998).

[23] J. Martin-Regalado, F. Prati, M. San Miguel, and N. Abraham, IEEE J. Quantum. Electron. **33**, 765 (1997).

[24] A. K. Jansen van Doorn, M. P. van Exter, A. M. van der Lee, and J. P. Woerdman, Phys. Rev. A **55**, 1473 (1997).

[25] M. P. van Exter, R. F. M. Hendriks, and J. P. Woerdman, Phys. Rev. A **57**, 2080 (1998).

[26] H. F. Hofmann and O. Hess, Quant. Sem. Opt. **10**, 87 (1998).

[27] H. van der Lem and D. Lenstra, Opt. Lett. **22**, 1698 (1997).

[28] M. Travagnin, M. P. van Exter, A. K. Jansen van Doorn, and J. P. Woerdman, Phys. Rev. A **54**, 1647 (1997).

[29] W. van Haeringen, Phys. Rev. **158**, 256 (1967).

[30] J. Martin-Regalado, J. L. A. Chilla, J. J. Rocca, and P. Brusenbach, Appl. Phys. Lett. **70**, 3350 (1997).

[31] M. Born and E. Wolf, *Principles of optics* (Pergamon Press, Oxford, England, 1980).

[32] M. Travagnin, Phys. Rev. A **56**, 4094 (1997).

[33] K. Petermann, *Laser diode modulation and noise* (Kluwer, Dordrecht, the Netherlands, 1988).

[34] M. P. van Exter, W. A. Hamel, J. P. Woerdman, and B. R. P. Zeijlmans, IEEE J. Quantum. Electron. **28**, 1470 (1992).

[35] D. V. Kuksenkov, H. Temkin, and S. Swirhun, Appl. Phys. Lett. **67**, 2141 (1995).

[36] R. F. M. Hendriks, M. P. van Exter, and J. P. Woerdman, IEEE J. Quantum. Electron. **34**, 1455 (1998).

[37] C. Gardiner, *Handbook of Stochastic Methods* (Springer, Berlin, Germany, 1985).

[38] S. Ciuchi, M. San Miguel, and N. B. Abraham, Phys. Rev. A **57**, 3843 (1998).

[39] H. A. Kramers, Physica **7**, 284 (1940).

[40] R. Roy, R. Short, J. Durnin, and L. Mandel, Phys. Rev. Lett. **45**, 1486 (1980).

[41] D. Lenstra and S. Singh, Phys. Rev. A **28**, 2318 (1983).

[42] M. Osinski and J. Buus, IEEE J. Quantum. Electron. **23**, 9 (1987).

[43] M. P. van Exter, M. B. Willemsen, and J. P. Woerdman, Appl. Phys. Lett. **74**, 2274 (1999).

[44] A. K. Jansen van Doorn, M. P. van Exter, and J. P. Woerdman, Appl. Phys. Lett. **69**, 1041 (1996).

[45] M. P. van Exter, A. K. Jansen van Doorn, and J. P. Woerdman, Phys. Rev. A **56**, 845 (1997).

[46] C. J. Chang-Hasnain, J. P. Harbison, L. T. Florez, and N. G. Stoffel, Electron. Lett. **27**, 163 (1991).

[47] E. Goobar, J. W. Scott, B. Thibeault, G. Robinson, Y. Akulova, and L. A. Goldren, Appl. Phys. Lett. **67**, 3697 (1995).

[48] D. C. Kilper, P. A. Roos, J. L. Carlsten, and K. L. Lear, Phys. Rev. A **55**, R3323 (1997).

[49] J. L. Vey and W. Elsasser, Opt. Lett. **23**, 721 (1998).

[50] M. P. van Exter, M. B. Willemsen, and J. P. Woerdman, Phys. Rev. A **58**, 4191 (1998).

[51] M. C. Tatham, I. F. Lealman, C. P. Seltzer, L. D. Westbrook, and D. M. Cooper, IEEE J. Quantum. Electron. **28**, 408 (1992).

[52] M. P. van Exter, M. B. Willemsen, and J. P. Woerdman, Quant. Sem. Opt. **1**, 637 (1999).

[53] M. B. Willemsen, M. U. F. Khalid, M. P. van Exter, and J. P. Woerdman, Phys. Rev. Lett. **82**, 4815 (1999).

[54] C. J. Chang-Hasnain, J. P. Harbison, G. Hasnain, A. C. von Lehmen, L. T. Florez, and N. G. Stoffel, IEEE J. Quantum. Electron. **27**, 1402 (1991).

[55] J. Martin-Regalado, S. Balle, and M. San Miquel, Opt. Lett. **22**, 460 (1997).

[56] G. Giacomelli and F. Marin, Quant. Sem. Opt. **10**, 469 (1998).

[57] P. Hänggi, P. Talkner, and M. Borkovec, Rev. Mod. Phys. **62**, 251 (1990).

[58] A. K. Jansen van Doorn, M. P. van Exter, and J. P. Woerdman, Appl. Phys. Lett. **70**, 1041 (1996).

[59] B. McNamara, K. Wiesenfeld, and R. Roy, Phys. Rev. Lett. **60**, 2626 (1988).

[60] G. Giacomelli, F. Marin, and I. Rabbiosi, Phys. Rev. Lett. **82**, 675 (1999).

[61] R. Jin, D. Boggavarapu, M. Sargent III, P. Meystre, H. M. Gibbs, and G. Khitrova, Phys. Rev. A **49**, 4038 (1994).

[62] S. Balle, E. Tokachova, M. San Miguel, J. R. Tredicce, J. Martin-Regalado, and A. Gahl, Opt. Lett. **24**, 1121 (1999).

[63] R. Roy and L. Mandel, Opt. Commun. **34**, 133 (1981).

[64] A. Le Floch, G. Ropars, and J. M. Lenormand, Phys. Rev. Lett. **52**, 918 (1984).

[65] G. Ropars, A. Le Floch, and R. Le Naour, Phys. Rev. A **46**, 623 (1992).

[66] M. B. Willemsen, M. P. van Exter, and J. P. Woerdman, Phys. Rev. A **60**, 4105 (1999).

[67] H. Risken, in *The Fokker-Planck Equation* (Springer-Verlag, Berlin, Germany, 1996), Chap. 5.

[68] J. Martin-Regalado, M. San Miguel, N. B. Abraham, and F. Prati, Opt. Lett. **21**, 351 (1996).

[69] D. Burak, J. V. Moloney, and R. Binder, Phys. Rev. A **61**, 3809 (2000).

[70] H. F. Hofmann and O. Hess, Phys. Rev. A **56**, 868 (1997).

[71] G. Giacomelli, F. Marin, M. Gabrysch, K. H. Gulden, and M. Moser, Opt. Commun. **146**, 136 (1998).

[72] J.-L. Vey, C. Degen, K. Auen, and W. Elsässer, Phys. Rev. A **60**, 3284 (1999).

[73] F. Prati, G. Giacomelli, and F. Marin, Phys. Rev. A **62**, 3810 (2000).

[74] D. R. Shelly, T. W. S. Garrison, and M. Beck, Opt. Express **7**, 249 (2000).

[75] M. B. Willemsen, M. P. van Exter, and J. P. Woerdman, Phys. Rev. Lett. **84**, 4337 (2000).

[76] Encyclopædia Britannica.

[77] H. O. Peitgen, H. Jürgens, and D. Saupe, *Chaos and Fractals* (Springer Verlag, New York, 1992).

[78] A. K. Jansen van Doorn, M. P. van Exter, and J. P. Woerdman, IEEE J. Quantum. Electron. **34**, 700 (1998).

[79] T. Ohtoshi, T. Kuroda, A. Niwa, and S. Tsuji, Appl. Phys. Lett. **65**, 1886 (1994).

[80] B. Möller, E. Zeeb, U. Fiedler, T. Hackbarth, and K. J. Ebeling, IEEE Phot. Tech. Lett. **6**, 921 (1994).

[81] W. Schmid, C. Jung, B. Weigl, G. Reiner, R. Michalzik, and K. J. Ebeling, IEEE Phot. Tech. Lett. **8**, 1288 (1996).

[82] Z. Toffano, A. Destrez, C. Birocheau, and L. Hassine, Electron. Lett. **28**, 9 (1992).

[83] D. V. Kuksenkov, H. Temkin, and S. Swirhun, Appl. Phys. Lett. **66**, 1720 (1995).

[84] J. P. van der Ziel, J. L. Merz, and T. Paoli, J. Appl. Phys **50**, 4620 (1979).

[85] T. L. Paoli, Appl. Phys. Lett. **34**, 652 (1979).

[86] C. R. Mirasso, G. H. M. van Tartwijk, E. Hernández-García, D. Lenstra, S. Lynch, P. Landais, P. Phelan, J. O'Gorman, M. San Miguel, and W. Elsäßer, IEEE J. Quantum. Electron. **35**, 764 (1999).

[87] S. Matsui, H. Takiguchi, H. Hayashi, S. Yamamoto, S. Yano, and Hijikata, Appl. Phys. Lett. **43**, 219 (1983).

[88] K. D. Choquette, H. Q. Hou, K. L. Lear, H. C. Chui, K. M. Geib, A. Mar, and B. E. Hammons, Electron. Lett. **32**, 459 (1996).

[89] The oxide-confined VCSELs are from CSEM, Zürich Switserland.

[90] The optically pumped VCSELs are from CSEM, Zürich Switserland.

[91] R. Lang, Jpn. J. Appl. Phys. **19**, L93 (1980).

[92] J. Buus, IEEE J. Quantum. Electron. **19**, 953 (1983).

[93] J. Buus, IEEE Phot. Tech. Lett. **6**, 1179 (1994).

[94] A. E. Siegman, in *Lasers* (University Science Books, Hill Valley, 1986), Chap. 26.

[95] M. Brunner, K. Gulden, R. Hövel, M. Moser, and M. Ilegems, Appl. Phys. Lett. **76**, 7 (2000).

[96] O. E. Martinez, IEEE J. Quantum. Electron. **23**, 59 (1987).

[97] B. Möller, E. Zeeb, T. Hackbarth, and K. J. Ebeling, IEEE Phot. Tech. Lett. **6**, 1056 (1994).

[98] Y. Kohama, Y. Ohiso, S. Fukushima, and T. Kurokawa, IEEE Phot. Tech. Lett. **6**, 918 (1994).

[99] W. L. Erikson and S. Singh, Phys. Rev. E **49**, 5778 (1994).

Samenvatting

In dit proefschrift wordt een onderzoek beschreven naar de polarisatiefluctuaties van een halfgeleider microlaser van het type VCSEL (spreek uit "vixel"). Het acroniem VCSEL betekent Vertical Cavity Surface Emitting Laser. Deze samenvatting begint met een algemene inleiding over VCSELs, gevolgd door een overzicht van het onderzoek in dit proefschrift.

VCSELs

Het aantal toepassingen van lasers in het dagelijkse leven is tegenwoordig talrijk. Cd/dvd-spelers, laserprinters, kassascanners, medische toepassingen en communicatienetwerken zijn bekende voorbeelden. In bijna al deze toepassingen worden halfgeleiderlasers gebruikt. De voornaamste redenen voor de populariteit van dit type laser zijn de lange levensduur en het kleine formaat. In 2000 werden wereldwijd meer dan een half miljard halfgeleiderlasers verkocht.

Een VCSEL is een moderne halfgeleider microlaser met afmetingen van een fractie van een haardikte. Halfgeleiderlasers worden gemaakt door uiterst dunne lagen verschillend halfgeleidermateriaal op een substraat te laten groeien. Het bijzondere van een VCSEL is dat de laserbundel loodrecht op de lagenstructuur staat. Dit is in tegenstelling tot conventionele halfgeleiderlasers die worden toegepast in cd-spelers, waar het licht parallel aan de lagenstructuur loopt. Het "handige" van de VCSEL-constructie is dat de verticale looprichting van de bundel het mogelijk maakt zeer veel van dit soort lasers naast elkaar op één halfgeleiderplak te fabriceren. In figuur 1 staat een bovenaanzicht afgebeeld van een plak met VCSEL microlasers gemaakt met een microscoop. Het donkergrijze vlak is de bovenste laag halfgeleidermateriaal. Op deze laag zijn (witte) stroomcontacten gemonteerd om de individuele VCSELs aan te sturen. Als de lasers aanstaan komen de bundels loodrecht omhoog uit de kleine ronde zwarte openingen. Een halfgeleiderplak van een vierkante centimeter kan meer dan tienduizend werkende lasers bevatten. Deze twee-dimensionale roosters met afzonderlijk te adresseren VCSELs zijn interessant voor parallelle optische datacommunicatie.

In figuur 2 is een dwarsdoorsnede van een VCSEL-lagenstructuur getekend. Zoals iedere laser bestaat ook een VCSEL uit twee spiegels, die een trilholte vormen, en een lichtversterkend medium of actieve laag. De trilholte van een
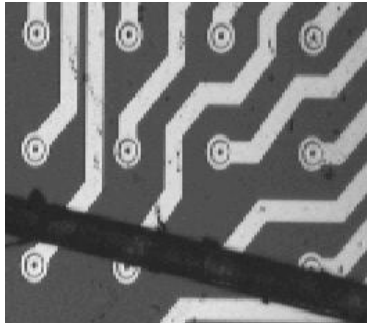
Figuur 1: Rooster van VCSEL microlasers. De afstand tussen de lasers is 250 micrometer. Als een laser aanstaat, komt het licht uit het kleine zwarte puntje in het midden van de "schietschijf". De zwarte balk die de onderste rij lasers bedekt is een haar.

VCSEL wordt gevormd door twee Braggspiegels, die uit vele lagen halfgeleidermateriaal bestaan. Om laserwerking te krijgen moet het laserlicht in de trilholte passen en de afstand tussen de twee spiegels gelijk zijn aan een veelvoud van de halve golflengte van het laserlicht. De afstand tussen de Braggspiegels in een VCSEL is slechts één optische golflengte, waardoor VCSELs tot de kleinst mogelijke lasers behoren. Vanwege het kleine formaat zijn VCSELs zowel interessant uit het oogpunt van toepassingen als om wetenschappelijke redenen. VCSELs zijn attractief voor toepassingen, omdat lasers met kleine afmetingen erg gemakkelijk met micro-elektronica te integreren zijn. De wetenschappelijke interesse komt voort uit het feit dat het opsluiten van licht in een volume van een aantal kubieke golflengtes fundamentele aspecten, van quantummechanische aard, met zich meebrengt.

De stroom die de VCSEL aanstuurt wordt geïnjecteerd via het metalen contact boven op de halfgeleiderplak (zie figuur 2). De ladingsdragers bereiken de actieve laag omdat de twee Braggspiegels respectievelijk positief en negatief-gedoteerd zijn. Het lichtversterkende medium of de actieve laag is een quantumput met een dikte van 10 nanometer. In de quantumput wordt de stroom omgezet in licht en versterkt door middel van gestimuleerde emissie. Het licht kaatst op en neer tussen de Braggspiegels en verlaat de structuur door de bovenste Braggspiegel, omdat deze spiegel net niet perfect reflecterend is. Behalve voor deze verticale opsluiting van het licht door de Braggspiegels moet ook voor horizontale opsluiting van het licht worden gezorgd. Hiervoor is een "roesttechniek" ontwikkeld; deze techniek bestaat uit het van buitenaf laten roesten van een dun laagje aluminiumarseen in de bovenste Braggspiegel tot aluminiumoxide, hetgeen geen stroom geleidt. Door het roestproces op tijd te stoppen, ontstaat in het midden van de oxidelaag een roestvrije opening waar de stroom doorheen gaat en die tevens het licht opsluit.

In figuur 2 staat ook een conventionele halfgeleiderlaser afgebeeld. Een conventionele halfgeleiderlaser is ongeveer honderdmaal groter dan een VCSEL

(0.3 mm in plaats van enkele golflengtes). Het licht in dit type laser loopt parallel aan de actieve laag. Om deze lasers te produceren wordt de halfgeleiderplak in stukken gebroken. De breukvlakken fungeren als spiegels. In dit geval is het niet mogelijk lasers te integreren in twee-dimensionale roosters.

Ten opzichte van een conventionele halfgeleiderlaser heeft de structuur van een VCSEL diverse voordelen. Het kleine volume van een VCSEL leidt tot lage drempelstromen en een efficiënte omzetting van elektrische energie naar licht. Door de hoge mate van cilindersymmetrie van een VCSEL is de laserbundel rond en gemakkelijk in glasvezels te koppelen. De algemene verwachting is dat VCSELs een belangrijke rol gaan spelen in datacommunicatie over korte afstanden. Een nadeel van de ronde VCSEL-geometrie is dat een intrinsieke polarisatievoorkeur ontbreekt (het onderwerp van dit proefschrift). De beperkte polarisatiepuurheid van het laserlicht uit VCSELs staat sommige toepassingen in de weg.
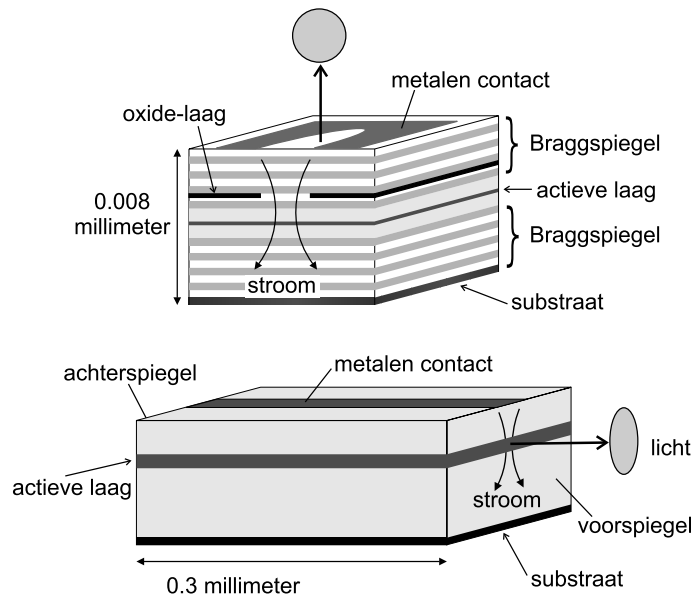
Figuur 2: VCSEL microlaser (boven) en conventionele halfgeleiderlaser (onder). Let op het grote verschil in schaal.

Dit proefschrift

Het centrale onderwerp van dit proefschrift is het polarisatiefluctuatiegedrag in het laserlicht van VCSELs. Laserlicht is een elektromagnetische golf en heeft dus een specifieke trillingsrichting of polarisatie. In het geval van een VCSEL liggen alle toegestane polarisaties in het vlak van de halfgeleiderplak. Op grond van cilindersymmetrie zouden al deze polarisaties gelijkwaardig moeten zijn. In een praktische VCSEL overwint één lineaire polarisatie, de overheersende of dominante polarisatie. Mechanismen die de polarisatiesymmetrie opheffen zijn anisotropieën in de trilholte en/of quantumput. Dat de polarisatievoorkeur van een VCSEL erg zwak is blijkt uit de aanwezigheid van polarisatiefluctuaties. In een dominant x-gepolariseerde VCSEL is een klein gedeelte van het laserlicht y-gepolariseerd door polarisatieruis. De oorzaak van polarisatiefluctuaties is van fundamentele aard, namelijk quantumruis. Deze quantumruis wordt veroorzaakt door spontane emissie. Spontane emissie is een toevalsproces waarvan de invloed in een laser toeneemt naarmate een laser kleiner is. Dit verklaart het prominente karakter van polarisatiefluctuaties in VCSELs. Naast de fundamentele aspecten van polarisatiefluctuaties is kennis van polarisatieruis ook van praktisch belang. Een slecht gedefinieerde polarisatietoestand is duidelijk nadelig voor toepassingen. Het succesvol kunnen toepassen van VCSELs vereist daarom inzicht in de polarisatie-eigenschappen. Dit proefschrift combineert een experimenteel onderzoek aan polarisatiefluctuaties in VCSELs met een theoretische analyse.

In hoofdstuk 2 wordt een theoretisch model geïntroduceerd dat de polarisatiedynamica van VCSELs beschrijft. In dit model wordt zowel het stabiliserende effect van de anisotropieën in de trilholte en quantumput op de polarisatie als de destabiliserende quantumruis meegenomen. De polarisatie van licht wordt beschreven door twee vrijheidsgraden, namelijk de polarisatiehoek ϕ en de ellipticiteit χ. Aangezien de spontane emissie isotroop gepolariseerd is, zou men verwachten dat de fluctuaties in ϕ en χ even sterk zijn. In hoofdstuk 2 wordt echter aangetoond dat de polarisatiefluctuaties in hoge mate anisotroop kunnen zijn ten gevolge van het breken van de polarisatiesymmetrie in de quantumput.

De aanwezigheid van een fractie y-gepolariseerd licht in een bijna volledig x-gepolariseerde VCSEL leidt tot polarisatiecompetitie. Hoofdstuk 3 gaat nader in op polarisatiecompetitie en de fluctuaties in de totale intensiteit, zijnde de som van de intensiteiten in de x-en y-polarisaties. Door de correlatie tussen de fluctuaties in de dominante x-polarisatie en de verstorende y-polarisatie te analyseren, demonstreren we dat polarisatiefluctuaties geen extra effect hebben op de totale intensiteitsruis.

Een polarisatiesprong is een buitengewoon sterke polarisatiefluctuatie, waarbij

de dominante polarisatie plotseling omklapt van *x* naar *y* of omgekeerd. In het experiment beschreven in hoofdstuk 4 laten we zien dat het aantal polarisatiesprongen per tijdseenheid veranderd kan worden over 8 ordes van grootte; van 20 miljoen sprongen per seconde tot minder dan 1 sprong per seconde. Het aantal polarisatiesprongen wordt gemanipuleerd door op een gecontroleerde wijze mechanische spanning op de VCSEL aan te brengen. Deze resultaten zijn in overeenstemming met een analytisch oplosbaar model, gebaseerd op de in hoofdstuk 2 geïntroduceerde theorie. Wiskundig gezien komt dit analytische model overeen met een door H. A. Kramers (1894-1952) in 1940 ontwikkelde theorie voor het beschrijven van de snelheid van chemische reacties.

Deze "Kramers-theorie voor VCSELs" doet een opmerkelijke voorspelling voor de polarisatie die omklapt van de lineaire *x*-polarisatie naar de lineaire *y*-polarisatie. Tijdens het omklappen van de polarisatie zou het licht afwisselend vele malen lineair gepolariseerd en circulair gepolariseerd moeten worden. De tijdschaal waarop een polarisatiesprong plaatsvindt is slechts enkele nanoseconden. In hoofdstuk 5 wordt deze verrassende voorspelling experimenteel bevestigd door de polarisatie tijdens een polarisatiesprong te volgen.

In hoofdstuk 6 wordt het breken van de polarisatiesymmetrie door de trilholte en door de quantumput afzonderlijk beschouwd. In beide gevallen wordt aangetoond dat polarisatie-excursies beschreven kunnen worden met loxodromen (bolspiralen).

De quantumruis of spontane emissie beperkt niet alleen de polarisatiepuurheid van het laserlicht, maar veroorzaakt ook fluctuaties in de kleur van het licht. In hoofdstuk 7 worden de fluctuaties in de polarisatie en in de kleur van het laserlicht geanalyseerd. Rond de laserdrempel vertonen beide type fluctuaties anomaal gedrag.

Met de roesttechniek kan op gecontroleerde wijze de afmetingen van een VCSEL in horizontale richtingen worden gevarieerd. In hoodstuk 8 worden VCSELs bestudeerd met uiterst kleine roestvrije openingen. Het laserlicht komt gepulst uit deze VCSELs, ondanks het feit dat ze door een continue elektrische stroom worden aangestuurd. We tonen aan dat dit een gevolg is van de nauwe opsluiting, hetgeen de ruimtelijke overlap tussen de ladingsdragers en het optische veld vermindert.

Tenslotte worden in hoofdstuk 9 twee-dimensionale roosters met VCSELs bestudeerd. Naarmate de roosterafstand kleiner wordt zullen de VCSELs met elkaar gaan communiceren via het optische veld dat van de ene VCSEL transversaal weglekt naar de trilholtes van z'n "buren". Het gevolg van deze communicatie is dat alle VCSELs in het rooster één mode kiezen, een zogenaamde supermode, om gezamelijk in te oscilleren. In de bestudeerde roosters is de onderlinge af-

stand tussen twee VCSELs slechts 5 micrometer. Het supermodepatroon van dit rooster bestaat uit buur-VCSELs die uit-fase laseren. Door het rooster van VC-SELs zowel polarisatie-als spectraal-opgelost af te beelden laten we zien dat de supermodepolarisatie in hoge mate niet-uniform is. Het bijzondere hieraan is dat VCSELs in het rooster hun fase aan elkaar opleggen, maar hun polarisatie individueel "kiezen".

List of publications

1. *Spontaneous emission spectra of optically pumped vertical-cavity surface-emitting lasers*,
   R. F. M. Hendriks, M. B. Willemsen, M. P. van Exter, J. P. Woerdman,
   L. Weegels, K. H. Gulden, and M. Moser,
   Optics Communications **149**, 50-54 (1997).

2. *Birefringence in TEM_{01} optically-pumped VCSELs*,
   S. F. Pereira, M. B. Willemsen, R. F. M. Hendriks, M. P. van Exter, and
   J. P. Woerdman,
   Optics Communications **153**, 282-284 (1998).

3. *Pinning of daisy modes in optically pumped vertical-cavity surface-emitting lasers*,
   S. F. Pereira, M. B. Willemsen, M. P. van Exter, and J. P. Woerdman,
   Applied Physics Letters **73**, 2239-2241 (1998).

4. *Polarization fluctuations in vertical-cavity semiconductor lasers*,
   M. P. van Exter, M. B. Willemsen, and J. P. Woerdman,
   Physical Review A **58**, 4191-4205 (1998).

5. *Polarization modal noise and dichroism in vertical-cavity semiconductor lasers*,
   M. P. van Exter, M. B. Willemsen, and J. P. Woerdman,
   Applied Physics Letters **74**, 2274-2276 (1999).

6. *Polarization switching of a vertical-cavity semiconductor laser as a Kramers hopping problem*,
   M. B. Willemsen, M. U. F. Khalid, M. P. van Exter, and J. P. Woerdman,
   Physical Review Letters **82**, 4815-4818 (1999).

7. *Correlated fluctuations in the polarization modes of a vertical-cavity semiconductor laser*,
   M. B. Willemsen, M. P. van Exter, and J. P. Woerdman,
   Physical Review A **60**, 4105-4113 (1999).

8. *Effect of mode-partition noise on intensity squeezing in a two-mode laser*,
   M. P. van Exter, M. B. Willemsen, and J. P. Woerdman,
   Quantum Semiclassical Optics, **1**, 637-645 (1999).

9. *Characterizing and understanding VCSEL polarization noise*,
   M. P. van Exter, M. B. Willemsen, and J. P. Woerdman,
   Proceedings of SPIE vol. 3946, 58-68 (2000).

10. *Anatomy of a polarization switch of a vertical-cavity semiconductor laser*,
    M. B. Willemsen, M. P. van Exter, and J. P. Woerdman,
    Physical Review Letters **84**, 4337-4340 (2000).

11. *Frequency spectra and waveguiding of a family of daisy modes in vertical-cavity surface-emitting lasers*,
    S. F. Pereira, M. B. Willemsen, M. P. van Exter, and J. P. Woerdman,
    Optics Communications **179**, 485-489 (2000).

12. *Self-pulsations in vertical-cavity semiconductor lasers*,
    M. B. Willemsen, A. S. van de Nes, M. P. van Exter, J. P. Woerdman,
    M. Brunner, and R. Hövel,
    Applied Physics Letters **77**, 3514-3516 (2000).

13. *Polarization-resolved linewidth-power product of a vertical-cavity semiconductor laser*,
    M. B. Willemsen, A. S. van de Nes, M. P. van Exter, J. P. Woerdman,
    M. Kicherer, R. King, R. Jäger, and K. J. Ebeling,
    Journal of Applied Physics **89**, 4183-4185 (2001).

14. *Polarization supermodes of phase-coupled arrays of vertical-cavity semiconductor lasers*,
    M. B. Willemsen, M. P. van Exter, J. P. Woerdman, F. Monti di Sopra,
    M. Moser, and E. Kapon,
    submitted for publication.

15. *Polarization loxodrome of a vertical-cavity semiconductor laser*,
    M. B. Willemsen, M. P. van Exter, and J. P. Woerdman,
    submitted for publication.

16. *Polarization stability of phase-locked arrays of vertical-cavity surface-emitting lasers*,
    F. Monti di Sopra, M. Moser, M. Brunner, M. B. Willemsen,
    M. P. van Exter, and E. Kapon,
    submitted for publication.